Relativistic Spin-dependent X-ray Absorption Theory.

by

Alexei L. Ankoudinov

A dissertation submitted in partial fulfillment of the requirements for the degree of

Doctor of Philosophy

University of Washington

1996

Approved by_____

(Chairperson of Supervisory Committee)

Program Authorized
to Offer Degree_____

Date_____

In presenting this dissertation in partial fulfillment of the requirements for the Doctoral degree at the university of Washington, I agree that the Library shall make its copies freely available for inspection. I further agree that extensive copying of this dissertation is allowable only for scholarly purposes, consistent with "fair use" as prescribed in the U. S. Copyright Law. Requests for copying or reproduction of this dissertation may be referred to University Microfilms, 1490 Eisenhower Place, P. O. Box 975, Ann Arbor, MI 49106, to whom the author has granted "the right to reproduce and sell (a) copies of the manuscript in microform and/or (b) printed copies of the manuscript made from the microform."

Signature_____

Date_____

University of Washington

Abstract

Relativistic Spin-dependent X-ray Absorption Theory.

by Alexei L. Ankoudinov

Chairperson of Supervisory Committee: Professor John J. Rehr
Department of Physics

Formally, the relativistic theory of X-ray absorption for nonmagnetic materials looks the same as non-relativistic theory. Usually relativistic effects are expected to be important for high Z elements, but even for low Z magnetic materials relativity is essential to describe several spin-dependent effects, while the non-relativistic theory gives null results. A new efficient way is suggested to treat relativistic and spin effects simultaneously. This approach is tested in calculations for several materials.

In order to achieve good agreement between x-ray absorption calculations and experiment, a good self-energy model is necessary. The self-energy or exchange correlation potential is the most important many-body correction for the calculation of x-ray absorption. The x-ray magnetic circular dichroism (XMCD) signal is primarily due to the spin dependence of the self-energy. A number of ways to improve the self-energy calculations are discussed and tested. The edge specific sum rules are also discussed. A new derivation of these sum rules is proposed. Many body analysis within sudden approximation is done, and shows that the sum rules give ground state properties.

A new version of the *ab initio* XAS code, FEFF7, has been developed, in which a Dirac-Fock atomic code replaces the LDA atomic code. This gives a better description of the core electrons, and also allows one to test the importance of the self-energy nonlocality. A new fully relativistic subroutine has been written for dipole matrix elements. Spin dependence of exchange-correlation potential is included. Results for a number of materials are discussed.

TABLE OF CONTENTS

LIST OF FIGURES

LIST OF TABLES

ACKNOWLEDGMENTS

I wish to express my indebtedness to Professor John J. Rehr for his invaluable guidance during the entire time of the thesis project.

I express my gratitude to Professors Edward A. Stern, Hannes Jonsson, David J. Thouless, and Larry B. Sorensen for their helpful assistance in various aspects of my graduate study.

I also acknowledge fruitful discussions with my colleagues Steve Zabinsky, Anatoly Frenkel, Matt Newville, Bruce Ravel, Kiril and Vadim Tsemekhman.

Finally, I thank my family for their patience, understanding and cheerful support.

Chapter 1

INTRODUCTION

Historically, the first measurements of the fine structure in x-ray absorption spectra were made in 1920 by Fricke [1] and Hertz [2]. The first explanation, based on newly developed quantum mechanics, was given by Kronig [3] in 1931. He explained the fine structure in terms of the singularities at the Brillouin zone boundaries. Later, this became known as a long range order (LRO) theory. Also Kronig [4] interpreted the XAFS of the molecules in terms of a short-range order (SRO) theory. He realized that the final state wave function should have modulations caused by the backscattering from the neighbors.

The controversy between SRO and LRO explanations of the fine structure was resolved only 40 years later in 1971, when Sayers, Stern and Lytle [5] applied a Fourier transform with respect to the photoelectrons wave vector. The peaks in Fourier transform were expected to be close to the distances to coordination shells of the absorbing atom [6]. This work showed that the SRO theory works for both molecules and solids. Thus it became clear that the extended x-ray absorption fine structure (EXAFS) contains an important structural information concerning nearest neighbor distances and coordination numbers. This information can be obtained even for the disordered materials such as alloys, glasses, etc.. Evolution of the ideas which led to this pioneering work, is reviewed by Stern and Heald in [7].

To extract structural information from EXAFS one needs an accurate knowledge of both the photoelectron properties and the lattice dynamics properties. In the 70's these properties (scattering phase shifts, mean free path, dispersion relation, and Debye-Waller factors) could not be calculated accurately enough. Therefore phenomenological EXAFS analysis, based completely on experimental data, was developed. However, with this approach the precision in distances never was better than 0.02 Å.

During the 80's a number of theoretical groups developed *ab initio* codes for

EXAFS analysis.[8, 9, 10, 11, 12, 13] All of them are based on the multiple scattering (MS) theory. But only with introduction of both the self-energy and the Debye-Waller (DW) factors in the x-ray absorption calculation [14, 12], did it become possible to reach good agreement between theory and experiment for the materials with known structures. The use of the MS theory with self-energy and DW factors made it possible to reduce the distance determination precision in crystals to 0.003 Å.

The XMCD (x-ray magnetic circular dichroism) was first observed by G. Schütz et al. [15] in 1987. It was predicted by Erskine and Stern [16] in 1975. The XMCD signal in the extended region is primarily due to the spin dependence of exchange potential. Therefore, it provides a very important test of the self-energy spin dependence and of our understanding of magnetism. However, no reliable calculations of the effect were available. In 1992 Carra et al. have derived edge specific sum rules, which explicitly connect polarization dependent XANES with ground state properties. Thus XMCD started to receive even more attention as a tool to separate orbital and spin contribution to the net magnetization of materials.

1.1 Goals

Our work deals with different aspects of x-ray absorption theory and *ab initio* codes for accurate calculations. The main goals of this dissertation are:

- Generalize relativistic theory of x-ray absorption for the spin dependent systems.
- Improve self-energy model and test the importance of non-local exchange.
- Improve *ab initio* calculation of x-ray absorption.

To achieve these goals I carried out the following investigations:

- developed relativistic and spin-dependent generalization of the Rehr-Albers multiple scattering formalism
- tested broadened plasmon self-energy model and partly nonlocal self-energy model using core-valence separation

- re-derived edge specific sum rules and analyzed many body corrections
- calculated the x-ray magnetic circular dichroism (XMCD) for Gd and other spin resolved spectra
- tested model of excitation spectra.
- introduced Lorentzian convolution to account for edge corrections in XANES.

1.2 Dissertation overview

In Chapter 2 I begin with a review of important concepts in the x-ray absorption calculation that appear already in single electron theory. Such a theory is much easier to understand than many-body theory and requires only the knowledge of textbook quantum mechanics. Messiah's book [17] is strongly recommended, since it treats all important details of collision theory and relativistic theory of light absorption. Next Chapter 3 discusses complications to the single electron theory due to the spin dependence of potential and the spin-orbit interaction. Chapter 4 describes the corrections to x-ray absorption due to many-body effects. An introduction to the important many particle physics can be found in Mahan's book,[18] and the other details are in the Hedin-Lundqvist review.[19] Details of the new code (FEFF7), based on the theory developed in previous chapters, are presented in chapter 5.

The remaining chapters discuss the application of FEFF7 to real materials. Chapter 6 revisits the standard FEFF test, x-ray absorption of Cu metal, and compares the new code to older versions. Chapter 7 deals with the polarization dependent measurements and shows the importance of fully relativistic calculations for heavy elements. In Chapter 8 I discuss calculations for magnetically ordered materials.

Conclusions are given in Chapter 9.

1.3 Terminology in X-ray Absorption

In an x-ray absorption experiment, light with intensity I is falling on the sample with width dx. The reduction in intensity due to the sample is dI. The measured *absorption coefficient*, defined as

$$\mu(E) = (dI/dx)/I \tag{1.1}$$

is simply connected to the total absorption cross section, if the concentration of absorbing atoms n_a is known:

$$\sigma_{tot}(E) = \mu(E)/n_a \; . \tag{1.2}$$

As will be shown in Chapter 2 there is a natural theoretical separation of the total absorption coefficient $\mu(E)$ into a smooth embedded atom absorption $\mu_0(E)$ and an oscillating fine structure, which is conveniently described by the XAFS function,

$$\chi(E) = \frac{\mu(E) - \mu_0(E)}{\mu_0(E)} \quad . \tag{1.3}$$

There are a number of commonly used abbreviations, used in this paper:

- XAS - x-ray absorption spectra - $\mu(E)$
- EXAFS - extended XAFS - $\chi(E)$, E above 40 eV of threshold
- NEXAFS - near edge XAFS - $\chi(E)$, first 40 eV above the edge
- XANES - x-ray absorption near edge structure - $\mu(E)$, first 40 eV above the edge including edge and below
- XAFS - x-ray absorption fine structure - $\chi(E)$ including EXAFS, NEXAFS and XANES
- XMCD - x-ray magnetic circular dichroism - difference in absorption of right and left circular polarized light

The X-ray absorption coefficient is also proportional to the fluorescence intensity. This is much more convenient to measure for the optically thick samples. Sometimes this method also allows one to separate spin-up from spin-down signal, giving more abbreviations:

- SPXAS - spin polarized XAS - $\mu(E, m_s)$
- SPEXAFS - spin polarized EXAFS - $\chi(E, m_s)$, $E > 40eV$

Here m_s stands for the photoelectrons spin direction (up or down). SPXAS is closely related to XMCD for the ferromagnetic materials (see section 3.2). However, it can give a unique information for the anti-ferromagnetic materials, where the XMCD signal will be zero.

Chapter 2

SINGLE ELECTRON THEORY OF X-RAY ABSORPTION

2.1 Multiple scattering formula for the cross section

Using *Fermi's Golden rule* for the transition rate, the total absorption cross section in the Gaussian units is:

$$\sigma_{tot}(\omega) = \frac{4\pi^2 e^2}{cm^2\omega} \sum_{i,f} \left| \langle f | \vec{p} \cdot \hat{\epsilon}\, e^{i\vec{k}\cdot\vec{r}} | i \rangle \right|^2 \delta(\epsilon_f - \epsilon_i - \hbar\omega), \tag{2.1}$$

where ω is frequency of the x-rays with wavevector $\vec{k}$ and unit polarization vector $\hat{\epsilon}$. Labels i and f stand for initial (occupied) and final (empty) states, with energies ϵ_i and ϵ_f. All other notations are standard. This expression is easy to derive from the Sakurai [20] formula (2.96). The relativistic expression looks very similar:

$$\sigma_{tot}(\omega) = \frac{4\pi^2 e^2 c}{\omega} \sum_{i,f} \left| \langle f | \vec{\alpha} \cdot \hat{\epsilon}\, e^{i\vec{k}\cdot\vec{r}} | i \rangle \right|^2 \delta(\epsilon_f - \epsilon_i - \hbar\omega), \tag{2.2}$$

where $\vec{\alpha}$ are the Dirac matrices, and i and f represent the Dirac spinors for the initial and final states. For convenience from now on I will use atomic units ($\hbar = e = m = 1$, $c = 1/\alpha = 137.037$). The above two formulas will look the same by writing the dipole operator $d_\epsilon = \vec{p} \cdot \hat{\epsilon}\, e^{i\vec{k}\cdot\vec{r}}$ in the first and $d_\epsilon = c\,\vec{\alpha} \cdot \hat{\epsilon}\, e^{i\vec{k}\cdot\vec{r}}$ in the second.

In the band structure approach one finds eigenstates and eigenvalues (i, f, ϵ_i and ϵ_f) and calculates the cross section using formula 2.1. We use a different approach - *multiple scattering theory* - which is based on the Green's function formulation. In single electron theory, the Green's function is defined by:

$$G(\vec{r}, \vec{r}\,', E) = \langle \vec{r} | \hat{G}(E) | \vec{r}\,' \rangle = \langle \vec{r} | \frac{1}{E - H + i\eta} | \vec{r}\,' \rangle = \sum_f^{all} \frac{\langle \vec{r} | f \rangle \langle f | \vec{r}\,' \rangle}{E - \epsilon_f + i\eta}, \tag{2.3}$$

where $\eta = 0^+$ is infinitesimal and positive. The expression for the cross section can be rewritten as:

$$\sigma_{tot}(\omega) = -\frac{4\pi}{c\,\omega}\mathrm{Im}\sum_i \langle i|d_\epsilon^* \hat{G}(\omega+\epsilon_i)d_\epsilon|i\rangle\theta(\omega+\epsilon_i-\epsilon_F) \tag{2.4}$$

where ϵ_F is the the energy of Fermi level (chemical potential). The θ function had to be added, since according to the definition 2.3, the MS Green's function has poles below the chemical potential which should be excluded for the calculation of cross-section. To account for finite temperature one can use Fermi distribution function $\theta = 1/(1+\exp((\omega+\epsilon_i-\epsilon_F)/kT)$, however temperature dependence can usually be neglected, since other broadening mechanisms are more important.

The one-particle Hamiltonian is separated into two parts: $H = H_0 + V$, where $H_0 = -\frac{1}{2}\vec{\nabla}^2 + V_{mt}$ is the free electron Hamiltonian with shifted zero level, and $V = \sum_i v_i$ is the scattering potential, which consists of possibly overlapping spherically symmetric potentials. The scattering potential V is zero in the interstitial region. The free particle Green's function G^0 is defined as

$$G^0(\vec{r},\vec{r}\,',E) = \langle\vec{r}|\hat{G}^0(E)|\vec{r}\,'\rangle = -\frac{2k}{4\pi}\frac{e^{ik|\vec{r}-\vec{r}\,'|}}{k|\vec{r}-\vec{r}\,'|} = 2k\tilde{G}^0(\vec{\rho}-\vec{\rho}\,')\,, \tag{2.5}$$

where $k = \sqrt{2(E-V_{mt})}$, and $\vec{\rho} = k\vec{r}$. Note that this definition of k differs from the conventional definition in EXAFS $k = \sqrt{2(E-E_F)}$. The Green's function for the central (absorbing) atom

$$G^c = \frac{1}{E - H_0 - V_c + i\eta} \tag{2.6}$$

requires a special treatment.

The full Green's function can be written using perturbation theory in V and the Dyson series expansion as

$$G = G^0 + \sum_i G^0 v_i G^0 + \sum_{i,j} G^0 v_i G^0 v_j G^0 + \cdots \quad . \tag{2.7}$$

Using the definition of t-matrix $t_i = v_i + v_i G^0 t_i$:

$$G = G^0 + \sum_i G^0 t_i G^0 + \sum_{i\neq j} G^0 t_i G^0 t_j G^0 + \cdots, \tag{2.8}$$

with t_i the scattering matrix at each scattering site.

The central atom Green's function $G^c = G^0 + G^0 t_c G^0$ can be expressed through regular and irregular solutions of Schrödinger equation in a central potential V_c

$$G^c = -2k \sum_\ell \left[R_\ell(r_<, k) N_\ell(r_>, k) + i R_\ell(r, k) R_\ell(r', k) \right] \sum_m Y_\ell^{m*}(\hat{r}) Y_\ell^m(\hat{r}\,'), \qquad (2.9)$$

where $r_< = \min(r, r')$ and $r_< = \max(r, r')$; $R_\ell(r, k)$ is regular at the origin and $N_\ell(k, r)$ is the irregular solution. Both functions are real and properly normalized: $R_\ell(r, k) = \cos(\delta_\ell) j_\ell(kr) + \sin(\delta_\ell) n_\ell(kr)$ and $N_\ell(r, k) = -\sin(\delta_\ell) j_\ell(kr) + \cos(\delta_\ell) n_\ell(kr)$ at distances larger than the central atom muffin tin radius ($r > r^c_{mt}$).

The total Green's function can be now written as

$$G = G^c + G^c \left[\sum_{c \neq i \neq c} t_i + \sum_{c \neq i \neq j \neq c} t_i G^0 t_j + \sum_{c \neq i \neq j \neq k \neq c} \cdots \right] G^c, \qquad (2.10)$$

where the sum starts and ends at the absorbing atom. Also two consecutive scatterings on the same atom is forbidden. The first term represents the background absorption from the absorbing atom alone. The successive terms are the contributions from single scattering, double scattering, and etc. Inserting a complete set of states for the energy $E = 1/2\, k^2$ between each pair of G^0 and t:

$$1 = \sum_L |L, i\rangle\langle L, i| = \sum_L |L, j\rangle\langle L, j|, \qquad (2.11)$$

where

$$\begin{aligned} \langle \vec{r} | L, i \rangle &= j_L(\vec{r} - \vec{R}_i) \qquad (2.12) \\ j_L(\vec{r}) &= i^\ell j_\ell(kr) Y_\ell^m(\hat{r}) \quad . \end{aligned}$$

Remember that the t-matrix by definition is an operator acting in this basis space of wave function, which are eigenfunctions of H_0. The expression for t_i through partial wave phase shifts can be obtained by considering the wavefunctions at $r > r_{mt}$

$$t_{\ell,i} = \frac{\tilde{t}_{\ell,i}}{2k} = \langle L, i | t_i | L, i \rangle = -e^{i\delta_{\ell,i}} \sin(\delta_{\ell,i})/(2k). \qquad (2.13)$$

Since we need only the imaginary part of G^c, it is enough to calculate only the regular solution of Dirac equation $R_\ell(r, k)$ for the central atom potential. This Green's function for $|\vec{r}_>| > r_{mt}$ is given by Messiah [17, p.872]

$$G(\vec{r}, \vec{r}\,', k) = -2\, k \sum_L Y_L^*(\hat{r}) Y_L(\hat{r}')\, R_\ell(k, r_<)\, h_\ell(kr_>) e^{i\delta_\ell} \quad . \qquad (2.14)$$

Using the addition theorem for the Bessel functions, h_L can be expressed as:

$$h_L(\vec{\rho}) = -\sum_{L'} j_{L'}(\vec{\rho}-\vec{\rho}_0)\tilde{G}'^0_{L',L}(\vec{\rho}_0) \tag{2.15}$$

where $\vec{\rho} = k\vec{r}$ and $h_L(\vec{\rho}) = i^\ell h_\ell(\rho)Y_\ell^m(\hat{\rho})$. The factor i^ℓ is inserted for convenience. The proof of addition theorem can be obtained by considering the one center expression for $\tilde{G}_0(\vec{\rho},\vec{\rho}\,')$ at $\rho' < \rho$:

$$\tilde{G}'^0(\vec{\rho},\vec{\rho}\,') = -\sum_L j_L^*(\rho_<)h_L(\rho_>) \tag{2.16}$$

and the two center expression [21, eq.6]:

$$\tilde{G}'^0(\vec{\rho},\vec{\rho}\,') = \sum_{L,L'} j_L(\vec{\rho}-\vec{\rho}_0)\tilde{G}'^0_{L,L'}(\vec{\rho}_0)j_L'^*(\vec{\rho}\,')\,. \tag{2.17}$$

The proof is completed by considering the limit $\rho' \to 0$. Since the Taylor expansion of $\tilde{G}_0(\vec{\rho},\vec{\rho}\,')$ in terms of ρ' is unique, therefore coefficients in front of $j_\ell(kr')$ in two expressions are equal.

Finally, the MS expression for cross-section, which we are going to use in calculations is:

$$\begin{aligned}\sigma_{tot}(\omega) &= -\frac{8\pi\, c\, k}{\omega}\mathrm{Im}\sum_{i,L,L'}\langle i|d_\epsilon^*|R_L\rangle \\ &\left[-i\,\delta_{L,L'} + e^{i(\delta_\ell+\delta_{\ell'})}\tilde{G}'^{sc}_{L,L'}(\omega+\epsilon_i)\right]\langle R_{L'}|d_\epsilon|i\rangle\theta(\omega+\epsilon_i-\epsilon_F)\end{aligned} \tag{2.18}$$

where $\langle\vec{r}|R_L\rangle = i^\ell\, R_\ell(r,k)Y_\ell^m(\hat{r})$ and $\tilde{G}'^{sc}_{L,L'} = \sum_N \tilde{G}'^N_{L,L'}$; $N = 1,2,\ldots$ correspond to contribution from single, double, etc. scattering.

$$\tilde{G}'^N_{L,L'} = \sum_{\vec{R}_1,\ldots,\vec{R}_N} \tilde{G}'^N_{L,L'}(\vec{R}_1,\ldots,\vec{R}_N) \tag{2.19}$$

$$\tilde{G}'^N_{L,L'}(\vec{R}_1,\ldots,\vec{R}_N) = \sum_{\{L_i\}} \tilde{G}'^0_{L,L_N}(\vec{\rho}_{N+1})\tilde{t}_{\ell_N,N}\cdots\tilde{G}'^0_{L_2,L_1}(\vec{\rho}_2)\tilde{t}_{\ell_1,1}G'^0_{L_1,L'}(\vec{\rho}_1) \tag{2.20}$$

Therefore there are only three main ingredients in the formulas for x-ray absorption:

- matrix elements of the interaction with light $\langle i|d_\epsilon^*|R_L\rangle$
- two center matrix elements of free propagator $G^0_{L,L'}(\vec{\rho})$

- scattering t-matrix $t_{\ell,i}$

To calculate all of them we need,

- regular solution R_ℓ for the central atom
- two center RA propagator representation and rotation matrices
- partial wave phase shifts for all different atom sites in solid $\delta_{\ell,i}$

They are obtained by solving the Dirac (or Schrödinger in non-relativistic approximation) equation for a central field potential.

2.2 Multipole matrix elements

I will discuss only relativistic form of the multipole matrix elements [22], since relativistic generalization of the MS theory is straightforward. One only has to change the basis from $|LS\rangle$ to $|J\rangle$ (or $|\kappa\rangle$ to be precise), and to calculate two $t_j(k)$ ($j = l \pm 1/2$) instead of each $t_l(k)$. Within this approach the spin-orbit interaction is treated exactly. Following the review of Grant, we are interested in the relativistic expression for the matrix elements of multipole transitions :

$$\langle n\kappa m|\vec{\alpha}\cdot\hat{\epsilon}\,\hat{e}^{i\vec{k}\vec{r}}|n'\kappa'm'\rangle\,. \tag{2.21}$$

All relativistic notations are described in Grant's review [22]. The quantum number $\kappa = \ell$ if $j = \ell - 1/2$, and $\kappa = -\ell - 1$ if $j = \ell + 1/2$. Without any loss of generality we can consider the vector $\vec{k}$ along the z-axis and right and left circular polarizations $\hat{\epsilon}_1 = -(\hat{\epsilon}_x + i\hat{\epsilon}_y)/\sqrt{2}$ and $\hat{\epsilon}_{-1} = (\hat{\epsilon}_x - i\hat{\epsilon}_y)/\sqrt{2}$. Expression for matrix elements can be most easily obtained using irreducible tensor algebra [23, 17]. Using the decomposition of $e^{i\vec{k}\cdot\vec{r}}$ in terms of the irreducible tensors $C_0^{(\ell)}$

$$e^{i\vec{k}\cdot\vec{r}} = \sum_{\ell=0}^{\infty} i^\ell(2\ell+1)j_\ell(kr)C_0^{(\ell)}(\hat{r})\,. \tag{2.22}$$

The vector operator $\vec{\alpha}$ is a tensor of order 1. The product of two tensors can be decomposed in terms of the irreducible tensors [23, 17]

$$\vec{\alpha}\cdot\hat{\epsilon}_p\,e^{i\vec{k}\vec{r}} = \sum_{L=1}^{\infty}\sum_{\ell=L-1}^{L+1} a_{\ell L}(r)\begin{pmatrix} 0 & X_p^{((\ell 1)L)} \\ X_p^{((\ell 1)L)} & 0 \end{pmatrix} \tag{2.23}$$

where

$$a_{\ell L}(r) = (-1)^L [L]^{1/2} i^\ell \begin{pmatrix} \ell & 1 & L \\ 0 & -p & p \end{pmatrix} j_\ell(kr) \tag{2.24}$$

depends only on r and not on angular or spin coordinates. On the contrary, the irreducible tensor $X_p^{((\ell 1)L)}$ does not depend on r and acts on the angular and spin coordinates only. Thus the operator connects two upper components of the initial state Dirac spinor only with the two lower components of final state spinor (and vice versa). The Grant's result (formula 6.30 [22]) can be rewritten in the form of Wigner-Eckart theorem:

$$\langle n\kappa m|\, a_{\ell L}(r) X_p^{((\ell 1)L)} \otimes \begin{pmatrix} 0 & 1 \\ 1 & 0 \end{pmatrix} |n'\kappa' m'\rangle = (-1)^{j-m} \begin{pmatrix} j & L & j' \\ -m & p & m' \end{pmatrix} R^{\ell L}_{\kappa\kappa'} \tag{2.25}$$

where the reduced matrix element $R^{\ell L}_{\kappa\kappa'}$ is

$$R^{\ell L}_{\kappa\kappa'} = \sum_\beta \langle n\kappa\beta | a_{\ell L}(r) | n'\kappa' - \beta\rangle C^{\ell L}_{\kappa\kappa'}(\beta). \tag{2.26}$$

Here $\beta = \pm 1$ corresponds to the upper (lower) component of Dirac spinor.

$$C^{\ell L}_{\kappa\kappa'}(\beta) = \sqrt{6}[j, L, j', \lambda, \lambda']^{1/2} (-1)^\lambda \begin{Bmatrix} \lambda & \ell & \lambda' \\ \frac{1}{2} & \frac{1}{2} & 1 \\ j & j' & L \end{Bmatrix} \begin{pmatrix} \lambda & \ell & \lambda' \\ 0 & 0 & 0 \end{pmatrix} \times \tag{2.27}$$
$$\times \delta(\lambda, j - \frac{1}{2} a\beta) \delta(\lambda', j' + \frac{1}{2} a'\beta)$$

where the usual notation of atomic physics is used:$[k, l, \ldots] = (2k+1)(2l+1)\ldots$; $a = 1$ for negative κ and $a = -1$ for positive κ. In the dipole approximation it is enough to keep only one term ($\ell = 0, L = 1$).

$$R_{\kappa\kappa'} = i \int dr\, j_0(kr) (P_\kappa Q_{\kappa'} C_{\kappa\kappa'}(1) + Q_\kappa P_{\kappa'} C_{\kappa\kappa'}(-1)) \quad , \tag{2.28}$$

where

$$C_{\kappa\kappa'}(\beta) = \beta\sqrt{6}[j, j']^{1/2} (-1)^{j-1/2-\lambda} \begin{Bmatrix} \frac{1}{2} & \frac{1}{2} & 1 \\ j' & j & \lambda \end{Bmatrix} \delta(\lambda, j - \frac{1}{2} a\beta) \delta(\lambda, j' + \frac{1}{2} a'\beta). \tag{2.29}$$

It is easy to calculate all $C_{\kappa\kappa'}(\beta)$ using appendices of Messiah book.[17] I have found that the result can be expressed by one formula:

$$C_{\kappa\kappa'}(\beta) = \beta(-1)^{(\Delta-1)}\frac{\sqrt{|(\Delta+\beta)(2\kappa+\Delta)(2\kappa+\Delta-1)(2\kappa+\Delta+1)|}}{2\kappa+\beta} \tag{2.30}$$

where $\Delta = 0$ if $\kappa = -\kappa'$, otherwise $\Delta = \kappa' - \kappa = \pm 1$. These are the only possible pairs of $\kappa\kappa'$ in the dipole approximation.

Thus it is easy to calculate the dipole matrix elements in relativistic theory, using the formula for reduced matrix elements $R_{k,k'}$. The algebra always looks simpler with the reduced matrix elements. Thus for a smooth atomic cross-section we have:

$$\sigma_{at}(\omega) = \frac{8\pi\, c\, k}{3\,\omega}\sum_{k'}|R_{\kappa\kappa'}|^2 \quad . \tag{2.31}$$

And defining normalized reduced matrix elements by

$$\tilde{R}_{\kappa\kappa'} = e^{i\delta_{\ell'}}\frac{3R_{\kappa\kappa'}}{\sum_{\kappa'}|R_{\kappa\kappa'}|^2} \quad , \tag{2.32}$$

the equation for the fine structure is

$$\chi = \sum_{\kappa_0,\kappa_N}\tilde{R}_{\kappa\kappa_0}\tilde{R}_{\kappa\kappa_N}\begin{pmatrix} j & 1 & j_0 \\ m_j & \epsilon & m\end{pmatrix}\begin{pmatrix} j & 1 & j_N \\ m_j & \epsilon & m'\end{pmatrix}\langle J_N|\tilde{G}^{sc}|J'\rangle\,. \tag{2.33}$$

$$\langle J_N|\tilde{G}^{sc}|J'\rangle = \langle J_N|L_NS\rangle\langle|L_NS|\tilde{G}^{sc}|L_0S'\rangle\langle L_0S'|J'\rangle\,. \tag{2.34}$$

This relativistic formalism is quite useful for calculations. Since spin-orbit interaction is negligible in the interstitial region, one can use the same two center Green's function matrix elements $\langle LS|G^0|L'S'\rangle = G^0_{L,L'}\delta_{S,S'}$. This can be used even for spin-dependent potentials. All necessary modifications are:

- t-matrix is diagonal in j-basis:$\langle J|t_i|J'\rangle = t_{j,i}\delta(J,J')$.

- transformation from J-basis to L,S basis (Clebsch-Gordon coefficients) $\langle J|LS\rangle$

2.3 Rehr-Albers decomposition of Green's function

Rehr and Albers have found an efficient separable representation for the two center free space Green's function:

$$\tilde{G}^0_{L,L'}(\vec{\rho}) = \frac{e^{i\rho}}{\rho} \sum_{\lambda} \tilde{\Gamma}^L_{\lambda}(\vec{\rho}) \Gamma^{L'}_{\lambda}(\vec{\rho}) \tag{2.35}$$

where the successive terms in λ have decreasing significance. Their paper [21] gives detailed prescription for how to calculate Γ and $\tilde{\Gamma}$. Retaining only first term is equivalent to small atom plane wave approximation. The rest of the terms are called curved wave corrections. It is usually enough to retain only 6 terms in λ-expansion

Defining a scattering matrix F and "termination matrix" M as

$$F_{\lambda,\lambda'}(\vec{\rho},\vec{\rho}\,') = \sum_{L} t_{\ell} \Gamma^L_{\lambda}(\vec{\rho}) \tilde{\Gamma}^L_{\lambda'}(\vec{\rho}\,') \tag{2.36}$$

$$M^{L_0,L_N}_{\lambda_0,\lambda_N}(\vec{\rho}_1,\vec{\rho}_N) = \Gamma^{L_0}_{\lambda_0}(\vec{\rho}_1) \tilde{\Gamma}^{L_N}_{\lambda_N}(\vec{\rho}_N) \tag{2.37}$$

the equation for the MS Green's function is analogous to the plane wave formula

$$\tilde{G}^{(N-1)}_{L_N,L_0}(\vec{R}_1,\ldots,\vec{R}_N) = \frac{e^{i(\rho_1+\rho_2+\cdots+\rho_N)}}{\rho_1\rho_2\cdots\rho_N} \sum_{\{\lambda_i\}} M^{L_0,L_N}_{\lambda_0,\lambda_N}(\vec{\rho}_1,\vec{\rho}_N) \times$$
$$F_{\lambda_N,\lambda_{N-1}}(\vec{\rho}_N,\vec{\rho}_{N-1}) \times \cdots \times F_{\lambda_3,\lambda_2}(\vec{\rho}_3,\vec{\rho}_2) \times F_{\lambda_2,\lambda_1}(\vec{\rho}_2,\vec{\rho}_1)\,. \tag{2.38}$$

This formula involves multiplication of 6×6 matrices. For the EXAFS analysis one needs $l_{max} = 25$. The standard MS formula has the multiplication of 1250×1250 matrices. Thus without RA decompositions calculations of EXAFS, using MS expansion, will be a million times slower, since the time to make matrix multiplication scales as third power of dimension. Even with fast RA algorithm the calculation by the MS formula is a bottleneck of the whole program to calculate absorption cross section (see genfmt in the FEFF7 description).

2.4 Full Multiple Scattering

The other way to overcome the bottleneck is to calculate the MS in infinite order for a finite cluster. G^0 and t_i are matrices in a basis vector space $|L,R_i\rangle$,

$$\langle L,k|t_i|L',j\rangle = t_{\ell,i}\,\delta_{i,k}\,\delta_{i,j}\,\delta_{L,L'} \tag{2.39}$$

$$\langle L,i|G^0|L',j\rangle = G^0_{L,L'}(\vec{\rho}_i - \vec{\rho}_j) \tag{2.40}$$

The basis set $|L, R_i\rangle$ can be formally treated as an orthonormal set

$$\langle L, i|L', j\rangle \quad = \quad \delta_{i,j}\, \delta_{L,L'}. \tag{2.41}$$

If we just add additional site diagonal condition

$$\langle L, i|G^0|L', i\rangle \quad = \quad 0 \tag{2.42}$$

then the exclusion of double scattering from the same center will be done automatically. This allows one to suppress matrix indices and write the total Green's function as

$$G^{sc} = G^0 + G^0 T G^0 + G^0 T G^0 T G^0 + \cdots \tag{2.43}$$

where $T = \sum_i t_i$ is the total scattering matrix. The expression for G^{sc} is obviously a geometric series. Full multiple scattering for the finite cluster can be made, since the matrix will have finite dimensions and one can do matrix inversion:

$$G^{sc} = \left[1 - G^0 T\right]^{-1} G_0 \quad . \tag{2.44}$$

The above equations guarantee that full MS formula is equivalent to MS expansion for the finite cluster. In fact "Full multiple scattering " is not full, since it does not count paths which have scattering atoms outside the cluster. Zabinsky [24] has shown that the most important paths are almost linear and triangular. They have at most one backscattering event and several or none almost forward scatterings. Therefore it is often better to use usual MS with path filters than "full" MS. Path filtering is extensively discussed in S. Zabinsky thesis [24]. On the other hand large modern computers can handle matrices with dimension $10^4 \times 10^4$. Since one have to use angular momentum up to 25, this means that number of atoms in cluster can be as big as $10^4/\ell^2_{max} = 16$, which is usually not enough. For solids one typically needs a cluster of 500 atoms. Therefore the calculations in the XANES are limited to $\ell_{max} = 4$. However, modern EXAFS structural analysis is based on MS path expansion and fitting in R-space (Fourier transform from k-space). Thus for analysis of unknown structures one hardly needs full MS, but it can be used as a final check for the model structure. The other shortcoming of full MS approach is that accurate treatment of Debye-Waller factors is impractical.

2.5 Self-consistent muffin tin potential

The same expansion appears not only in the formula for absorption coefficient, but also in the expression for the electron density at point $\vec{r}$:

$$\rho_{s,s'}(\vec{r},E) = -\frac{1}{\pi}\mathrm{Im}\, G^{tot}_{s,s'}(\vec{r},\vec{r},E) \tag{2.45}$$

where s, s' are spin indices. The density of states is

$$\rho(E) = \sum_s \int d^3r\, \rho_{s,s}(\vec{r},E)\,. \tag{2.46}$$

The chemical potential μ is given by

$$\int_{-\infty}^{\mu} dE\rho(E) = N, \tag{2.47}$$

where N is the total number of electrons. The usual density is a trace over spin indices of the matrix

$$\rho_{s,s'}(\vec{r}) = \int_{-\infty}^{\mu} dE\rho_{s,s'}(\vec{r},E)\,. \tag{2.48}$$

The new $\rho_{s,s'}(\vec{r})$ can be diagonalized for every space point and used to improve the muffin tin potential.

Currently, FEFF7 uses the so called Mattheiss prescription for muffin tin potential. That is, the charge density is constructed just as a sum of free atomic densities. All small details in this potential become irrelevant if the outgoing photoelectron has high enough energy of order 20 eV above Fermi level. Therefore, for the purpose of EXAFS analysis it is enough to use Mattheiss prescription, but improved potentials may be needed for XANES calculations.

A practical procedure to improve muffin-tin potential can be suggested for future work:

1)Use Mattheis prescription to construct overlapped densities around each atom $\rho^i_{ovp}(r)$.

2)Find Norman and muffin-tin radii from $\rho^i_{ovp}(r)$ and construct muffin-tin potential. (Subroutine istprm.f of FEFF7).

3)Find new wavefunctions modified by the presence of the neighbors.

4)For the energy range, where one expects the chemical potential, calculate:

$$N^i(E) = \frac{1}{\pi}\int_0^{r_{nrm}} d^3r \int_{-\infty}^{E} \sum_\ell \frac{2kR_\ell^2(r)}{4\pi}\left[2\ell+1-\mathrm{Im}\sum_m \tilde{G}_{L,i;L,i}e^{2i\delta_\ell}\right]. \qquad (2.49)$$

Determine the chemical potential from condition $\sum_i N^i(\mu) = N_{tot}$. On the first iteration the quantity $Z^i - N^i(\mu)$ can be interpreted as charge transfer.
5)Build new $\rho^i_{ovp}(r)$

$$\rho^i_{ovp}(r) = \frac{1}{\pi}\int_{-\infty}^{\mu} dE \sum_\ell \frac{2kR_\ell^2(r,E)}{4\pi}\left[2\ell+1-\mathrm{Im}\sum_m \tilde{G}_{L,i;L,i}(E)e^{2i\delta_\ell}\right]. \qquad (2.50)$$

The derivation of both above formulae can be understood from the MS expression 2.18, if one will do spherical averaging. Now the self-consistent loop is closed by going back to step 2.

In practice may be even first correction will be enough, since even with Mattheiss prescription the XANES calculations are often close to experiment. For example, to account for onlyonly the embedded atom corrections to wave functions one simply neglects the second term within the square brackets

In the case of nonmagnetic materials the total electronic density is uniquely defined by the above procedure. Therefore, the ground state potential and density can be found. According to the Hohenberg and Kohn theory, the requirement of energy minimization leads to unique ground state potential and electron density. The unique muffin-tin potential will be just the approximation to the true ground state potential. This is another reason to do just few iterations for the self-consistent muffin-tin potential.

For magnetic materials additional complications arise, since one also has to minimize the total energy with respect to spin degrees of freedom. However, if the spin arrangement is known, then still the one shot atomic (Mattheiss) prescription can be used to construct spin-dependent muffin-tin potential. One usually neglects the spin polarization of valence s- and p-electrons. All density magnetization is assumed to be due to the partly filled d- and f-shells. Then von Barth-Hedin prescription[25] can be used to construct the spin-dependent potential. This construction implies that the principal source of magnetism is atomic magnetism, the nature of which is clear from the Hund's rules. Spin-ordering happens due to minimization of the total energy

with respect to the spin degrees of freedom. This may induce the spin-polarization of valence s- and p-electrons, which can be also estimated by MS theory. Also, valence s- and p-electrons can play an important role in the spin ordering. Therefore, the first shot procedure may be not enough for the XANES calculations, but should be satisfactory for the EXAFS, where the scattering is slightly affected by valence s- and p-electrons.

2.6 Optical potential

2.6.1 Core-hole lifetime

The core hole lifetime Γ_{ch} describes the interaction with the passive $N-1$ electrons, which is assumed independent of the energy of outgoing photoelectron. If the system of N-1 electrons is left in state $|N-1,n\rangle$ then probability to find system in the state n after time t is decaying exponentially mainly due to radiative decay.

$$|\langle N-1,n|U(t)|N-1,n\rangle|^2 \propto e^{-\Gamma_{ch}t}\,, \tag{2.51}$$

where the Heisenberg picture has been used and U is the evolution operator. In the energy domain the effect is to shift the position of poles of Green's function by $-i\Gamma_{ch}/2$. Thus all of the above formulae are valid with $i0^+ \to iV_i$ and $V_{mt} \to V_{mt} - iV_i$ ($V_i = \Gamma_{ch}/2$). This corresponds to the use of "optical" potential. All propagators decay exponentially, reducing contributions from long paths.

The Green's function, obtained with MS, has all poles below real axis, but some of them lie below chemical potential μ. To get the retarded Green's function it is necessary to get rid of the contribution from those poles. If we are interested in the imaginary part of G only, then one can do the calculations with real potential, multiply by $\theta(E-\mu)$, and convolute the resulting absorption coefficient with a Lorentzian

$$\sigma(\omega) = \int dE\; \sigma_0(E)\theta(E-\mu)\,.\frac{1}{\pi}\frac{V_i}{(\omega-E)^2+V_i^2} \tag{2.52}$$

However, sometimes the real part of Green's function is needed, e.g. for calculation of DAFS (diffraction anomalous fine structure).[26] The difference in real part of G (or whole G) can be calculated using a Kramers-Kronig transform.

2.6.2 Inelastic mean free path

The photoelectron propagating in solid, will eventually lose its energy due to creation of elementary excitations (plasmons, electron-hole pairs, etc.). These losses can be also described by means of an optical potential $-iV_{mfp}$. This is just the imaginary part of self-energy, which will be discussed later. For example, Penn[27] has shown how to estimate this average imaginary potential, using experimental inverse dielectric function $\epsilon^{-1}(\omega)$. Thus the total optical potential for the absorption measurement is given by the sum:

$$V_i(k) = \Gamma_{ch}/2 + V_{mfp}(k)\,. \tag{2.53}$$

Therefore we have two lifetimes: one is the lifetime of core-hole and the other is the lifetime of photoelectron state. If absorption is measured by the fluorescence method, the energy spectrum of emitted photons will have a half width $\Gamma/2$, due to the decay of core-hole state. One can ask a question: "If Γ is already accounted for by the measurement, whether it should be excluded from the optical potential?" The answer is "No!". Imagine that $V_{mfp} = 0$ and the incoming x-ray photons are well monochromated and have energy within Γ below the edge. One will still measure a nonzero fluorescence intensity, since the absorption processes will happen and will be observable by the transmission measurement. Thus one won't measure an abrupt step in fluorescence, and the total optical potential should be always used to calculate x-ray absorption despite the different measurement techniques. But the experimental resolution can be different for different devices, and also can be accounted for by the means of optical potential ($\eta > 0$):

$$V_i(k) = \Gamma_{ch}/2 + V_{mfp}(k) + \eta\,. \tag{2.54}$$

Therefore the effective mean free-path for EXAFS calculations is given by

$$\lambda_{eff} = k/V_i\,. \tag{2.55}$$

2.7 EXAFS formula

The fine structure formula for the *fixed* atomic positions can be rewritten as a sum over paths Γ:

$$\chi(k,\vec{\epsilon}) = \sum_{\Gamma} S_0^2 f_{\rm eff}(k,\vec{\epsilon},\Gamma) e^{ikR_\Gamma} e^{-R_\Gamma/\lambda_{\rm eff}} \tag{2.56}$$

where the constant factor S_0^2 will be discussed in chapter 4, the losses described by optical potential are shown explicitly, and from the previous formula for χ without losses we extracted a term e^{ikR_p} since only this term varies rapidly if distances between atoms change.

All atoms will oscillate around their equilibrium position even at zero temperature. Therefore, we have to average χ over these oscillations. If the probability to find given path Γ at distance R is equal to $P_\Gamma(R)$ and Gaussian (e.g. zero temperature vibrations)

$$P_\Gamma(R) = \frac{1}{\sqrt{2\pi\sigma_\Gamma}} \exp(-\frac{(R - \langle R_\Gamma \rangle)^2}{2\sigma_\Gamma^2}) \tag{2.57}$$

which is also often the case for disordered systems, according to the central limit theorem. Then:

$$\chi(k, \vec{\epsilon}) = \sum_\Gamma S_0^2 f_{\text{eff}}(k, \vec{\epsilon}, \Gamma) e^{ik\langle R_\Gamma \rangle} e^{-\langle R_\Gamma \rangle / \lambda_{\text{eff}}} e^{-\sigma_\Gamma^2 k^2/2}. \tag{2.58}$$

The last term is called Debye-Waller factor by analogy with X-ray diffraction. Even though the nature of this factor is the same i.e., motion of atoms, DW factor in EXAFS is due to the relative displacement of atoms (path length), unlike DW in diffraction, where individual atomic displacements matter. All details on Debye-Waller factors in EXAFS can be found in the Crozier, Rehr, Ingalls review paper [28], including correlated Einstein and Debye models for σ.

The EXAFS equation shows that contribution from the long paths will be small due to the mean free path and the DW factor. Therefore, by making a Fourier transform of $\chi(k)$ one expect to get peaks close to the lengths of the most important paths. Those are the paths with the shortest distance, i.e. one can get important information about distances to the nearest neighbors and coordination numbers. These are very important quantities for the structural analysis. Sometimes, EXAFS is the unique method, since it works also for the disordered materials (alloys, glasses, etc.) unlike standard x-ray diffraction techniques.

The algorithm of the structural EXAFS analysis, using the theoretical code to calculate f_{eff}(FEFF, etc.) and the fitting code to find distances (FEFFIT, etc), is represented by the flow diagram 2.1. FEFF and FEFFIT are the trademarks of University of Washington copyright codes, but other codes also exist. Thus in order to make real analysis of EXAFS data one has to use the FEFF program, which of course

Table 2.1: Algorithm for the structural EXAFS analysis with theoretical code.

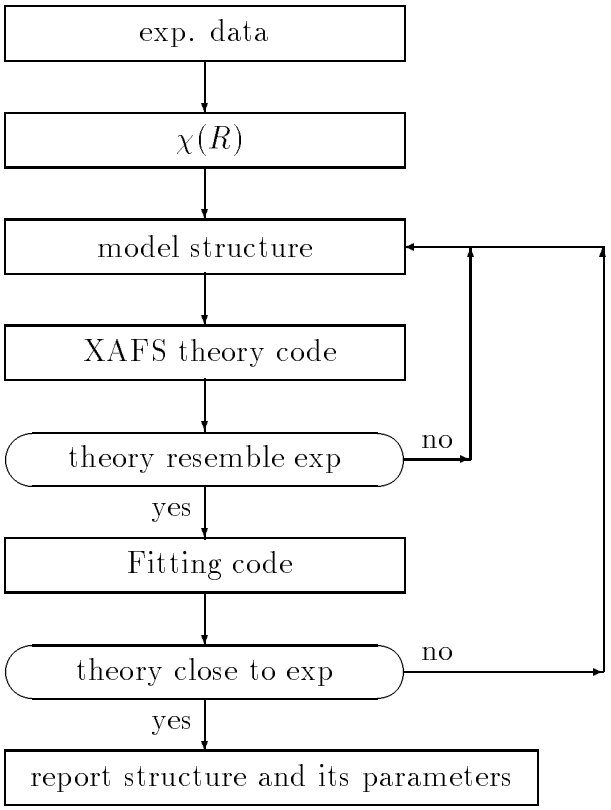

calculates f_{eff}. Few remaining parameters in the EXAFS formula are varied by some fitting program such as FEFFIT. These parameters are hard to get accurately by *ab initio* calculations (E_F, S_0^2, σ^2) or represent the primary interest of the structural analysis ($\langle R_\Gamma \rangle$). Actually, it is necessary to use FEFF in order to achieve high precision in distance determination (below 0.01 Å). In times before FEFF the precision rarely was below 0.05 Å.

Chapter 3

SPIN DEPENDENT SYSTEMS AND SUM RULES

3.1 Introduction

The theory of x-ray absorption of previous chapter must be modified for spin dependent systems (ferromagnetic, antiferromagnetic, etc.), since the potential and densities are spin-dependent. First, for simplicity I will neglect the spin-orbit interaction, except for the central atom initial state. For spin-dependent potentials the LS-basis is more convenient than the J-basis, which is natural to treat the SO interaction. Complications, arising in treating both interactions simultaneously are discussed in section 3.4.

With this approximation, the potential and the Green's function are diagonal 2×2 matrices in spin space. The difference between spin-up and -down potentials is due to the exchange interaction with spin-up (-down) populations. For the dipole matrix element we will neglect the SO interaction in the final state, but the SO interaction in the initial state cannot be neglected. This is a reasonable approximation since SO is very important for the core electrons, and much less important for the valence electrons.

Two kinds of x-ray absorption measurements are currently used to study magnetic order. The first method is X-ray magnetic circular dichroism (XMCD), where the difference of right and left circular polarized light is measured. Usually, (at least always for polycrystalline materials) a non-zero signal will arise only if there is a non-zero average magnetic moment. In the standard geometry the light is sent along magnetization axis. There are two sources for nonzero XMCD:

- in magnetic materials spin-up and -down potentials are different.

- due to spin-orbit interaction in the initial state (and also in the final state for $\ell = 0$ edges) the right (left) circularly polarized light will produce more spin-up (-down) electrons *along the direction of light propagation.* This is well known in atomic physics as the Fano effect.

The second method is connected with the fluorescence measurement of X-ray absorption. A photon of certain energy is emitted when an electron from an outer shell fills the core hole $i \to c$; e.g. for the K-edge of Fe 3p (i) electron fills 1s (c) core-hole. The measured fluorescence line (K_β) is split by several eV (15 for Fe) due to the exchange interaction. Exchange with partly filled 3d-shells is strong for the outer electrons (3p), and in the first approximation can be neglected for the deep core states (1s, 2s, 2p). Therefore, the observed line splitting is due to the exchange interaction of the outer electron (i), which definitely has more overlap with a nonzero spin density of valence electrons. If the splitting is big enough, then intensities of two lines can be measured independently. Thus the absorption for spin-up and spin-down electrons is measured separately. Notice, that in this method the direction of *the photoelectron spin is relative to the spin of central atom.* Also, since exchange will make the energy of 3p-up lower than energy of 3p-down, the line with lower energy correspond to the emission of photoelectron with spin-up. This method is applicable to study the spin order in antiferromagnets as well as in ferromagnets. The measured signal is called SPXAS (spin polarized XAS). Unlike XMCD, SPXAS has only one source – the spin-dependent potential – with an additional requirement that the exchange splitting of measured line is greater than it's width or SO splitting. Also this measurement does not require a circularly polarized light.

All formulas of the previous chapter remain valid but with the addition of spin indices. Thus the absorption coefficient is given by:

$$\sigma_{tot}(\omega,\epsilon,s) = -\frac{8\pi\, c\, k_s}{\omega}\mathrm{Im}\sum_{i,L,L'}\langle i|d^*_\epsilon|R_{Ls}\rangle \qquad (3.1)$$
$$\left[-i\,\delta_{L,L'} + e^{i(\delta_{\ell s}+\delta_{\ell' s})}\tilde{G}^{sc}_{Ls,L's}(\omega+\epsilon_i)\right]\langle R_{L's}|d_\epsilon|i\rangle\theta(\omega+\epsilon_i-\epsilon_F)\,,$$

where $s = m_s$ is the spin projection. The spin dependence of the scattering Green's function comes from the spin dependence of the free propagator G^0 ($k \to k_s$, since muffin-tin zero can be different for spin-up and -down electrons) and of the scattering t-matrices ($t_\ell \to t_{\ell s}$).

The average $\langle L_z\rangle$ in magnetic materials is non zero, except for elements with half-filled core levels. If all occupied orbitals are known, then the exchange potential for photoelectron ($\hat{V}_x = \sum_{occ}|f\rangle\langle f|/|r-r'|$) can be parameterized as: $\hat{V} = V(r)\hat{I} + V_S\hat{S}_z + V_L\hat{L}_z + V_{LS}\hat{L}_z\hat{S}_z$. This corresponds to the expansion of the potential in spherical

harmonics and retaining the terms in front of Y_{00} and Y_{10} for spin-up and spin-down separately. This maintains the spherical symmetry of scattering problem for the photoelectron with m_ℓ, m_s. The phase shifts will now depend on the values of m_l and m_s of the photoelectron, but otherwise the generalization of multiple scattering (MS) formalism is straightforward. For half-filled configurations, the scattering potential is different for spin-up and -down electrons, but independent of m_l. Our present code neglects the L_z dependence of scattering potential, but it can be included as will be discussed later. Construction of the spin-dependent muffin-tin potential has been already discussed in section 2.5. Comparison of calculated XMCD and SPXAS with experiment can be viewed as a test of this construction, and is therefore a test of our understanding of magnetism.

3.2 XMCD and SPXAS

The XMCD signal is the difference between absorption of right and left polarized light:

$$\sigma_c(\omega) = \sum_{m_s} \sigma_{tot}(\omega, +1, m_s) - \sigma_{tot}(\omega, -1, m_s)\,. \tag{3.2}$$

The polarization average SPXAS is given by

$$\sigma_s(\omega, m_s) = \frac{1}{3}\sum_{\epsilon} \sigma_{tot}(\omega, \epsilon, m_s)\,. \tag{3.3}$$

Both of them can be calculated using Eq. 3.1. Often polycrystalline averaging needs to be done. This means that the distant pieces of crystal have random orientations. However, spins can still point in the same direction (assuming a ferromagnet). Therefore the average scattering Green's function should be used in calculations:

$$\tilde{G}^{sc}_{Lm_s,L'm_s} = \delta_{L,L'}\bar{G}^{sc}_{\ell,m_s} \tag{3.4}$$

where $\bar{G}^{sc}_{\ell,m_s}$ is calculated by making a partial trace of G-matrix. Since the trace is invariant, we can simply calculate G for some orientation.

$$\sigma_c = \sum_{m_s}\sum_{k',k''} [j', j'']^{1/2} \tilde{R}^{m_s}_{k,k'} \tilde{R}^{m_s}_{k,k''} \delta_{\ell',\ell''} \tilde{C}(k, k', k'', m_s) \frac{1}{2\ell'+1} \sum_{m'_\ell} \tilde{G}^{sc}_{L'm_s,L'm_s} \tag{3.5}$$

where

$$\tilde{C}(k,k',k'',m_s) = \sum_{m_0} \begin{pmatrix} l_0 & 1/2 & j' \\ m_0 & m_s & -m' \end{pmatrix} \begin{pmatrix} l_0 & 1/2 & j'' \\ m_0 & m_s & -m' \end{pmatrix} \times \tag{3.6}$$
$$\left[\begin{pmatrix} j & 1 & j' \\ -m & -1 & m' \end{pmatrix} \begin{pmatrix} j & 1 & j'' \\ -m & -1 & m' \end{pmatrix} - \begin{pmatrix} j & 1 & j' \\ -m & 1 & m' \end{pmatrix} \begin{pmatrix} j & 1 & j'' \\ -m & 1 & m' \end{pmatrix} \right]$$

The polycrystalline average SPXAS looks even simpler:

$$\sigma_s = \frac{1}{2} \sum_{k'} \tilde{R}^{m_s}_{k,k'} \tilde{R}^{m_s}_{k,k'} \frac{1}{2\ell'+1} \sum_{m'_\ell} \tilde{G}^{sc}_{L'm_s,L'm_s} \tag{3.7}$$

Equations 3.5 and 3.7 can be used to make relativistic calculations of the polycrystalline average XMCD and SPXAS with a subtracted background. A simple relation (Eq. 3.24) between these two signals will be established later in the non-relativistic limit,

$$\sigma_c \approx \frac{\ell\,(-)^{j-j_+}}{j} \left[\sigma_s(\uparrow) - \sigma_s(\downarrow)\right] \quad . \tag{3.8}$$

Therefore XMCD and SPXAS should have the same order of magnitude for ferromagnets, except for $\ell = 0$ edges, where the SPXAS signal is expected to be significantly larger.

3.3 XMCD: Non-relativistic theory

Below we develop a quantitative MS theory for XMCD and SPXAS based on these considerations for the $\ell \rightarrow \ell + 1$ transitions only [29]. Our treatment makes use of the fast Rehr-Albers (RA) MS formalism [21] and takes advantage of symmetry properties of the total propagator G. The main contribution to the absorption $\mu(k)$ comes from the $l \rightarrow l+1$ transition ($l_0 = l_n$). From conservation of the projection of angular momentum, $m_0 + m_s = m_j + 1 = m_n + m_s$, it follows that $m_0 = m_n$, and

$$\mu^+(k) = -\frac{A\,k_0}{\pi}\,\mathrm{Im} \sum_{L_n,m_s} \tilde{G}^{m_s}_{L_n,L_n} \sum_{m_j} \langle J|L\,S\rangle \langle L\,S|p_-|L_n\,S\rangle \langle L_n\,S|p_+|L\,S\rangle \langle L\,S|J\rangle, \tag{3.9}$$

where $\langle L\,S|J\rangle$ are the Clebsch-Gordon coefficients.[17] Using the Wigner-Eckart theorem for dipole matrix elements we obtain

$$\mu^+(k) \;\; = \;\; -\frac{1}{\pi}\mathrm{Im} \sum_{m_n,m_s} \tilde{G}^{m_s}_{L_n,L_n} \Delta^2_{m_s}$$

$$\times \sum_{m_j,m_l} (2j+1) \begin{pmatrix} j & l & 1/2 \\ -m_j & m_l & m_s \end{pmatrix}^2 \begin{pmatrix} l & 1 & l+1 \\ m_l & +1 & -m_n \end{pmatrix}^2, \quad (3.10)$$

where the reduced matrix element $\Delta_{m_s} = \sqrt{A\,k_0}|\langle l\,j||p||l+1+m_s\rangle|$ depends on j, because the initial state radial wave function differs for $j = j^{\pm}$, and the final state radial wave function depends on m_s. The difference in the result for $\mu^-(k)$ is only a sign change, with -1 in the second 3j-symbol instead of $+1$. Using invariance of 3j-symbols under the simultaneous sign change of all m_i, we obtain

$$\begin{aligned} \mu^-(k) &= -\frac{1}{\pi}\mathrm{Im} \sum_{m_n,m_s} \tilde{G}^{-m_s}_{l_n\,-m_n,l_n\,-m_n} \Delta^2_{-m_s} \\ &\times \sum_{m_j,m_l} (2j+1) \begin{pmatrix} j & l & 1/2 \\ -m_j & m_l & m_s \end{pmatrix}^2 \begin{pmatrix} l & 1 & l+1 \\ m_l & +1 & -m_n \end{pmatrix}^2. \quad (3.11) \end{aligned}$$

Diagonal elements of the propagator have the property that $\tilde{G}_{l\,-m,l\,-m} = \tilde{G}_{l\,m,l\,m}$, which follows from the symmetry of $g^{|\mu|}_{l1,l2} = g^{|\mu|}_{l2,l1}$ [RA, Eq. (10)] and the properties of rotation matrices,[10] $R^l_{m_1,m_2}(\Omega^{-1}_{\hat{\rho}}) = (-1)^{m_2-m_1} R^l_{m_2,m_1}(\Omega_{\hat{\rho}})$ substituted into Eq. (9) of RA.[21] Here $\Omega_{\hat{\rho}}$ refers to the Euler angles that rotate a bond $\vec{\rho}$ onto the z-axis. For identical superscripts, which are henceforth suppressed, this procedure gives $\tilde{G}_{l_1\,-m_1,l_2\,-m_2} = (-1)^{m_2-m_1}\tilde{G}_{l_2\,m_2,l_1\,m_1}$. Thus in Eq. (14) of RA, the contribution to $\tilde{G}_{lm,lm}$ from the path $\Gamma = \vec{R}_1, \vec{R}_2 \ldots \vec{R}_n$ is the same as the contribution to $\tilde{G}_{l\,-m,l\,-m}$ from the inverse path, $\Gamma^{-1} = \vec{R}_n, \vec{R}_{n-1} \ldots \vec{R}_1$. We therefore obtain for the XMCD signal from a subshell j,

$$\begin{aligned} \mu^+ - \mu^- &= -\frac{1}{\pi}\mathrm{Im} \sum_{m_n,m_s} \left[\tilde{G}^{m_s}_{L_n,L_n}\Delta^2_{m_s} - \tilde{G}^{-m_s}_{L_n,L_n}\Delta^2_{-m_s}\right] \\ &\times \sum_{m_j,m_l} (2j+1) \begin{pmatrix} j & l & 1/2 \\ -m_j & m_l & m_s \end{pmatrix}^2 \begin{pmatrix} l & 1 & l+1 \\ m_l & +1 & -m_n \end{pmatrix}^2. \quad (3.12) \end{aligned}$$

The second sum actually consists of just one term since $m = m_l + m_s$ and $m_n = m_l + 1$. Using properties of 3j-symbols, [17] the sum over m_s gives,

$$\mu^+ - \mu^- = -\frac{1}{\pi}\mathrm{Im} \sum_{m_n} \left[\tilde{G}^{\uparrow}_{L_n,L_n}\Delta^2_{\uparrow} - \tilde{G}^{\downarrow}_{L_n,L_n}\Delta^2_{\downarrow}\right] \frac{(-1)^{(j-j^+)}\,l\,C(m_n)}{3(2l+3)(2l+1)}, \quad (3.13)$$

where

$$C(m) = \frac{3(m-1)(l+m)(l+m+1)}{l(2l+1)(l+1)}. \quad (3.14)$$

If we now sum contributions from $j^{\pm}$ and neglect the j-dependence of the propagators and matrix elements, Eq. 3.13 gives zero signal due to the $(-1)^j$ factor. From physical considerations alone we expect to have zero XMCD signal when the SO splitting of the $j^{\pm}$ shells is zero, because then there is no connection between electron spin polarization and photon polarization. In order to take advantage of path symmetries, we can make use of the path-reversal symmetry property of $\tilde{G}_{L_1,L_2}$ above and cancel out all odd powers of m,

$$C\,(m) = \frac{3(2m^2 - l - 1)}{(2l+1)(l+1)}. \tag{3.15}$$

In addition to 1) path-reversal symmetry, ($\Gamma \rightarrow \Gamma^{-1}$), paths give the same contribution to the total propagator, if they transfer one into another under the operations of 2) rotations on any angle about the magnetization axis, and 3) reflections in the planes containing the magnetization axis and normal to it. These symmetries ignore the small phase shift due to magnetic flux, however all important paths for XAS are almost linear [24].

In order to take advantage of the XAFS code FEFF6 to calculate the XMCD signal χ^M, it is convenient to define a normalized, spin-dependent XAFS function,

$$\chi^M_{m_s} = (-)^{j-j_+}\frac{1}{\pi}\mathrm{Im}\sum_{m_n,\Gamma}\frac{C(m_n)}{2l+3}\tilde{G}^{m_s}_{L_n,L_n}(\Gamma)e^{2i\delta^c_{l_n,m_s}}\ , \tag{3.16}$$

as FEFF is designed to calculate the full propagator $\tilde{G}^{m_s}_{L_n,L_n}(\Gamma)e^{2i\delta^c_{l_n,m_s}}$ with the MS expansion. It is convenient at this point to distinguish several different quantities that appear in the XMCD formalism. In this work we will use as normalization factors the atomic cross-sections (denoted with a superscript A),

$$\mu^A = \frac{1}{2}(\mu^A_{\uparrow} + \mu^A_{\downarrow}) = -\frac{1}{\pi}\mathrm{Im}\,\frac{2j+1}{6(2l+1)}\left[G^{c,\uparrow}_{l\,0,l\,0}\Delta^2_{\uparrow} + \tilde{G}^{c,\downarrow}_{l\,0,l\,0}\Delta^2_{\downarrow}\right]. \tag{3.17}$$

The XMCD signal in Eq. 3.13 (denoted with superscript M) can be expressed as

$$\mu^M = \mu^+ - \mu^- = \mu^M_0 + \mu^M_S, \tag{3.18}$$

where μ^M_0 is the nearly smooth XMCD background arising from absorption within the central atom,

$$\mu^M_0 = \frac{(-1)^{(j-j^+)}\,l}{(2j+1)}\left(\mu^A_{\uparrow} - \mu^A_{\downarrow}\right), \tag{3.19}$$

and μ_S^M is the oscillating part of the XMCD signal, arising as in XAFS, from scattering by neighboring atoms,

$$\mu_S^M = \frac{(-1)^{(j-j^+)}\, l}{(2j+1)} \left[\mu_\uparrow^A \chi_\uparrow^M - \mu_\downarrow^A \chi_\downarrow^M\right]. \tag{3.20}$$

Because the matrix element factors $\mu_{\uparrow\downarrow}^A$ are spin dependent, the net XMCD effect is not simply due to the difference in $\chi_{\uparrow\downarrow}^M$. Similarly, the average XAFS signal from subshell j contains atomic matrix element factors and is given by

$$\begin{aligned} \Delta\mu &= \frac{1}{3}(\mu^0 + \mu^+ + \mu^-) - \mu^A = \frac{1}{2}\left[\mu_\uparrow^A \chi_\uparrow + \mu_\downarrow^A \chi_\downarrow\right] \\ &= \frac{-1}{\pi}\frac{(2j+1)}{6(2l+1)(2l+3)}\mathrm{Im}\sum_{m_n}\left[\tilde{G}^\uparrow_{L_n,L_n} e^{2i\delta^c_{l_n,\uparrow}}\Delta_\uparrow^2 + \tilde{G}^\downarrow_{L_n,L_n} e^{2i\delta^c_{l_n,\downarrow}}\Delta_\downarrow^2\right]. \end{aligned} \tag{3.21}$$

Experimentally a factor close to -2 has been found between the XMCD signals above the L_2 and L_3 edges.[30] This can be understood as follows. If one neglects the difference between the $j^\pm$ core wave functions, which is generally a good approximation, the following approximate results are obtained in terms of a generalized XAFS function $\chi_j = \Delta\mu_j/\mu_j^A$,

$$\begin{aligned} \mu_{j^+}^A(k) &\approx \frac{l+1}{l}\mu_{j^-}^A(k) \\ \Delta\mu_{j^+}(k) &\approx \frac{l+1}{l}\Delta\mu_{j^-}(k) \\ \chi_{j^+}(k) &\approx \chi_{j^-}(k) \\ \mu_{j^+}^M(k) &\approx -\mu_{j^-}^M(k) \\ \chi_{j^+}^M(k) &\approx -\frac{l}{l+1}\chi_{j^-}^M(k). \end{aligned} \tag{3.22}$$

Here

$$\chi_j^M \approx \frac{(-1)^{(j-j^+)}\, l}{(2j+1)}\left(\chi_\uparrow^M - \chi_\downarrow^M\right), \tag{3.23}$$

which should not be confused with $\chi_{m_s}^M$. Thus for $L_2(j=1/2)$ and $L_3(j=3/2)$ final states (both $l=1$), we obtain a factor of precisely -2.

For polycrystalline materials, averaging over all directions leads to $C(m)=1$ and hence from Eq. 3.16, $\chi_{\uparrow\downarrow}^M = \chi_{\uparrow\downarrow}$. This averaging significantly increases path symmetry

and Eqs. 3.16-3.20 simplify to a very compact form for the XMCD, namely

$$\mu^M = \mu^+ - \mu^- = \frac{(-1)^{j-j^+}\, l}{(2j+1)} \left(\mu_\uparrow - \mu_\downarrow\right). \tag{3.24}$$

We can then use *unpolarized* FEFF6 calculations to obtain the XMCD signal. Here $\mu_{\uparrow\downarrow} = \mu^A_{\uparrow\downarrow}(1+\chi_{\uparrow\downarrow})$ is the net j-edge absorption coefficient calculated with the potential for spin-up and -down electrons, respectively. This formula explicitly connects the XMCD signal to the spin polarization of the system. However, within the dipole approximation, the result gives no XMCD signal in nonmagnetic systems.

One can estimate the magnitude of the XMCD signal for polycrystalline materials using the single-scattering approximation and neglecting the difference between the background amplitudes $\mu^A_{\uparrow\downarrow}$. Then, using the exact curved-wave expression (or somewhat less accurately, the spherical wave approximation)[21] for the scattering amplitude at site i in Eq. 3.16-3.20, one obtains $\tilde{G}_{L,L} \approx \sum_i (e^{2i\rho_i}/\rho_i^2) f_i^{m_s}(\pi) e^{2i\delta^c_{l,m_s}}$, where the sum is over all neighbors to the absorber and $\rho_i = kR_i$:

$$\mu^M_S \approx \mathrm{Im}\frac{(-1)^{j-j^+}\, l}{(2j+1)} \mu^A \sum_i \frac{e^{2i\rho_i}}{\rho_i^2} \left[f_i^\uparrow(\pi) e^{2i\delta^c_{l_n,\uparrow}} - f_i^\downarrow(\pi) e^{2i\delta^c_{l_n,\downarrow}} \right]. \tag{3.25}$$

The term in square brackets can be interpreted as an effective magnetic scattering amplitude

$$f^M_{\mathrm{eff}} = f_i^\uparrow(\pi) e^{2i\delta^c_{l_n,\uparrow}} - f_i^\downarrow(\pi) e^{2i\delta^c_{l_n,\downarrow}}. \tag{3.26}$$

Note that f^M_{eff} arises partly from the magnetization of the scattering atom and partly from the central atom phase shift. Comparison of f^M_{eff} and the corresponding nonmagnetic scattering amplitude f_{eff} of XAFS shows that for Gd, f^M_{eff} is smaller by a factor which varies roughly inversely with k and out of phase by about $\pi/2$ (see chapter 8). One interpretation for this behavior is the derivative effect of the exchange energy difference between up- and down-spin populations; i.e., $(d\chi/dE)\Delta E \sim i\Delta E/k$. This result also explains the comparatively small amplitude of the XMCD signal at large photoelectron energies.

We can use Eq 3.24 to calculate the XMCD signal for Gd because the L_2-L_3 separation is approximately 700 eV and the two signals are well separated. However, when the SO splitting is small, for example in Mn where the L_2-L_3 splitting is 10 eV, one must sum over contributions from both $j^\pm$ channels. We can also neglect

the difference between matrix elements for $j = l \pm 1/2$ electrons (and the same core orbital wave function) since this is a good approximation when the SO interaction is small. Then the propagators differ only by a constant shift in energy $G^{j=1/2}(E) \approx G^{j=3/2}(E + E_{so})$. The same shift applies to the phase shifts $\delta^c_{l_n,m_s}$, so

$$\mu^M(E) \approx \mu^M_{j+}(E) - \mu^M_{j-}(E - E_{so}). \tag{3.27}$$

This expression can be used to estimate the XMCD signal far from the edge for elements like Mn, and again predicts an effect proportional to $1/k$ and a phase shift of about $\pi/2$.

3.4 Relativistic spin dependent theory

We now discuss the simultaneous treatment of SO interaction and spin dependent potentials. The extension of scattering theory is straightforward when one has only one of these two interactions. The SO interaction is naturally treated in the J-basis, so that the number of phase shifts doubles $\delta_\ell \to \delta_j$ ($j = \ell \pm 1/2$). Neglecting SO interaction for the spin dependent potentials also leads to the doubling of phase shifts $\delta_\ell \to \delta_{\ell,m_s}$, but a convenient extension of scattering theory is in the LS-basis. Their simultaneous treatment leads to the coupling of the Dirac equations for the same $m_j = m_\ell + m_s$. and different $m_s = \pm 1/2$ ($j = \ell \pm 1/2$).[31] Therefore, since we are interested in angular momentum up to $\ell = 25$, the average number of coupled equation for each ℓ is 25, which significantly increases computational time and effort. However the effect of both SO and spin interactions on phase shifts is rather small. Thus our calculations for Pu of $\delta_{\ell,j}$ (see Figure 7.5) give the largest difference in phase shifts for $l = 1$ about 0.45 radian and approximately constant in the whole energy range. It is approximately 0.1 radian for $\ell = 2$ and much less for larger ℓ and for the lighter elements. This leads to the expectation that an appropriate perturbation treatment of the SO interaction in final state and the spin dependent interaction should be sufficient for most of the problems. Remember also, that we are making a lot of other approximations (e.g. muffin-tin potential), so we should avoid unnecessary complexities, such as solution of coupled equation for each value of m_j. Such treatment will unreasonably increase computational time for small corrections.

I therefore want to suggest a modified perturbation treatment, which leads to the exact result, if one of the interactions is small. With this approach one has to solve the

Dirac equation only 4 times: for the total momentum $j = \ell \pm 1/2$ in the spin-up and -down potentials. Thus we will obtain a set of four phase shifts δ_{js} (for convenience I use $s = m_s$ in this section) for corresponding situations. Therefore the problem gets complicated only by a factor of 2 (compared to 25 in case of coupled equations approach) with respect to the relativistic spin-independent MS theory. Now I will show, how all ingredients of scattering theory should be modified.

First, let us consider the free propagator $G^0(r, r', E)$. Since the muffin-tin zero can be different for spin-up and -down potentials, the free propagator also will depend on the spin index, and an appropriate basis set is

$$|LS\rangle = |j_L(k_s), s\rangle \tag{3.28}$$

where $(k_s) = \sqrt{2(E - V_{mt}(s))}$. Second, the t-matrix can be effectively parameterized by

$$\begin{aligned} \langle LS|t|L'S'\rangle &= \langle LS|J\rangle \frac{1}{2}(t_{js} + t_{js'})\langle J|L'S'\rangle \delta_{\ell,\ell'}\,, \\ t_{js} &= \frac{e^{2i\delta_{js}} - 1}{-4\mathrm{i}\, k_s}, \end{aligned} \tag{3.29}$$

where on the right hand side $\langle J|LS\rangle$ are Clebsch-Gordon coefficients. Notice that states $|m_\ell = \ell, s = \uparrow\rangle = |j = \ell + 1/2, m_j = j\rangle$ and $|m_\ell = -\ell, s = \downarrow\rangle = |j = \ell + 1/2, m_j = -j\rangle$, are simultaneous eigenstates of j and s and are treated exactly. Third, the central atom radial matrix elements

$$\langle i|d_\epsilon|LS\rangle = \sum_j \langle i|d_\epsilon|Js\rangle\langle J|LS\rangle\,, \tag{3.30}$$

where the final state wave function $\langle \vec{r}|Js\rangle = R_{js}(r)\langle \Omega S|J\rangle$ has a separate dependence on radial and angular-spin coordinates. Fourth, the additional factor from normalization of radial wave function $e^{i\delta_\ell} \to e^{i\delta_{js}}$ in order to have a proper limit when potential is spin independent.

The final formula for cross section, combining all ingredients, is :

$$\begin{aligned} \sigma_{tot}(\omega, \epsilon, s) = -\frac{4\pi\, c}{\omega}\mathrm{Im} \sum_{i,JS,J'S'} \langle i|d^*_\epsilon|R_{Js}\rangle \\ \left[-i2k_s\, \delta_{Js,J's'} + e^{i(\delta_{js}+\delta_{j's'})} G^{sc}_{Js,J's'}(\omega + \epsilon_i)\right] \langle R_{J's'}|d_\epsilon|i\rangle \theta(\omega + \epsilon_i - \mu) \end{aligned} \tag{3.31}$$

where

$$\begin{aligned} G^{sc}_{Js,J's'}(E) &= \langle J|LS\rangle G^{sc}_{Ls,L's'}(E)\langle L'S'|J'\rangle \\ G^{sc}_{Ls,L's'}(E) &= G^{0}_{LS,L_1S}(-\rho_{i,s})\langle L_1S|t_i|L_1'S'\rangle G^{0}_{L_1'S',L'S'}(\rho_{i,s'}) + \cdots \end{aligned} \tag{3.32}$$

and $\rho_{i,s} = k_s(\vec{R}_i - \vec{R}_c)$. These formulas look exactly the same as the usual MS expression for cross section, except they have additional indices. This approximate approach will become exact if either SO or spin-dependent interaction is zero. Thus it should also have an appropriate perturbation expansion around these two points. In other words, this approach can fail only if both SO and spin-dependence are big. For real systems this situation will never happen, since SO interaction in the final state is big only for the $\ell = 1$ of actinides. However, their magnetic properties are determined by f-electrons and their exchange interaction with final p-electrons is expected to be small. This approach is therefore easy to implement in the existing codes, since all formulas are the same, only all the ingredients will have additional indices.

The neglect of SO in the final state gave a zero XMCD signal for $\ell = 0$ edges. A simple approximate expression can be derived for this case, using formula 3.31. Assuming, that SO is important only for the central atom, after the substitution of all 3j symbols one obtains

$$\sigma_c \approx \frac{1}{3}(\sigma^{\uparrow}_{3/2} - \sigma^{\downarrow}_{3/2} - \sigma^{\uparrow}_{1/2} + \sigma^{\downarrow}_{1/2})\,, \tag{3.33}$$

where σ^s_j is calculated by solving the Dirac equation for total momentum j and for spin-up or -down potential. This expression shows that XMCD signal for $\ell = 0$ edges is the second derivative effect in contrast to the signal for other edges, where XMCD is the first derivative effect. In the derivation of this formula it was important to get rid of the cross-terms. Therefore, since SO in the final state can be treated as a perturbation, I used the approximation for the cross product of reduced matrix elements,

$$R_{i,1/2}R_{i,3/2} = \frac{1}{2}(R^2_{i,1/2} + R^2_{i,3/2}), \tag{3.34}$$

where spin indices are suppressed. Equation 3.33 explicitly shows that one will get a zero signal if spin or SO interaction in the final state is neglected for $\ell = 0$. There is no additional complexity, if one wants to add the ℓ_z dependence of spherically symmetric scattering potential, which can arise due to the different filling of ℓ_z states

($\vec{L}$ wants to be along $\vec{S}$) and the Φ exchange interaction of a photoelectron with this electron density. Since both spin-orbit and exchange interaction are responsible for this dependence, the ℓ_z dependence of potential is expected to be even less important than SO interaction or spin dependence of potential.

$$V_{tot}(r) = V_0 + A\vec{L}\cdot\vec{S} + B\hat{S}_z + C\hat{L}_z \tag{3.35}$$

Therefore once again we solve the Dirac equation four times for extreme situations only:

$$\begin{aligned}
&1)\, V_{tot} = [V_0 + B/2 + C\ell] + A\vec{L}\cdot\vec{S};\; j = \ell + 1/2,\\
&2)\, V_{tot} = [V_0 - B/2 - C\ell] + A\vec{L}\cdot\vec{S};\; j = \ell + 1/2,\\
&3)\, V_{tot} = [V_0 + B/2 - C\ell] + A\vec{L}\cdot\vec{S};\; j = \ell - 1/2,\\
&4)\, V_{tot} = [V_0 - B/2 + C\ell] + A\vec{L}\cdot\vec{S};\; j = \ell - 1/2.
\end{aligned}$$

They can be labeled by (js) only, and all formulas remain the same. The difference is that we will add or subtract the ℓ_z dependent potential to four potentials discussed above, since $C \neq 0$. Again the first two cases will apply in the solution for two states, which are simultaneous eigenstates of m_ℓ, m_s, m_j. The last two situation are almost fulfilled for the states $|j_-, j_-\rangle$ and $|j_-, -j_-\rangle$, where $j_- = \ell - 1/2$. However, in the calculation by the formula for any state in LS-basis one will never use the "pure" j_- quantities.

3.5 Sum Rules

A connection between the integrated XMCD signal and the ground state value of the projection of orbital angular momentum on the magnetization axis was first derived by Thole et al.[32] Later Carra et al.[33] derived a second sum rule using graphical angular momentum techniques. There are many approximations in the derivation of these sum rules. There is even some arbitrariness in the choice of integration range and in the number of holes. All these troublesome features were analyzed by Wu et al.[34] They found from the band structure calculations, that the sum rules are valid to within 10%, and even within 5% if one deducts contributions from hybridization.

Below I will derive the same sum rules without graphical techniques, simply using analytical expressions for 3j symbols[35], in a manner similar to that used by Altarelli[36] for the first sum rule.

3.5.1 Derivation of sum rules

We start from Fermi's golden rule for the x-ray absorption coefficient within the independent electron approximation, having in mind band structure picture. In the dipole-approximation the absorption at the j-edge with polarization $\hat{\epsilon}$ is

$$\mu^j(\omega) = \frac{2\pi}{\hbar} \sum_{m_j,f}^{unocc} \langle j, m_j|\vec{p}\cdot\hat{\epsilon}^*|f\rangle\langle f|\vec{p}\cdot\hat{\epsilon}|j, m_j\rangle\, \delta(\omega - E_f + E_j)\,. \tag{3.36}$$

Integration over all ω is trivial. Using the completeness relation, that allows us to change the consideration from the unoccupied states to the occupied ones, we obtain for the integrated intensities,

$$\overline{\mu}^j = \int_{E_j^0}^{\infty} \mu(\omega) d\omega \tag{3.37}$$

$$\begin{aligned}\overline{\mu}^j = \frac{2\pi}{\hbar} \quad & \textstyle\sum_{m_j,m_l,m_s} \quad \langle j, m_j|l, m_l, s, m_s\rangle\langle l, m_l, s, m_s|\vec{p}\cdot\hat{\epsilon}^* \left(\hat{1} - \sum_f^{occ} |f\rangle\langle f|\right) \vec{p}\cdot\hat{\epsilon}\, \times \\ & \times \textstyle\sum_{m_l',m_s'} \quad |l, m_l', s, m_s'\rangle\langle l, m_l', s, m_s'|j, m_j\rangle. \end{aligned} \tag{3.38}$$

From the dipole selection rules we can only have transitions $l \to l' = l \pm 1$. We can rewrite Eq. 3.38 in terms of the one-particle density matrix,

$$\rho(\alpha;\beta) = \sum_f^{occ} \langle\alpha|f\rangle\langle f|\beta\rangle = \langle\Psi_0|c_\alpha^\dagger c_\beta|\Psi_0\rangle, \tag{3.39}$$

where $|\alpha\rangle$ is some complete set wave functions, which is chosen later to be a set of orthonormal orbital for central (absorbing) atom.

Without loss of generality we can restrict consideration to $\hat{\epsilon}_+$, $\hat{\epsilon}_-$ and $\hat{\epsilon}_0$ for right-circular, left-circular, and z-axis polarizations, defined as usual [17] ($\hat{\epsilon}_+ = -(\hat{x} + i\hat{y})/\sqrt{2}$, $\hat{\epsilon}_0 = \hat{z}$, $\hat{\epsilon}_- = (\hat{x} - i\hat{y})/\sqrt{2}$). From the Wigner-Eckart theorem we obtain

$$\overline{\mu}_\epsilon^j = \frac{2}{3}\pi\hbar(2j+1)\left[\int dr R_j(r)\left(\frac{-\partial^2}{\partial r^2} + \frac{l(l+1)}{r^2}\right)R_j(r) - \sum_{nl',n'l'',all\,m} 3\sqrt{l'_> l''_>}\right.$$

$$\times R_{j,n'l''}R_{j,nl'}\,\rho(n'l'',m_l,m_s;nl',m_l',m_s')\,(-)^p \begin{pmatrix} l & 1/2 & j \\ m_l-\epsilon & m_s & -m_j \end{pmatrix} \quad (3.40)$$
$$\times \begin{pmatrix} l & 1 & l'' \\ -m_l+\epsilon & -\epsilon & m_l \end{pmatrix} \begin{pmatrix} l' & 1 & l \\ -m_l' & \epsilon & m_l'-\epsilon \end{pmatrix} \begin{pmatrix} l & 1/2 & j \\ m_l'-\epsilon & m_s' & -m_j \end{pmatrix} \Bigg],$$

where $p = m_l - m_l' + (l''-l')/2$; $\epsilon = +1,\ -1$ and 0 for the absorption of right-circular, left-circular and z-axis polarized x-rays; $l_>'$ is the larger of l or l'; n is the principal quantum number; $R_j(r)$ are radial wave functions multiplied by r; and dipole matrix elements, evaluated in ∇ form, are $R_{j,nl'} = \int dr\, R_j(r)\{\partial/\partial r - [l(l+1) - l'(l'+1)]/2r\}\, R_{nl'}(r)$.

Equation 3.40 is the principal result, because given the density matrix for the ground state for any theoretical model, we can calculate experimentally measurable integrated intensities and thereby check the validity of that model. Furthermore we can make some approximations to obtain sum rules which show more explicitly the connection between integrated intensities and ground state properties.

Here we neglect possible cross terms due to hybridization (e.g. between 3d and 4s), because they are suppressed by the ratio of the dipole matrix elements $R_{j,l-1}/R_{j,l+1}$, and we suppose that only one nl shell is partly filled for each l. If we have several $l+1$ shells with non-negligible partial filling, then our sum rules can still be valid if the dipole matrix element for one transition nl' is much larger than the others.

The sum over all m for the completely filled shells can be done analytically. If we can make the assumption for the partly occupied shells that the transition amplitude to the one of them (nl') is much larger than to the others or that the density matrix elements for other shells are negligible, then we obtain

$$\overline{\mu}_\epsilon^j = A^j + 2\pi\hbar(2j+1)l_> R_{j,nl'}^2 \sum_{all\,m} [1-\rho(nl',m_l,m_s;nl',m_l',m_s')](-)^{m_l-m_l'} \quad (3.41)$$
$$\times \begin{pmatrix} l & 1/2 & j \\ m_l-\epsilon & m_s & -m_j \end{pmatrix} \begin{pmatrix} l & 1 & l' \\ -m_l+\epsilon & -\epsilon & m_l \end{pmatrix} \begin{pmatrix} l' & 1 & l \\ -m_l' & \epsilon & m_l'-\epsilon \end{pmatrix} \begin{pmatrix} l & 1/2 & j \\ m_l'-\epsilon & m_s' & -m_j \end{pmatrix}.$$

The radial matrix elements A^j can be obtained from atomic calculations,

$$\begin{aligned} A^j &= \frac{2}{3}\pi\hbar(2j+1)\Bigg[\int dr R_j^*(r)\left(\frac{-\partial^2}{\partial r^2} + \frac{l(l+1)}{r^2}\right)R_j(r) \\ &- \sum_{nl'j'}^{occ'} R_{j,nl'j'}^2\, l_>(2j'+1)\begin{Bmatrix} 1 & j' & j \\ 1/2 & l & l' \end{Bmatrix}^2\Bigg], \end{aligned} \quad (3.42)$$

where occ' means the sum over fully occupied shells and the important partly occupied (nl') shell. The contribution from the $l \rightarrow l-1$ transitions is usually an order of magnitude less important and can often be neglected. However, we have enumerated the sum rules for both $l' = l \pm 1$. Usually we have only one partly filled nl-shell, for which we can neglect the difference of the $nlj_{\pm}$ wavefunctions, where $j_{\pm} = l \pm 1/2$. These results imply that we can connect the j and ϵ dependence of the integrated absorption with ground state values of various operators. From the six possible integrated intensities (3 polarizations times 2 for $j_{\pm}$) we can extract six linearly independent operators $\hat{O}(j, l', \epsilon)$. These operators can be found after substitution of the analytic expressions for 3j symbols taken from any source.[17] After tedious but straightforward algebra, where the main trick was to reexpress all square roots from 3j symbols in terms of raising and lowering operators, we find that

$$\overline{\mu}_{\epsilon}^{j} = A^{j} + \pi\hbar \frac{\langle \hat{O}(j, l', \epsilon) \rangle R_{j,nl'}^{2}}{(2l+1)^{2}(2l'+1)}, \tag{3.43}$$

where the expectation value $\langle \hat{O}(nl') \rangle$ means

$$\langle \hat{O}(nl') \rangle = \sum_{all\, m} \langle nl', m_l', s, m_s' | \hat{O} | nl', m_l, s, m_s \rangle \rho(nl', m_l, s, m_s; nl', m_l', s, m_s') \,, \tag{3.44}$$

and $\hat{O}(j, l', \epsilon)$ are given in Table 3.1 as an operator expansion,

$$\hat{O}(j, l', \epsilon) = \sum_{i} c_i(j, l', \epsilon) \hat{O}_i \,, \tag{3.45}$$

where

$$\begin{aligned}
\hat{O}_1 &= \hat{1} \cdot 2N_h l_> (2l+1)/(3N_e), \\
\hat{O}_2 &= (-)^k l_z (2l+1), \\
\hat{O}_3 &= l_z^2 - \hat{1} \cdot l'(l'+1)/3, \\
\hat{O}_4 &= 2l(l+1)[s_z + (-)^{k+1}(l_z \vec{l} \cdot \vec{s} + \vec{l} \cdot \vec{s}\, l_z)/l_>], \\
\hat{O}_5 &= 2\vec{l} \cdot \vec{s}\, l(l+1)/l_>^2, \\
\hat{O}_6 &= 2l_z \vec{l} \cdot \vec{s}\, l_z + (-)^{k+1} 2 l_z s_z (l+1),
\end{aligned} \tag{3.46}$$

where all angular momentum operators are in the units of $\hbar$; $k = (l+1-l')/2$, and N_e and N_h are the number of electrons and holes in the nl' shell.

Table 3.1: Coefficients $c_i(j,l',\epsilon)$ in the operator expansion $\hat{O}(j,l',\epsilon) = \Sigma_i c_i(j,l',\epsilon)\hat{O}_i$. The operators $\hat{O}_i$ are defined in the text. O_1 is a number of holes operator, O_2 is a projection of angular momentum, etc.. $l_> = max[l,l']$.

$i=$	1	2	3	4	5	6
$c_i(j_+,l',+1)$	$l+1$	$-(l+1)$	$-(l+1)$	$+1$	$-l(l+1)$	-1
$c_i(j_-,l',+1)$	l	$-l$	$-l$	-1	$+l(l+1)$	$+1$
$c_i(j_+,l',0)$	$l+1$	0	$2(l+1)$	0	$-2l_>^2$	$+2$
$c_i(j_-,l',0)$	l	0	$+2l$	0	$+2l_>^2$	-2
$c_i(j_+,l',-1)$	$l+1$	$l+1$	$-(l+1)$	-1	$-l(l+1)$	-1
$c_i(j_-,l',-1)$	l	l	$-l$	$+1$	$+l(l+1)$	$+1$

We note that normalized integrated cross-sections can be defined by dividing out the radial matrix element, i.e.,

$$\chi_\epsilon^j = \frac{\overline{\mu}_\epsilon^j - A^j}{2\pi\hbar R_{j,nl'}^2}\,. \tag{3.47}$$

Thus making appropriate linear combinations we can construct the following sum rules:

$$\rho = \frac{(\chi_+^{j_+} - \chi_-^{j_+}) + (\chi_+^{j_-} - \chi_-^{j_-})}{N} = \frac{(-)^{k+1}\langle l_z\rangle}{N_h\, l_>}\,, \tag{3.48}$$

$$\begin{aligned}\delta &= \frac{(\chi_+^{j_+} - \chi_-^{j_+}) - (1+1/l)(\chi_+^{j_-} - \chi_-^{j_-})}{N} \\ &= \frac{\langle 2(l+1)[s_z + (-)^{k+1}(l_z\vec{l}\cdot\vec{s} + \vec{l}\cdot\vec{s}\,l_z)/l_>]\rangle}{N_h(2l+1)l_>}\,,\end{aligned} \tag{3.49}$$

$$\begin{aligned}\gamma &= \frac{(\chi_+^{j_+} + \chi_-^{j_+} - 2\chi_0^{j_+}) + (\chi_+^{j_-} + \chi_-^{j_-} - 2\chi_0^{j_-})}{N} \\ &= \frac{-3\langle l_z^2\rangle + l'(l'+1)N_e}{N_h(2l+1)l_>}\,,\end{aligned} \tag{3.50}$$

$$\begin{aligned}\beta &= \frac{(\chi_+^{j_+} + \chi_-^{j_+} - 2\chi_0^{j_+}) - (1+1/l)(\chi_+^{j_-} + \chi_-^{j_-} - 2\chi_0^{j_-})}{N} \\ &= \frac{-\langle 2(l_>^2-1)\vec{l}\cdot\vec{s} - 6l_z\vec{l}\cdot\vec{s}\,l_z + (-)^k 6(l+1)l_z s_z\rangle}{N_h(2l+1)l_> l}\,,\end{aligned} \tag{3.51}$$

$$\alpha = \frac{(\chi_+^{j_+} + \chi_-^{j_+} + \chi_0^{j_+}) - (1+1/l)(\chi_+^{j_-} + \chi_-^{j_-} + \chi_0^{j_-})}{N}$$
$$= \frac{-2(l+1)\langle \vec{l}\cdot\vec{s}\rangle}{N_h\, l\, l_>}\,, \tag{3.52}$$

$$N = (\chi_+^{j_+} + \chi_-^{j_+} + \chi_0^{j_+}) + (\chi_+^{j_-} + \chi_-^{j_-} + \chi_0^{j_-})$$
$$= N_h l_>/(2l'+1)\,. \tag{3.53}$$

Following the classification of the six fundamental spectra in X-ray photoemission spectroscopy,[37] we can assign names for the sum-rules as follows: orbit (ρ), spin (δ), anisotropic orbit (γ), anisotropic spin magnetic (β), spin orbit (α) and isotropic (N). Note that for $l = 0$ we do not have j_- terms and we can use only the three sum rules for ρ, γ and N.

Thus the problem of normalization in using the sum rules[34] can be overcome by using atomic calculations, assuming absolute measurements of $\mu_{\pm,0}$ can be made. Note that in first four sum rules we don't even have to know number of holes, nor calculate A^j, because these factors cancel out in the final expressions. The use of last two sum rules does depend on the calculation of A_j and also on how well absorption from two edges can be separated. When two edges are very close in energy, the sum rule for α is probably useless, due to the ambiguity in the separation of $\overline{\mu}_\epsilon^{j\pm}$.

The first two sum rules for ρ and δ are the same as in the original papers,[32, 33] but they are corrected for the case when one cannot neglect the difference between the $j_\pm$ wavefunctions. An overall '$-$' sign in our formulas is due to our opposite definition of right- and left-circular polarization directions. Our convention is that light going in the positive z-direction with right-circular polarization is the polarization causing the transition $\Delta m = +1$. This sign is important, because otherwise, values of $\langle L_z\rangle$ and $\langle S_z\rangle$ extracted from experiment values could have the wrong sign. In order to compare with Carra et.al. [33], we have to express the operator $T_z = \Sigma_i t_{z,i}$ in terms of our operators. This can be done within one l-shell as:

$$(2l+3)(2l-1)\langle l, m_l, s, m_s|t_z|l, m_l', s, m_s'\rangle = \langle l, m_l, s, m_s|$$
$$-2l(l+1)s_z + 3(l_z(l\cdot s) + (l\cdot s)l_z)|l, m_l', s, m_s'\rangle. \tag{3.54}$$

Substituting this equation into the expression for δ in Ref. [33] for the $l \rightarrow l'$ transition

($c = l, l = l'$), we recover the same result.

The third and forth sum rules (γ and β) were derived earlier for linear dichroism signal by Carra et al.[38] These two sum rules show, that the assumption $\overline{\mu}_+ + \overline{\mu}_- = 2\overline{\mu}_0$ is generally invalid, even for integrated intensities. This equality can hold in special cases however, e.g., for the model when the density matrix for an open shell is $\rho(m_l, m_s; m_l', m_s') = \delta_{m_l,m_l'}\delta_{m_s,m_s'}\delta_{m_s,1/2}N_e/(2l+1)$, $[N_e < (2l+1)]$. This model predicts all sums to be zero except the second and the last one. For Gd, which has a half-filled f-shell with all spins up, this model should work and gives $\delta = -1/3$, in agreement with experiment and the prediction by Carra et al.,[33] who had to assume all spins down to get the same '$-$' sign.

3.5.2 Discussion

We have derived a complete set of independent sum rules for polarization dependent x-ray absorption based on the independent electron approximation and the dipole approximation for transition rates. Our results are stated in terms of the density matrix. Thus they apply to both atomic and extended systems, and accordingly the number of holes need not be an integer. The previously derived sum rules are improved by the explicit inclusion of dipole matrix elements. We have also shown that the problem of the arbitrary range of integration in the previously derived sum rules can be overcome with the help of atomic calculations (and absolute measurement of μ).

We do not make the additional assumption that radial matrix elements are constant for all transitions, as in Ref.[32, 33]. Instead, we assume that one partly filled shell is important, either because the transition amplitude to the other shells is much smaller or the occupation number of the other shells is small. This assumption is generally satisfied.

Changing the direction of light, one can obtain more information. For example all 3 components L_x, L_y and L_z can be obtained, if one send the x-ray beam along x, y and z axis.

Magnetic materials are usually described by spin-resolved band structure, where the density matrix is diagonal. Thus, if one can do spin-resolved measurements (SPXAS), the actual number of sum rules is multiplied by 2. Since they were derived in a non-relativistic limit, they will be valid for each spin direction separately.

Therefore a number of experimentally extracted quantities can be compared with the results of spin-resolved band structure calculations. For example, the spin contribution to the net magnetization can be obtained from the polarization average SPXAS signal.

$$S_z = -\frac{1}{2}\left[N_h(\uparrow) - N_h(\downarrow)\right]. \tag{3.55}$$

Then one does not have to rely on the cancelation of operator T_z to extract S_z from the sum rule δ. Actually the cancelation of T_z can be checked experimentally.

The main uncertainty in these sum rules comes from the $l \rightarrow l-1$ dipole transitions and the neglect of the quadrupole transitions for the heavier elements. Hybridization tends to increase this uncertainty, due to the even smaller power of the transition amplitudes ratio involved. The applicability of the sum rules can be checked with atomic or band structure calculations. Even if the conditions for approximate use of sum rules are not met, the integrated intensities can still be used to extract information about the density matrix and ground state properties from equation (3.40), but the connection will not be as clear as that stated in sum rules.

Chapter 4

MANY-BODY EFFECTS IN X-RAY ABSORPTION

A rule of thumb in theoretical solid state physics says: "Consider the single electron theory first, if it does not explain the phenomenon, look for the many-body correction." Actually, many-body theory was already implicitly used to calculate the photoelectron mean free path. This is the main quantity single electron theory fails to predict and is essential for validity of modern XAFS theory. Early comparison of single electron calculation of cross section with experiment showed also the wrong peak-to-peak distance in XANES region, and the need of overall reduction factor S_0^2. All these quantities and some other effects are naturally accounted for by the many-body theory.

4.1 Sudden approximation and excitation spectrum

It is easy to generalize the formal expression for cross section to the full N-body case, using Fermi's Golden rule:

$$\sigma_{tot}(\omega) = \frac{4\pi^2 e^2}{cm^2\omega} \sum_{I,F} |\langle F|\hat{D}_\epsilon|I\rangle|^2 \, \delta(E_F - E_I - \omega) \quad , \tag{4.1}$$

where capital letters I and F stand for the many-body initial and final state. The many-body dipole operator $\hat{D}$ can be expressed through the single electron dipole matrix elements using second quantization notation:

$$\hat{D}_\epsilon = \sum_{i,f} d_{i,f} a_f^\dagger a_i \quad , \tag{4.2}$$

where operator a_i destroys electron in state i, and $a_f^\dagger$ creates electron in state f. States i and f should form complete basis sets (not necessarily the same). However, it is impractical to calculate exact I and F for the N particle Hamiltonian. Therefore, additional approximations are necessary. Further, I will use separable or sudden approximation. Qualitatively, it is justified if the photoelectron leaves atom in a time

a_0/v_F ($v_F = \hbar k_F/m$) much faster than the core-hole relaxation time $\hbar/\Gamma_{ch}$. For the typical metal this leads to condition:

$$\Gamma_{ch} \ll \frac{\hbar^2 k_F}{m\, a_0} \approx \frac{2}{r_s}\mathrm{Ryd} = 10 - 25eV \quad . \tag{4.3}$$

Typically, $\Gamma_{ch} \leq 3eV$, and this inequality is well satisfied . Thus sudden approximation is justified. The opposite approximation, which is often used to investigate optical properties ($\hbar\omega \leq 3eV$), is the adiabatic approximation. [39] Here the electronic system follows the external potential.

Within the separable approximation, the N-particle Hamiltonian for the final state is separated into the Hamiltonian for $(N-1)$ particles and the effective one electron Hamiltonian for photoelectron h:

$$H_N = H'_{N-1} + h \quad . \tag{4.4}$$

The dynamics of the $(N-1)$ particle system are assumed to be independent of the photoelectron energy, and the effective potential for photoelectron is calculated with some fixed charge density of $(N-1)$ electrons.

$$h = -\frac{\nabla^2}{2} + V_{coul}^{N-1} + \Sigma_{xc}(E, \rho(r)) \quad , \tag{4.5}$$

where $\rho(r)$ within sudden approximation is given by the initial density with subtraction of the density from core-hole orbital. The Coulomb potential can be calculated from this density. The last quantity $\Sigma_{xc}(E, \rho(r))$ is the self-energy, which reduces to the ground state exchange-correlation potential at the Fermi level.[40] Self-energy has a smooth energy dependence. The definition of the self-energy and it's models will be discussed later in this chapter. In order to find the photoelectron's Green's function a Dyson equation should be solved. (This is like Schrödinger equation, but employs a complex energy dependent self-energy).

$$h(E)\phi_{ph}(E) = E\,\phi_{ph}(E) \quad . \tag{4.6}$$

The initial and final wave functions also separated

$$\begin{aligned} |I\rangle &= |\phi_c\rangle|\Psi_0^{N-1}\rangle \\ |F\rangle &= |\phi_{ph}\rangle|\psi_n^{N-1}\rangle \quad , \end{aligned} \tag{4.7}$$

where $|\phi_{ph}\rangle$ is an eigenstate of the H_{N-1} with energy E_n. Within the sudden approximation the final state wave function is known . Since the rest of the electrons are assumed to keep their orbitals, it is just $|\Psi_0^{N-1}\rangle$ but it is not an eigenstate of H_{N-1} and thus can be decomposed in terms of eigenstates. Therefore absorption coefficient is given by:

$$\sigma_{tot}(\omega) = \frac{4\pi^2 e^2}{cm^2\omega} \sum_{n,k} |\langle \Psi_0^{N-1} | \psi_n^{N-1} \rangle|^2 \, |\langle \phi_c | \hat{d}_\epsilon | \phi_p h \rangle|^2 \, \delta(E_{ph} + E_n - E_I - \omega) \,, \qquad (4.8)$$

where $E_F = E_n + E_{ph}$ is total energy of the final state. The sum of overlap integrals is unity:

$$\sum_n S_n^2 = \sum_n |\langle \Psi_0^{N-1} | \psi_n^{N-1} \rangle|^2 = 1 \quad . \qquad (4.9)$$

The remarkable feature is that in atoms and molecules one of S_n^2 (usually the lowest) dominates: $S_0^2 > 0.75$. In the atomic picture this happens for the configuration with the same sets of quantum numbers of orbitals.

Therefore, it is convenient to take this dominant channel as a reference point and define an excitation spectrum as:

$$\rho(\omega) = \sum_n S_n^2 \, \delta(\omega - E_n + E_0) \quad . \qquad (4.10)$$

A typical atomic excitation spectrum consists of few delta peaks above zero (shake-up processes) and a smooth tail due to final states in continuum (shake-off processes).

For the solid state all $(N-1)$ orbitals will be slightly affected by the creation of a core-hole. The effect will be extremely small for the delocalized orbitals, since they are spread throughout the whole system, and hence the changes of localized orbitals will be similar to those of atomic system. One can probably neglect the changes of localized orbitals on all the atoms except the central. However, the solids have continuous energy spectrum and the delta-peak corresponding to S_0^2 will be spread out through the finite energy range. Thus in principle one will get the Anderson orthogonality catastrophe:

$$S_0^2 \propto 1/V \to 0 \quad . \qquad (4.11)$$

However, the excitation spectrum can still have a large "quasiparticle" peak at the origin. The weight for this peak can be still estimated from the embedded atom picture.

Thus the total absorption coefficient is given by the convolution of the excitation spectrum, and the absorption coefficient calculated for dominant channel (σ) :

$$\sigma_{tot}(\omega) = \int d\omega' \sigma(\omega') \rho(\omega - \omega') \quad , \tag{4.12}$$

where

$$\sigma(\omega) = \frac{4\pi^2 e^2}{cm^2 \omega} \sum_k |\langle \phi_c | \hat{d}_\epsilon | \phi_p h \rangle|^2 \, \delta(E_{ph} + E_0 - E_I - \omega) \, . \tag{4.13}$$

This equation looks the same as in the single electron theory, except that the photoelectron wave function is calculated by the Dyson equation with self-energy. Sometimes even the effective potential for the photoelectron is calculated with the final state Ψ_0^{N-1} in order to account for the screening of core-hole Coulomb potential. This is currently done in our program FEFF, despite the fact that it looks more appropriate to just subtract core-hole density from initial electron density within sudden approximation . The long range Coulomb interaction may be important for the near edge structure. Even bound states of photoelectron can appear (excitonic states), but since in this case photoelectron does not go away from core hole, the screened potential should be used. The time scale of screening is determined by plasmon frequency, which is typically 10-20 eV. Thus for a photoelectron close to Fermi energy the screening time is comparable with the time needed to leave absorbing atom. Therefore only in EXAFS region screening of core-hole can be neglected. The consistent treatment of screening goes beyond the sudden approximation, and complications to the theory will be discussed at the end of this chapter.

4.1.1 Atomic model for excitation spectrum

An exact calculation of the excitation spectrum is computationally intractable at present, and probably not necessary for the x-ray absorption, since a convolution should be made. Therefore an approximate model for excitation spectrum may be enough, if one is not interested in its details (e.g. as in photoelectron energy loss spectra, measured in XPS). Atomic calculations can give estimates for two important parameters of the excitation spectra: the weight of peak at the origin of excitation spectrum (S_0^2) and the relaxation energy (E_R). One needs to calculate the central atom orbitals and the total energy with and without core-hole. The first parameter is estimated by

$$S_0^2 = |\det M_{i,j}|^2 \quad , \tag{4.14}$$

where $M_{i,j} = \langle i|j\rangle$ is the $(Z-1)\times(Z-1)$ matrix of overlap integrals (Z is the atomic number in periodic table). This matrix has all diagonal terms close to 0.99 and all off-diagonal terms close to zero (less than 0.1 or often exact zero due to symmetry).

The atomic estimate for the edge position is given by difference in the total atomic energies, calculated with and without core-hole ($E_{edg} = E_w - E_{wo}$). If the atomic orbitals are frozen during transition (sudden approximation), then excitation energy is given by the Koopman's theorem:

$$E_{fr} = -\epsilon_c \quad . \tag{4.15}$$

This is just negative eigenenergy for the core-hole orbital, calculated *without* core-hole. This energy is the average edge position for all channels.

$$\begin{aligned} E_{fr} &= \langle \Psi_I^{N-1}|H_{N-1}|\Psi_I^{N-1}\rangle - E_{wo} = \\ &= E_{edg} + \sum_n S_n^2(E_n - E_w) = E_{edg} + \int d\omega\rho(\omega)\omega \quad . \end{aligned} \tag{4.16}$$

Therefore the first moment of excitation spectrum, which can be interpreted as the relaxation energy, is given by

$$E_R = E_{fr} - E_{edg} = \int d\omega\rho(\omega)\omega \quad . \tag{4.17}$$

The simplest excitation spectrum model, based on two atomic parameters S_0^2 and E_R, is

$$\rho(\omega) = S_0^2\delta(\omega) + (1 - S_0^2)\frac{e^{-E/E_d}}{E_d} \quad , \tag{4.18}$$

where the distribution parameter $E_d = E_R/(1 - S_0^2)$ is found from the value of the first moment. The exponential tail was chosen arbitrarily, but it is very convenient for a fast numerical convolution in the energy space. This model is implemented as an option in the FEFF7 code, and can be important for the extraction of more accurate coordination number. A free parameter in EXAFS formula (S_0^2) is fixed by this calculation. Therefore one should use only $S_0^2 = 1$ after the convolution with excitation spectrum. The amplitude of the first peak in Fourier transform will be directly connected with the average number of nearest neighbors. Application of this model is discussed in the Chapter 6.

4.2 Self-energy and GW approximation

Within sudden approximation the x-ray absorption problem separates into independent consideration of the photoelectron propagation in solid and the core-hole dynamics. The latter is assumed independent of all eigenstates of $(N-1)$ electrons, and determined by the radiative decay. Thus the core-hole dynamics is described by a single parameter – the core-hole lifetime – which is well known experimentally. The core-hole excitation spectrum can also be found from the experiment or estimated from the atomic calculations, described above. Therefore, if one knows how to calculate the photoelectron's Green's function, then the many-body calculations of XAS within sudden approximation can be done.

Photoelectron propagation is connected to the central quantity of many-body theory – the one particle Green's function. Due to causality principle, all experimentally measured quantities (as well as absorption coefficient) are related to the retarded Green's functions

$$G(xt,x't') = -i\theta(t-t')\langle\Psi^\dagger(xt)\Psi(x't') + \Psi(x't')\Psi^\dagger(xt)\rangle \quad , \tag{4.19}$$

where $x = (\vec{r},s)$ is abbreviation for space and spin coordinates, and brackets can be generalized for the thermodynamic average (see Matsubara technique in Mahan's book [18]). The important feature of this expression is that, it has a simple equal time limit

$$\lim_{t\to t'}\langle\Psi^\dagger(xt)\Psi(x't') + \Psi(x't')\Psi^\dagger(xt)\rangle = \delta(x-x')\,. \tag{4.20}$$

As one can see, this retarded Green's function coincides with the total Green's function used in MS theory within single electron approximation. Indeed, it can be shown using second quantization formalism, that the expression for cross section will look the same, except the many body retarded Green's function replaces single electron Green's function of MS theory.

The time evolution of Green's function is determined by Hamiltonian of the system which for real solid state system is known, at least in principle, from the QED theory. It consists only of the Coulomb interaction between electrons and nuclei and the interaction with external electro-magnetic fields. Using the fundamental commutation relations for fermions, one can derive equation of motion for the Green's

function:

$$[E + \frac{\nabla^2}{2} - V_{coul}(r)]G(x,x',E) - \int \Sigma(x,x",\omega)G(x",x',E) = \delta(x,x')\,, \qquad (4.21)$$

where the self-energy is defined by a set of equations (see Eq. 13-19 in Hedin-Lundqvist review and it's derivation [19, p.34-37]). In principle, the self-energy is an infinite sum over the functionals of G and bare Coulomb interaction v. One assumes, that this sum converges, and terminates it at some point. The neglect of vertex corrections leads to a simplified expression for self-energy Σ:

$$\begin{aligned} P(12) &= -iG(12)G(21) \\ W(12) &= v(12) + \int d(34)W(13)P(34)v(42) \\ \Sigma(12) &= iW(1^+2)G(12) \quad , \end{aligned} \qquad (4.22)$$

where 1 stands for (x_1, t_1). It is also convenient to reexpress the relation between screened and bare Coulomb potential through a dielectric constant, which is also experimentally accessible

$$\begin{aligned} \epsilon(12) &= \delta(12) - \int P(32)v(13)d(3) \\ W(12) &= \int v(13)\epsilon^{-1}(32)d(3) \quad . \end{aligned} \qquad (4.23)$$

Actually, there is no small parameter that justifies this GW approximation for Σ. However, several important points of GW approximation should be mentioned.

- If one neglects screening of Coulomb potential (W=v), then GW goes to the widely used HF approximation.

- Careful consideration of screening, rather than the perturbation expansion, led to the improvements of uniform electron gas theory.

- GW picks up both contributions from poles of the Green's function and inverse dielectric function, which can be considered due to the dynamic screening exchange and the Coulomb hole correspondingly.

Thus all important physics of the screening is described by the GW approximation. The next terms in expansion for Σ cannot change qualitative results, however they

can change the numerical results of calculations. Also GW can be used to construct ϵ_{xc} for the use in LDA [40], due to the result for uniform electron gas:

$$V_{xc}(r_s) = \Sigma(k_F, E_F)\,. \tag{4.24}$$

Also in practice the GW equation are not solved self-consistently, since Σ is usually small compared to Coulomb potential. The general procedure is

1. Find filled single electron orbitals. It is obvious for uniform electron gas, and require to find band structure with your favorite method for crystals.

2. Calculate G_0 from the single electron theory, and use it to calculate the irreducible polarization tensor P and inverse dielectric function ϵ^{-1}. This is interesting by itself, since it is connected with optical and microwave light properties and elementary excitations such as plasmons in metals.

3. Now W and Σ can be calculated and used in turn to determine an improved Green's function by solving the Dyson equation. By doing this, one effectively obtains new band structure or quasiparticle dispersion relation.

Note that expression for ϵ^{-1} 4.23 is exactly the well known RPA result,[41] if G_0 is used instead of G. One can use an improved new G back in stage 2, but usually it does not lead to further improvement. Also it was found for the uniform electron gas that the corrections from such renormalization of Green's function tend to cancel with the vortex corrections [42]. Therefore one step G_0W approximation is usually enough. Such scheme has been implemented in a number of band structure calculations.[43, 44] GW calculations represent one of the ways to look for improvements beyond extremely popular LDA calculations.

4.2.1 GW for uniform electron gas

In the FEFF code we use GW results for the uniform electron gas to estimate Σ. Such procedure was first suggested by Sham and Kohn, [40] and is based on short range properties of Σ. Such procedure has practically the same foundation as LDA theory for ground state exchange-correlation potential.

For uniform electron gas the set of occupied orbitals is just plane waves with momentum up to $k = k_F$. Neglecting screening ($W = v$), leads to a simple calculation first done in 1930 by Dirac.[45]

$$\Sigma_x(k) = -\frac{e^2 k_f}{\pi}\left[1 + \frac{1-x^2}{2x}\log\left|\frac{1+x}{1-x}\right|\right] \quad , \tag{4.25}$$

where $x = k/k_f$. This is known to be a very unsatisfactory model for the theory of metals, since it gives a zero density of states at the Fermi level and logarithmic singularities. This is clear from the dispersion relation

$$E(k) = \frac{k^2}{2m} + \Sigma_x(k) \tag{4.26}$$

and a singular behavior of Σ at the Fermi level. However, if one follows the GW procedure described above, no singularities appear and DOS remains finite.

Step 2 of G_0W algorithm was done also long ago, and the result for ϵ^{-1} is the well known Lindhard dielectric function [46]

$$\epsilon_L(q,\omega) = 1 + \frac{\alpha r_s}{\pi q^3}\left[2q + f\left(q + \frac{\omega + i\delta}{q}\right) + f\left(q - \frac{\omega + i\delta}{q}\right)\right] , \tag{4.27}$$

where

$$f(z) = (1 - \frac{z^2}{4})\,\ln[(z+2)/(z-2)], \tag{4.28}$$

and $\alpha = (4/9\pi)^{1/3} = 0.521$, $r_s = (\frac{3}{4\pi}\rho)^{1/3}$. For convenience, q is in units of Fermi momentum, ω is in units of Fermi energy, and r_s is in bohrs.

The last step was done in 1965 by Hedin [47], where he introduced the single plasmon approximation for the dielectric function:

$$\epsilon^{-1}(q,\omega) = 1 + \frac{\omega_p^2}{\omega^2 - \omega_p^2(q) + i\delta} \quad , \tag{4.29}$$

where the coefficient is chosen to satisfy sum rules for ϵ^{-1}

$$\int \omega\,\mathrm{Im}\,\epsilon^{-1}(\omega,q)d\omega = -\frac{\pi}{2}\omega_p^2 \quad . \tag{4.30}$$

The plasmon dispersion relation is approximated by

$$\omega_p^2(q) = \omega_p^2 + \frac{1}{3} v_F(\omega_p) q^2 + \left(\frac{1}{2m} q^2\right)^2 \quad , \tag{4.31}$$

where the coefficients are chosen so that the dispersion curve is close to that found from the Lindhard dielectric function. Thus $\omega_p^2 = \omega_p^2(0) = 4\pi n e^2/m$, with n being the uniform density. This model is very popular, since it is easy to calculate. Using this type of dielectric function, integration over frequency leads to

$$\Sigma_{HL}(\omega, \vec{k}) = -\frac{1}{(2\pi)^3} \int dq \frac{v_{\vec{q}} n_{\vec{k}+\vec{q}}}{\epsilon(q, \epsilon_{\vec{k}+\vec{q}} - \omega)} - \frac{\omega_p^2}{(2\pi)^3} \int \frac{v(q)}{2\omega_p(q)} \frac{dq}{w_p(q) + \omega - \epsilon_{\vec{k}+\vec{q}}}. \tag{4.32}$$

The two terms can be interpreted as contributions to the self-energy from the screened exchange and from the Coulomb hole. An analytic result is obtained for the imaginary part of self-energy, since imaginary part of ϵ^{-1} is proportional to the δ-function. The real part of self-energy is obtained by one-dimensional integration numerically.

Hedin-Lundquist model neglects the contribution from electron-hole excitations. This leads to a small broadened tail in ϵ^{-1} below the plasmon frequency. This significantly affects only the imaginary part of self-energy below the plasmon frequency, but is important for the estimates of mean free path in LEED. It is less important for XAS, since the core-hole lifetime often dominates the effective mean free path, but sometimes can be noticeable (e.g. in EXAFS of Pb.[48]). These corrections were analyzed by Quinn [49] and are also used in our program (FEFF) to correct the Hedin-Lundqvist model.

Another simple way, suggested by Rehr, to give some weight of $\mathrm{Im}\,\epsilon^{-1}$ below the plasmon frequency is to use *finite* δ instead of infinitesimal. This is a reasonable thing to do, since experimentally $\mathrm{Im}\,\epsilon^{-1}$ always have a finite width of peaks. This *broadened plasmon approximation* is also implemented in FEFF7 code. Actually one can even fit the experimental $\mathrm{Im}\,\epsilon^{-1}$ with a number of Lorentzian curves, and still use just one dimensional integration to get the self-energy for use in Dyson equation.

For the magnetically ordered systems it is important to know the spin dependence of Σ, assuming we know local spin-up and down density. The screening is determined mainly by the Coulomb repulsion between electrons. Therefore we can neglect spin-dependence of $\mathrm{Im}\epsilon^{-1}$ and use 'two bubble' approximation for irreducible polarization propagator [25], used by Von Barth and Hedin in their calculation of spin-dependent

xc potential. Again $\mathrm{Im}\,\epsilon^{-1}$ can be taken in the single plasmon approximation. It will be spin independent, but can depend on spin polarization of the system $x = abs((\rho\uparrow - \rho\downarrow)/\rho_{tot})$. The plasmon frequency dependence on the spin polarization is expected to be small. First, $q = 0$ limit is determined just by the total density and therefore is x-independent. Also the large q limit is fixed by the electron mass. Thus only the second coefficient in plasmon dispersion relation will be x-dependent, but it has small effect on the calculated self-energy (HL review [19] p.85). Therefore one can take ϵ^{-1} just from the total density. Formally spin dependent Σ looks the same as in unpolarized case, but the spin dependence of self-energy will come just from the difference in integration range, since the spin-up density is not equal to the spin-down density:

$$\Sigma_{HL}(\omega, \vec{k}, s) = -\frac{1}{(2\pi)^3}\int dq \frac{v_{\vec{q}} n_{\vec{k}+\vec{q},s}}{\epsilon(q, \epsilon_{\vec{k}+\vec{q},s} - \omega)} - \frac{\omega_p^2}{(2\pi)^3}\int \frac{v(q)}{2\omega_p(q)} \frac{dq}{w_p(q) + \omega - \epsilon_{\vec{k}+\vec{q},s}} \quad , \tag{4.33}$$

where s stand for spin-up or -down.

To conclude the discussion of uniform electron gas I would like to mention that improvements over the RPA results for uniform electron gas did not come from the next terms in perturbation expansion for Green's function. One way of improvements was suggested by Singwi et al.[50] They did more careful consideration of the exchange-correlation hole in terms of pair distribution function and obtained 3 equations for the dielectric function, the Hubbard factor $G(q)$ [51] and the static structure factor (Fourier transform of the pair distribution function), which can be solved self-consistently. The other approach, used by Ceperley and Alder [52] to derive the most popular LDA exchange-correlation potential, also considers correlations between electrons more carefully. They used many-body form of the wave function – usual Slater determinant modified by a Jastrow factor. One has to do the Monte-Carlo calculations in the parameter space. However, this second approach is much easier to generalize for the real systems, and calculations for a number of materials have been done.[53]

4.2.2 Application of GW to real materials

The usual way of using GW was described above. The result is a shift of energy levels due to the real part of self-energy, and a finite mean free path of photoelectron

due to the imaginary part of self-energy. However the last step of calculation for nonuniform system is the most difficult. This complication can be overcome using HL result for the uniform electron gas. The LDA approach to calculate self-energy has been suggested by Sham and Kohn. [40] One approximates the nonlocal Σ by it's value for the uniform electron gas with the same density.

$$\Sigma(r, r', E) = \Sigma_{HL}(\rho(r), E)\,\delta(r - r') \quad . \tag{4.34}$$

Since the value of Σ at Fermi level gives ground state exchange-correlation, one wants to enforce the best known LDA ground state potential (Ceperley-Alder[52] and may be generalized gradient corrections of Perdew[54])

$$\Sigma(r, E) = V_{LDA}(\rho(r), \nabla\rho(r)) + \Sigma_{HL}(\rho(r), E) - \Sigma_{HL}(\rho(r), E_F) \quad . \tag{4.35}$$

This type of approach, unlike the first one, cannot lead to the improvements in band structure over the LDA. The results for ground state will be essentially the LDA results. However, this is a reasonable approximation for the calculation of XAS and is used in our program FEFF, since it gives reasonable value for the mean free path.

Actually a semi-empirical approach can be made following Penn,[27] if one is interested in the statistical average of $\mathrm{Im}\,\Sigma(\vec{k})$, which gives the mean free path:

$$\mathrm{Im}\,\bar{\Sigma}(\vec{k}) = \int d^3q \mathrm{Im}\,\frac{v_{\vec{q}} n_{\vec{k}-\vec{q}}}{\epsilon(q, E_{\vec{k}} - E_{\vec{k}-\vec{q}})} \quad . \tag{4.36}$$

The formula should be compared with Eq. 4.32. It assumes, that on average the screening is uniform and does not depend on the direction of vector $\vec{q}$. Under several assumptions Penn derived an approximate relation between $\epsilon(q, w)$ and $\mathrm{Im}\,\epsilon(0, w)$, where the last quantity can be obtained from optical absorption or calculated using the RPA. His final result is

$$\mathrm{Im}\,\epsilon^{-1}(q, \omega) = \int_0^\infty d\omega_p \frac{2}{\pi\omega_p}(-\mathrm{Im}\frac{1}{\epsilon(0, \omega)})(\mathrm{Im}\,\frac{1}{\epsilon_L(q, \omega, \omega_p)}) \quad , \tag{4.37}$$

where ϵ_L is Lindhard dielectric function. Penn also showed that the single pole approximation can be used for high energies (EXAFS region). Using this approach and experimental data for the noble metals Penn obtained a reasonable agreement for the energy dependent mean free path in these materials.

4.2.3 Core-valence separation

Another advantage of the GW is due to the natural separation of Σ into the core and valence contribution, first suggested by HL [19]

$$\Sigma = G_c v + G_v W^v P^c W^v + G^v W^v \quad , \tag{4.38}$$

where 3 terms are interpreted as the bare exchange (HF) potential from the core, the screened polarization potential from the core, and the self-energy from the valence electrons. Therefore, using known results for the self-energy of uniform electron gas, one can make LDA approximation for the self-energy:

$$\Sigma = \Sigma_{HF}(core) + \Sigma_{HL}(\rho_{val}(r)) \tag{4.39}$$

or

$$\Sigma = \Sigma_{HF}(core) - \Sigma_{HL}(\rho_c(r), E - k_f^2 + k_c^2) + \Sigma_{tot}(\rho_{tot}(r), E) \quad . \tag{4.40}$$

Both of these nonlocal GW approximations for the self-energy have been used to calculate absorption of Cu-metal, (see chapter 6) but the first one gave better numerical results.

For most elements of the periodic table it is clear, how to make the core-valence separation: s and p electrons with the largest principal quantum number are valence and the rest are core. Partially filled d- and f-electrons also are usually treated as valence,(as in pseudo-potential method). However, for the f-electrons crystal field theory (CFT) explains well their optical properties. CFT is based on assumption, that f-shell has an integer number of electrons, and its ground state is given by the Hund's rules. Therefore it treats f-electrons, as if they were core electrons. Agreement with experiment means, that simple band structure for f(d)-electrons does not work, and more careful treatment of the electron-electron interaction is needed. This can be achieved by adding the Hubbard term to LDA based calculations [55] (LDA+U model). This may be less important for the d-electrons, where the spin-polarized band structure calculations give reasonable estimates for the magnetic moments [56].

The atomic-like (localized) interpretation of partially occupied d and f shells, and consideration of the exchange interaction between two orbitals centered on the neighbors led to the Ising and Hamilton models of magnetism. The spins on each atom are assumed to be known, and they interact with each other by some known

law. For the f-electrons these local spins can be easily obtained from Hund's rules, and agree well with the experimental data.

Our main concern is the construction of spin-dependent potential for a given magnetic system. If the spins associated with each site are known (Hund's rules, band structure calculation or experiment), then the spin-dependent electron density can be obtained. The usual Mattheis prescription can be used to find the muffin tin radii from total density. The difference in spin-up and -down potential in terms of spin dependent density is given by Von Barth and Hedin.[25] Energy dependence of Σ is important for the photoelectron, and one has to use the spin dependent self-energy.

Since partially occupied d-electron wave function sticks out of the muffin tin sphere (much less for f-electrons), localized treatment of the d-electron is slightly complicated. Within our core-valence separation we have only exchange term in Σ from the d-electrons. Thus inside the muffin tin sphere one can use HF expression for nonlocal Σ_x. The local expression is preferred for the interstitial region, since we have to find the appropriate muffin tin zero. In the interstitial region potential varies smoothly, and the WKB approach can be conveniently used. The photoelectron wave function is a linear combination of exponents $\exp(i\vec{k}\vec{r})$. The exchange due to the ℓ-electrons gives

$$\Sigma_\ell(r,r',s)\exp(i\vec{k}\vec{r}\,') = \frac{e^2\,R_L^*(r,s)R_L(r',s)}{|r-r'|}\exp(i\vec{k}\vec{r}\,') = \Sigma_\ell(r,k,s)\exp(i\vec{k}\vec{r}) \quad . \tag{4.41}$$

Thus the local expression for Σ_ℓ is

$$\Sigma_\ell(r,k,s) = \frac{N_\ell}{2\ell+1}\int d^3r'\frac{e^2R_\ell(r,s)Y_L^*(\Omega')R_\ell(r',s)Y_L(\Omega)}{|r-r'|}\exp(i\vec{k}(\vec{r}\,'-\vec{r})) \quad . \tag{4.42}$$

Using the Fourier transform of Coulomb potential

$$\Sigma_\ell(r,k,s) = \frac{-4\pi e^2N_\ell}{(2\pi)^3(2\ell+1)}R_\ell(r)\int d^3r'd^3q\frac{Y_L^*(\Omega')R_\ell(r',s)Y_L(\Omega)}{|\vec{k}-\vec{q}|^2}\exp(i\vec{q}(\vec{r}\,'-\vec{r}))\int\frac{d\Omega}{4\pi}\,, \tag{4.43}$$

where the last integral represents the spherical averaging of $\Sigma_\ell(r,k,s)$. Expressing $\exp(i\vec{q}\,\vec{r}) = 4\pi\sum i^l j_l(qr)Y_L^*(\hat{q})Y_L(\Omega)$, after the angular integration we have

$$\Sigma_\ell(r,k,s) = \frac{-4\pi e^2N_\ell(s)}{(2\pi)^3}R_\ell(r)\int(r')^2dr'd^3qj_\ell(qr)\frac{R_\ell(r',s)j_\ell(qr')}{|\vec{k}-\vec{q}|^2} \quad . \tag{4.44}$$

Finally, the angular integration over $\hat{q}$ gives

$$\Sigma_\ell(r,k,s) = \frac{-e^2 N_\ell(s)}{\pi} R_\ell(r) \int_0^\infty dq j_\ell(qr) f(q) \frac{q}{k} \ln\left|\frac{k+q}{k-q}\right| \quad , \tag{4.45}$$

where the atomic form-factor is

$$f(q) = \int (r')^2 dr' R_\ell(r',s) j_\ell(qr') \quad . \tag{4.46}$$

The logarithmic divergence does not cause any numerical problems. The wave vector k, used for WKB wave function, will be r-dependent inside the muffin tin, according to $k^2(r)/2 = E - V(r)$. If one neglects this dependence, then expression is also valid inside the muffin tin sphere. Then the average over r will recover formula 11 of Horsch et al.[57]

$$\bar{\Sigma}_\ell(k,s) = -\frac{2\, N_\ell(s) e^2 n_{at}}{\pi} \int d^3q \frac{f^2(q)}{|\vec{k}-\vec{q}|^2} \quad , \tag{4.47}$$

where $n_a t = N/V$ is the density of atoms. Actually these authors got a good agreement with the experimental results for the real part of self-energy in Ag. May be one can neglect k(r) , since valence wave function is big only in the region where potential is shallow.

4.3 Many body effect on sum rules

Due to the core-hole, the final state orbitals differ from the initial ones. Therefore the question is, what properties of the system do we get from the sum rules? The ground state expectation values can differ significantly from those, calculated with the core-hole, as band structure calculations indicate [58]. Below I will show, that within sudden approximation the corrections to sum rules are somewhat opposite to the intuition. To the main order the initial state orbital should be corrected for the core-hole, and the final state orbitals should not. Therefore, extracted from the sum rules quantities (such as L_z) are proportional to the ground state expectation values of corresponding operators.

We start as usual from the Fermi's golden rule for the x-ray absorption coefficient within the second quantization formalism.

$$\mu(\omega) = \frac{2\pi}{\hbar} \sum_F \langle I| \sum_{j_2,f_2} d^*_{j_2,f_2} a^\dagger_{j_2} a_{f_2} |F\rangle\langle F| \sum_{j_1,f_1} d_{j_1,f_1} a^\dagger_{f_1} a_{j_1} |I\rangle \delta(\omega - E_F + E_I)\,, \tag{4.48}$$

where I,F are the initial and final many body states, which we assume to be the Slater determinants ($|I\rangle = a_N^\dagger \dots a_1^\dagger |0\rangle$, $|F\rangle = a'^\dagger_N \dots a'^\dagger_1 |0\rangle$); and $a_k, a_k^\dagger$ are destruction and creation operators for the state k. I will use unprimed operators for the ground state operators and primed for excited. Dipole matrix elements are taken in the initial state basis: $d_{jf} = \langle f|\vec{p}\cdot\hat{\epsilon}|j\rangle$. Notice that, if we were going to sum over all edges, there would be no many-body corrections to the f-sum rules. In that case, the set of final states is complete, and we will recover the single electron result. [59].

The problem is, how to express theoretically contribution to the integrated intensity from the j-edge. The best way, I can think of, is to require, that the final state should have a hole in n', j', m_j state. Therefore the integrated intensity for the j-edge is

$$\bar{\mu}_j = \frac{2\pi}{\hbar}\langle I| \sum_{j_2,f_2} d^*_{j_2,f_2} a^\dagger_{j_2} a_{f_2} \sum_{F_j} |F_j\rangle\langle F_j| \sum_{j_1,f_1} d_{j_1,f_1} a^\dagger_{f_1} a_{j_1} |I\rangle \quad , \tag{4.49}$$

where F_j belongs to the restricted set of wave functions with a hole in the j-orbital:

$$|F_j\rangle = a'_j |F_{N+1}\rangle \, . \tag{4.50}$$

I assume, that operator a'_j is constant, independent of further excitations. This approximation is reasonable, since the changes are expected to be less, if another hole is made in the same or more distant from the nucleus orbital.

With this ansatz we can go from the restricted sum in N-particle states to the sum over complete set of (N+1)-particle states. The other problem is that we will double count the transitions with holes in two orbitals $j1$ and $j2$. Therefore, the double counting for j_1 , j_2 is reasonable to subtract from the integrated j-edge absorption with the higher excitation energy. We will neglect this, since the appropriate energies lie in the region, where the separation of j_1 and j_2 signal is anyway ambiguous. We will estimate later the contribution from such possibility. Therefore we have

$$\bar{\mu}_j = \frac{2\pi}{\hbar}\langle I| \sum_{j_1,f_1} d^*_{j_2,f_2} a^\dagger_{j_2} a_{f_2} a'_j \sum_{F_{N+1}} |F_{N+1}\rangle\langle F_{N+1}| a'^\dagger_j \sum_{j_1,f_1} d_{j_1,f_1} a^\dagger_{f_1} a_{j_1} |I\rangle \, . \tag{4.51}$$

Now the sum over complete set can be replaced by unity and

$$\bar{\mu}_j = \frac{2\pi}{\hbar}\langle I| \sum_{j_2,f_2} d'^*_{j_2,f_2} a^\dagger_{j_2} a_{f_2} a'_j a'^\dagger_j \sum_{j_1,f_1} d_{j_1,f_1} a^\dagger_{f_1} a_{j_1} |I\rangle \quad . \tag{4.52}$$

Using mixed first and second quantization notations and expanding a'_j in the ground state basis, we obtain

$$\bar{\mu}_j = \frac{2\pi}{\hbar} \sum_{j,f,n} \langle j_1|p\cdot\epsilon^*|f_1\rangle\langle f_2|p\cdot\epsilon|j_2\rangle\langle n_2|j'\rangle\langle j'|n_1\rangle\langle I|a^\dagger_{j_2}a_{f_2}a_{n_2}a^\dagger_{n_1}a^\dagger_{f_1}a_{j_1}|I\rangle \quad . \quad (4.53)$$

The last part involving the second quantization operators is easy to calculate, using the commutation relations. If the system has inversion symmetry, then all states can be chosen to be even or odd. Since the dipole matrix elements are nonzero only for the opposite parity states, then $a^\dagger_j$ simply anticommute with $d_{j,f}a_f$. Therefore both j should be occupied and both f unoccupied. Orbitals n_1, n_2 can be j_1, j_2 or unoccupied.

$$\begin{aligned}&\langle I|a^\dagger_{j_2}a_{f_2}a_{n_2}a^\dagger_{n_1}a^\dagger_{f_1}a_{j_1}|I\rangle = \delta_{j,occ}\delta_{f,unocc}\times \\ &(\delta_{n1,j1}\delta_{n2,j2}\delta_{f1,f2} + \delta_{j1,j2}\delta_{n1,n2}\delta_{f1,f2}\delta_{n,unocc} - \delta_{j1,j2}\delta_{n1,f2}\delta_{f1,n2}) \quad . \quad (4.54)\end{aligned}$$

Substitution of this result immediately gives that:

$$\begin{aligned}\bar{\mu}_j = \frac{2\pi}{\hbar} \sum_{j-occ} \sum_{f,n-unocc} &(\langle j_1|p\cdot\epsilon^*|f\rangle\langle f|p\cdot\epsilon|j_2\rangle\langle j_2|j'\rangle\langle j'|j_1\rangle \quad (4.55)\\ +\langle j|p\cdot\epsilon^*|f\rangle\langle f|p\cdot\epsilon|j\rangle\langle n|j'\rangle\langle j'|n\rangle &- \langle j|p\cdot\epsilon^*|f_1\rangle\langle f_2|p\cdot\epsilon|j\rangle\langle f_1|j'\rangle\langle j'|f_2\rangle)\,.\end{aligned}$$

This can be rewritten in a more compact form, using the following notations

$$\begin{aligned}|j"\rangle &= \sum_{n-occ} |n\rangle\langle n|j'\rangle \\ \alpha_j^2 &= 1 - \langle j"|j"\rangle \\ |j^-\rangle &= \alpha_j^{-1}(|j'\rangle - |j"\rangle) \\ \bar{\mu} &= \sum_{j-occ} \bar{\mu}_j \quad . \end{aligned} \quad (4.56)$$

Then the integrated j-edge absorption is

$$\begin{aligned}\bar{\mu}_j = \frac{2\pi}{\hbar} \quad &(\sum_{f-unocc} \langle j"|p\cdot\epsilon^*|f\rangle\langle f|p\cdot\epsilon|j"\rangle \\ + \quad &\alpha_j^2(\bar{\mu} - \sum_{j-occ} \langle j|p\cdot\epsilon^*|j^-\rangle\langle j^-|p\cdot\epsilon|j\rangle)) \quad . \end{aligned} \quad (4.57)$$

In order to estimate the error coming from the double counting, which is the limit of best experimental uncertainty in the separation of different j-edges, we have to

Table 4.1: Overlap integrals between the core-hole initial orbital and the orbital with principal quantum number n, calculated with core-hole, for selected elements and edges.

$n=$	$Fe, L3$	$Ga, L2$	$Gd, L3$	$Gd, M4$
2	+0.99982	+0.99988	0.99997	
3	−0.01264	−0.01032	0.00576	0.99993
4		+0.00149	0.00194	0.00843
5			0.00067	0.00148

estimate the term

$$\frac{2\pi}{\hbar}\langle I|\sum_{j_2,f_2} d'^{*}_{j_2,f_2} a^{\dagger}_{j_2} a_{f_2} a'_{j_1} a'_{j_2} a'^{\dagger}_{j_2} a'^{\dagger}_{j_1} \sum_{j_1,f_1} d_{j_1,f_1} a^{\dagger}_{f_1} a_{j_1} |I\rangle \quad . \tag{4.58}$$

This term was obtained in the same manner as equation 4.53. Certainly, it is of the second order in parameters α_j, since one of the $a'^{\dagger}_{j_2} a'^{\dagger}_{j_1}$ should belong to the unoccupied states as well as one of the $a'_{j_2} a'_{j_1}$.

Therefore one can consistently neglect the second order terms. The first order corrections can come only from the first term in equation 4.57. Finally,

$$\bar{\mu}_j = \frac{2\pi}{\hbar} \sum_{f-unocc} \langle j"|p\cdot\epsilon^*|f\rangle\langle f|p\cdot\epsilon|j"\rangle + O(\alpha_j^2)\,. \tag{4.59}$$

To see the typical values of α_j, I made calculation of overlap integrals. I used the Dirac-Fock-Slater atomic code, which is a part of the code FEFF6. I made calculations for the L3 edge of several elements, and the results are presented in table 4.1. It is clear from the table, that $\alpha_j^2 \approx 10^{-4}$ is really a small parameter. Thus all second order corrections can be omitted.

Thus the main order many-body corrections are accounted for by the simple substitution $j" \to j$ for the initial state. Final states should be calculated without core-hole.

The last expression is the same as the starting point in the derivation of sum rules within the independent electron approximation [35], except simple substitution for the initial state. Therefore the sum rules remain valid, and they give ground state properties.

Notice, that I managed to avoid the excitation spectrum problem, using the completeness relation. Thus the excitation spectrum, which complicates the calculation of the energy dependent absorption $\mu_j(\omega)$, actually does not enter into discussion of the integrated intensities $\bar{\mu}_j$.

Usually XMCD signal goes fast to zero from the edge. Therefore the finite integration range is all, one wants to use. However, the wrong choice of normalization can lead to large errors. In the normalization, suggested by Wu et al. [34], one takes the integration range equal to the appropriate band width. This method is expected to work best, if there is a strong white line in the absorption. Wu et al. [34] had 5-10% error for Fe. In other materials the error was larger - 30-50% [31]. As previous analysis shows, such error cannot come from the independent electron approximation. The normalization factor should be better defined. Atomic calculations should be involved in the determination of normalization factor, or it should be found experimentally from the known material. The proportionality itself can be enough, for example, to investigate the temperature dependence of average magnetic moments. The normalization factor can be determined also if the value of the operator is known for some temperature.

To summarize:

- The sum rules, derived with infinite integration range, can give ground state quantities with 1% precision. However, infinite integration range is impractical, and not necessary, since all quantities will converge in a small range, except the normalization.

- Finite integration range, defined by the band width, leads to errors of order 10%, which is also a typical difference between final and initial state expectation values.

- Intermediate approach combines the convenience of finite range integration and the precision of infinite range sum rules. Stop integration of XMCD or XLD signal at any convenient extremum, and find the normalization from other data (calculations, low T limit, other known material, etc.).

4.4 Beyond sudden approximation

The steps beyond sudden approximation is an important topic of active research. Within the sudden approximation discussed above, the incoming photon creates a photoelectron , which couples to plasmons, and a core-hole, which couples to photons (radiative decay dominates). So the coupling between photoelectron and core-hole is neglected. However, the core-hole also has a charge (+e), and the coupling of core-hole to the plasmons should be included in the theory. Then the theory is no longer separable, however it is still possible to handle.

The coupling of core-hole to plasmon is expected to be especially important in XANES region. First, photoelectron in this region has smaller velocity. Second, such coupling led Mahan to the theory of edge singularities in the ladder approximation. Experimentally, singularities become rather edge corrections to the single electron theory results, due to the finite core-hole lifetime. Third, an important cancelation theorem of extrinsic and intrinsic losses at the plasmon frequency has been proven by Hedin[60], and the numerical results show that Im part of self-energy is significantly decreased in a wide range of energies.[61]

In the XAS calculations of Cu with sudden approximation, we always find that the Im part of self-energy is to big (by 2 eV out of 5) up to 150 eV above the edge. This can be due to the interference effects.[24] On the other hand, Penn's calculations of the mean free path have a good agreement with experiment, but he used experimental optical absorption. The *ab initio* GW calculations of optical absorption have been done by Gunnarsson et al.[62], and show a reasonable agreement with experiment. Therefore, improved GW calculation of the self-energy can help to asses the importance of interference effects. In any case, it seems that they can be treated by the perturbation series in the screened Coulomb interaction.

Chapter 5

FEFF7

All details, how to use the FEFF7 code, can be found in it's documentation and from the comments in the source code. This chapter is designed for the FEFF expert users, who want a deeper understanding of the physics put in the FEFF7, to use our code more efficiently, and may be even to make his own modifications to the code. If you are not a FEFF user, you can skip this chapter and look at the results, which I obtained using FEFF7 in the following chapters.

5.1 Input and output.

There is one input file for the code – feff.inp. It consists of the entries, named cards. Each card has a name and can have additional arguments. All cards are classified and described in the FEFF7 document. Therefore, I do not reproduce here a long description of all input cards. If you are reading this chapter, you should be already a FEFF user.

There are two main possibilities available to run the code. The basic one is when XAS is calculated for a cluster of N atoms, specified by the ATOMS card (a list of Cartesian coordinates and atomic numbers). A second method can be used when very little is known about the structure of material. In this case, the approximate coordination for each type of atom can be specified with the OVERLAP card. Only single scattering paths can be used in this case to calculate XAS (see SS card). However, even in this case improved average distances and coordination numbers can be obtained.

Output of FEFF7 is designed to be used by a number of fitting programs, based on the standard EXAFS formula 2.58. Thus feffnnnn.dat files are used by the FEFFIT program, and chipnnnn.dat files by the EXAFSPAK [63] and XFIT [64]. The total calculated absorption coefficient is written in the file xmu.dat, and can be directly compared with experimental data.

The entire code (feff.f) can be divided into five steps.

- rdinp(0-th step) – Reads the input file feff.inp

- potph(1-st step) – Solves the atomic problem for each type of free atom (scfdat), uses the Mattheis prescription to construct the ground state muffin tin potential (istprm) based on the overlapped atomic charge densities (ovrlp). Solves the Dirac-Fock equation for photoelectron (dfovrg, fovrg) with the energy-dependent self-energy (xcpot), which is also known as the Dyson equation. The resulting embedded atom cross-section (xsect) and partial wave phase shifts (phase) passed to the next units.

- paths(2-nd step) – Constructs a list of important paths (paths.dat) using hash and keep sort, based on the calculated partial wave phase shifts. Various paths filters have been designed by S. Zabinsky, to produce a reasonable list even for the materials with a large mean free path. The CRITERIA and PCRITERIA cards can be essential to get a reasonable paths list. Different paths can give the same contribution due to the symmetries of the problem. This is used by subroutine pathsd to further reduce the amount of calculation.

- genfmt(3-rd step) – For every path in the list calculates it's contribution to XAS, using fast Rehr-Albers algorithm. For a long list of paths this part takes the most of calculational time. All results are written in the file feff.bin.

- ff2chi(4-th step) – This part usually takes the least amount of time and can be repeated quickly in the analysis. It combines the contributions from all paths into a total cross-section. The calculated XAS and EXAFS are written into files xmu.dat and chi.dat. At request (see PRINT card) additional files feffNNNN.dat and/or chipNNNN.dat are written for the use in EXAFS analysis programs (FEFFIT, etc.).

According to the five steps of the program, there are 5 levels of input cards.

Level 0. You can run the code for known and unknown structures, depending on whether you use ATOMS or OVERLAP cards. POTENTIALS card is also necessary to run the code. Several cards have the same importance for all steps: CONTROL, PRINT, TITLE, END.

The rest of the cards can be conveniently classified by by the step, which they affect first.

Level 1. AFOLP, EXCHANGE, FOLP, HOLE, ION, JUMPRM, NEMAX, NOHOLE, RGRID, RMULT, RPHASES, XANES.

Level 2. CRITERIA (plane wave), NLEG (only 2 for OVERLAP mode), NOGEOM (unimportant for OVERLAP mode), PCRITERIA, RMAX, SS.

Level 3. CRITERIA (curved wave), IORDER. Three cards, which cannot be used in OVERLAP mode: ELLIPTICITY, NSTAR and POLARIZATION.

Level 4. CORRECTIONS, CUSTOMCRITERIA, DEBYE, MBCONV, SIG2, SIG3.

The initial step (rdinp) is always called, but the rest are called only if the appropriate CONTROL card is specified. Since some changes in the input file do not require to run the whole code again, you can save computational time by the proper use of the CONTROL card. If you change just one card, you may want to avoid the repetition of long calculations (steps 1,3) or to use the same paths list (omit step 2). For some diagnostic purposes you may omit any step.

If you changed just one of the following cards, you may skip the following steps: AFOLP – 2; CORRECTIONS – 1, 2, 3; CRITERIA – 1 (3 and 4, if you are making paths list); CUSTOMCRITERIA–1, 2, 3; DEBYE – 1, 2, 3; ELLIPTICITY – 1,(sometimes 2); EXCHANGE – 2; FOLP – 2; HOLE – 2; ION – 2; IORDER – 1, 2; JUMPRM – 2; MBCONV – 1, 2, 3; NEMAX – 2; NLEG – 1; NOGEOM – 1; NOHOLE – 2; NSTAR – 1, 2, 4; PCRITERIA – 1 (3 and 4, if you are making paths list); POLARIZATION – 1; POTENTIALS – 2; PRINT – 1, 2, 3, 4; RGRID – 2; RMAX – 1; RPHASES – 2; SIG2 – 1, 2, 3; SIG3 – 1, 2, 3; SS – 1; TITLE – 1, 2, 3, 4; XANES – 2.

5.2 Description of FEFF7 subroutines

It is very convenient to look at the calling sequence of the program arranged in the hierarchy table 5.1. With a short description of subroutines below, it helps to understand the structure of the huge FEFF code, and find a place for alterations.

Below I give a brief description of each subroutine. It is arranged in alphabetical order for each step separately.

Table 5.1: Calling sequence of FEFF7

0	cright feffbd chopen str.f wlog						prcrit	rphbin cpl0	
							paths	rdhead sortix	
	rdinp	mkptz dist						ccrit	mrb mcrith mcritk
		setgam	terp					ipack heap sdist	
1 s t e p	potph	rpotph SCFDAT					pathsd	ipack*	
		ovrlp	sumax frnrm					timrep	mpprmp phash
		istprm	sidx					sortix*	
			istval	xx.f				outcrt	mrb* strap mcrith* mcritk*
			fermi logint.f					mpprmd	
		head.f wpot phmesh fixvar fixdsx fixdsp				3 s t e p	genfmt	rphbin rdhead snlm rdpath setlam rot3i mmtr sclmz mmtrxi fmtrxi trap pijump getxk	
		xsect	setkap somm						
			xcpot	rhl rhlbp edp					
				imhl	cubic quinn ffq				
			DFOVRG						
			exjlnl	bjnser					
			csomm			4 s t e p	ff2chi	rdhead*	
		phase	besjn	bjnser				feffdt	
			xcpot* DFOVRG*					sigms	dist pertab
			fovrg	diff				pijump*	
		wphase getxk						terp	xx.f
								custom	trap*
								exconv conv	

Step 0.

CHOPEN Checks the status of opened file. This subroutine is used a lot throughout the program. It is practically always called, when a new file is opened.

CRIGHT Contains the Copyright information.

DIST Calculates the distance between atoms.

FEFFBD Contains an important version information.

MKPTZ Makes polarization tensor, if POLARIZATION and optional ELLIPTICITY are specified.

RDINP Reads the input file feff.inp.

SETGAM Sets the core-hole lifetime parameter Γ, using the tabulated experimental data.

STR.F Contains several subroutines (BWORDS, ISTRLN, TRIML, UPPER, LOWER), written by S. Zabinsky, to simplify the work with string variables in FORTRAN. They are used a lot by a subroutine RDINP. Due to these subroutines a lot of freedom on the format of input file has been achieved.

TERP Linear interpolation subroutine. It is used a lot throughout the code. There are some modifications of this double precision subroutine to handle single precision numbers (TERP1), complex numbers (TERPC) and two dimensions (TERP2D).

WLOG Writes the same information on the screen and into the log.dat file. This is convenient for the diagnostic purposes, if you want to look at the screen output later.

Step 1.

BESJN Calculates the spherical Bessel functions j_ℓ and n_ℓ. Recursion relations for the large argument are used.

BJNSER Calculates the spherical Bessel functions j_ℓ and n_ℓ for a small argument, using the series expansion.

CSOMM Integration by the Simpson method of a complex function on a double precision grid. SOMM does the same for a double precision function.

CUBIC Finds the roots of a cubic equation.

DIFF Just a part of FOVRG, dealing with a finite difference method.

DFOVRG Solves the Dyson (Dirac-Fock plus self-energy) equation for photoelectron. The main output are the large and small components of photoelectron wave function at the muffin-tin radius. This is a fully relativistic counterpart of subroutine FOVRG.

EDP Calculates the energy dependent Dirac-Hara self-energy.

EXJLNL Uses the exact analytic expressions for the Bessel functions with $\ell \leq 5$ and large enough argument.

FERMI Calculates the Fermi level and the Fermi momentum for the system.

FFQ Analytic function, that gives imaginary part of the Hedin-Lundqvist self-energy in a single plasmon pole approximation.

FIXDSP Fixes up the Dirac spinor components of the initial state orbital (ihole) (dgc0 and dpc0) from the atomic code (SCFDAT) for the xsect and phase codes. It is called only, if the grid size is changed (RGRIG card).

FIXDSX Fixes up all Dirac spinor components (dgc and dpc) from the atomic code (SCFDAT) for the xsect and phase codes. It is called only, if the grid size is changed (RGRIG card).

FIXVAR Fixes up the charge density and the potential for xsect and phase codes. It is called only, if the grid size is changed (RGRIG card).

FOVRG Solves the Dyson equation for photoelectron. It is a non-relativistic analog of DFOVRG, but it can be used only for the negative κ and the LDA self-energy.

FRNRM Finds the Norman radius.

GETXK Function, which finds a wave vector k for the given energy.

HEAD.F Contains subroutines to set the header (STHEAD) and to write the header (WTHEAD).

IMHL Calculates the imaginary part of the Hedin-Lundqvist self-energy in a single plasmon pole approximation.

ISTPRM Finds all parameters of the muffin-tin potential.

ISTVAL This subroutine calculates the interstitial values of potential and density for the overlapped atom.

LOGINT.F Contains subroutines to calculate the local self-energy, using WKB approximation (see Eq. 4.45). These subroutines are called only, if the card EXCAHGE 7 is specified. It is experimental and is set for the Cu calculations only.

OVRLP Overlaps the Coulomb potentials and the electron densities for the current unique potential.

PHASE Calculates complex scattering phase shifts.

PHMESH Makes the energy mesh for PHASE.

POTPH Calculates the potentials and the phase shifts for the unique potentials, specified by ATOMS and OVERLAP cards.

QUINN Calculates contribution to the imaginary part of self-energy due to the electron-hole excitations, using a formula from the Quinn's review.[49]

RHL Calculates the real part of the Hedin-Lundqvist self-energy in a single plasmon pole approximation.

RHLBP Calculates real and imaginary parts of the Hedin-Lundqvist self-energy in a broadened plasmon pole approximation (see section 4.2.1).

RPOTPH Reads the input data for the POTPH.

SETKAP Sets the angular momentum and the quantum number κ for the core-hole orbital.

SCFDAT A single configuration Dirac-Fock atomic code [65]. Finds atomic orbitals and energies.

SOMM Integration by the Simpson method of a double precision function on a double precision grid. Subroutine CSOMM is for the complex function.

SIDX Finds the last non-zero point of overlapped density.

SUMAX Adds contribution from the atoms of type 2 to the overlapped density (potential) around atom of type 1.

WPHASE Writes the partial wave phase shifts into a file phase.bin.

WPOT Writes potentials to a file, named POTxx.DAT, for each unique potential, if an appropriate PRINT option is specified.

XCPOT Calculates the self-energy, using the model, specified by EXCHANGE card.

XSECT Calculates the embedded atom cross section, which is a smooth background of XAS.

XX.F Several functions (XX,RR,II) to work with the logarithmic Loucks grid.

Step 2.

CCRIT Finds, whether a given path passes the keep and the heap criteria, specified by the PCRITERIA card.

CPL0 Calculates the associated Legendre polynomials $p_{l0}(x)$ by recursion.

HEAP.F Contains heap subroutines to maintain a heap (array h) and an index array (array ih), used to keep the data associated with the heap elements.

IPACK.F Packing (IPACK) and unpacking (UPACK) subroutines for the path finder and the degeneracy checker. Packs and unpacks the path's data.

MCRITH Decides, if we want the path to be added to the heap. Gives path parameters for the crit calculations (ri, beta and rpath).

MCRITK Decides, if we want to keep the path. We may want path in the heap so that other paths, built from this path will be considered, but do not want this path to be written out for itself.

MPPRMD Makes the path parameters, i.e. ri, beta and eta, for each leg for a given path.

MPPRMP Makes the path parameters (xp, yp and zp - coordinates in standard frame of reference) for each atom in a given path.

MRB Makes the path parameters (ri, beta and rpath) for the CCRIT calculations.

OUTCRT Makes a plane wave importance factor (see CRITERIA card) for the pathsd. Also it recalculates pathfinder criteria for the output.

PATHS Finds multiple scattering paths, which pass keep and heap criteria.

PATHSD Checks the path degeneracy and the plane wave criterion.

PHASH Hashes the path information into a double precision real number.

PRCRIT Prepares arrays, etc. for the pathfinder.

RDHEAD Reads title lines from the input file. Makes a header.

RPHBIN Reads the input data from phase.bin for the step 2.

SDIST Finds the distance between two Cartesian points. Single precision.

SORTIX.F Several subroutines (SORTII, SORTIR, SORTID) to make the heap sort by rearranging Indices, Real or Double precision numbers.

STRAP Single precision version of the trapezoidal integration (subroutine TRAP).

TIMREP Returns a path in the standard order and its hash key for sorting.

Step 3.

FMTRXI Calculates the scattering matrices $F(\lambda, \lambda')$. See Rehr-Albers paper [21].

GENFMT Calculates the contribution from each path into the total EXAFS signal, using Rehr-Albers algorithm. [21]

MMTR Calculates the energy independent part of the termination matrix M.

MMTRXI Calculates the termination matrix M for each energy point.

PIJUMP Removes the 2π jumps in phase shifts to make δ_ℓ continuous.

RDPATH Reads the current path data.

ROT3I Calculates the rotation matrix elements.

SCLMZ Sets the CLM(Z) for a current leg and for the current energy. See Eq. B11 in Rehr-Albers paper.[21]

SETLAM Sets the lambda array, based on the IORDER card and current energy.

SNLM Calculates the Legendre normalization factors $xnlm = \sqrt{(2l+1)(l-m)!/(l+m)!}$.

TRAP Integrates, using a trapezoidal rule.

Step 4.

CONV Convolutes the spectrum with Lorentzian of a constant width.

CUSTOM Does custom filtering for ff2chi, according to the CUSTOMCRITERIA card.

EXCONV Convolutes with the atomic model of excitation spectrum, if the MBCONV card is specified.

FEFFDT Writes feffNNNN.dat files.

FF2CHI Makes the final calculation of absorption coefficient and writes the output files for EXAFS analysis.

PERTAB Atomic weights and symbols from the periodic table.

SIGMS Calculates the Debye-Waller factors for each multiple scattering path, using the correlated Debye model.

5.3 SCFDAT and DFOVRG subroutines

The calling sequences of SCFDAT and DFOVRG subroutines are not shown in Table 5.1. These subroutines have a similar structure, since they both solve the Dirac-Fock equation. SCFDAT [65] is the atomic single configuration code, which requires only an atomic number as input and gives the atomic orbitals, densities and energies

Table 5.2: Calling sequences of SCFDAT and DFOVRG

SCFDAT			DFOVRG		
inmuat	getorb		inmuac	getorb	
wfirdf	nucdev dentfa soldir* messer*		wfirdc	nucdec solout*	
			potdvp		
muatco	cwig3j		muatcc	cwig3j	
ortdat	dsordf*		ortdac	dsordc	aprdec
lagdat	akeato		potex	aprdec	
	fdrirk	yzkrdf* dsordf		yzkrdc	aprdec yzktec
potrdf	akeato* aprdev		solout	intout	
			ortdac* cofcoc		
	yzkrdf	aprdev yzkteg			
soldir	intdir				
cofcon					
dsordf	aprdev				
messer					
tabrat	dsordf*				
etotal	akeato fdrirk* bkmrdf fdmocc				
potslw s02at					

in the output. DFOVRG is a modification of SCFDAT to solve Dyson equation only for the photoelectron with a complex (optical) potential in order to obtain complex partial wave phase shifts. The calling sequences for both of them are presented in Table 5.2.

The brief description of subroutines is given below, but also can be found in the original Desclaux paper [66].

AKEATO Finds in a table the angular coefficients to multiply the direct (F_k) and the exchange (G_k) integrals for two specified orbitals.

APRDEV Finds the coefficients of polynomial, which is a product of two polynomials, whose coefficients are given. APRDEC is a generalization, when the coefficients of one polynomial are complex.

BKMRDF Calculates angular coefficients for the Breit term.

COFCON Controls the acceleration of convergence in the iterative process. A generalization for the complex wave function, COFCOC, is currently switched off, and the maximum convergence "speed" is used.

CWIG3J Calculates the Wigner 3j symbols.

DENTFA Uses the Thomas-Fermi approximation for the charge distribution to start a self-consistent process.

DSORDF Calculates different integrals, using the Simpson method. Generalization to the complex functions is DSORDC.

ETOTAL Calculates the total atomic energy.

FDMOCC Multiplies the occupation numbers of two orbitals and excludes the self interaction for calculation of the total energy.

FDRIRK Calculates the radial integrals R_k (F_k and G_k in particular).

INMUAT Initializes the data and arrays for SCFDAT, using the atomic number.

INMUAC Initializes the data and arrays for DFOVRG, using the atomic number.

INTDIR Solves the inhomogeneous Dirac equation, using a 5-point predictor-corrector method. Uses outward integration to the left from the matching point, and inward to the right.

INTOUT The same for the photoelectron wave function and complex potential. Only the outward integration is needed.

LAGDAT Calculates the non-diagonal Lagrange multipliers.

MESSER Writes the message about an error.

MUATCO Makes a table of angular coefficients to multiply the direct (F_k) and exchange the (G_k) integrals. This table is used later by the subroutine AKEATO.

MUATCC The same as above, but for DFOVRG one of the orbitals should be occupied by a photoelectron. Table is simpler and does not require additional subroutines to use it.

NUCDEV Constructs the nuclear potential. Point charge is usually used, but finite nuclear size options are available. NUCDEC differs only by dimensions of the arrays.

ORTDAT Orthogonalizes orbitals, using the Schmidt procedure.

ORTDAC Orthogonalizes the photoelectron orbital, keeps the rest of orbitals frozen.

POTRDF Calculates the Coulomb and exchange potentials.

POTDVP Part of POTRDF to calculate the potential development coefficients (power expansion at the origin). This subroutine is called just once in DFOVRG.

POTEX Calculates exchange term for the photoelectron.

POTSLW Calculates the Coulomb potential only. This subroutine is borrowed from the previous atomic code (Dirac-Fock-Slater).

SOLDIR Calls INTDIR several times, trying to match the outward and inward integration by adjusting the diagonal Lagrange multiplier (one electron energy).

SOLOUT No matching is needed for the photoelectron, therefore calls INTOUT just once. The photoelectron energy is also fixed.

S02AT Several subroutines to make an estimate of S_0^2 from the atomic calculations.

TABRAT Prints out some additional results. See the PRINT card.

WFIRDF Calculates the initial orbitals from the Thomas-Fermi approximation for electron charge density. Solves the homogeneous Dirac equation.

WFIRDC Calculates the initial photoelectron orbital, using the LDA exchange-correlation potential. This will be the final result, unless a nonlocal self-energy model is specified.

YZKRDF Prepares to calculate the functions Y_k and Z_k from the Grant's review[22]. YZKRDC is for the complex functions and one of the orbitals is photoelectron's.

YZKTEG Calculates functions Y_k and Z_k, using a 4-point method. YZKTEC is for the complex functions. Otherwise, it differs only by dimensions of the arrays.

5.4 Theory left out in FEFF7

All the new theory, used in FEFF7, is discussed in three previous chapters. Our goal is to make the best possible code for XAS calculation. But, as usual, one must start with the simplest theories and add successive complications later. The following can be done to improve the existing code:

- Single electron theory. 1) The muffin-tin potential is not self-consistent. The Mattheis prescription of overlapped atomic densities is now used. Non muffin tin corrections to the potential also can be important in XANES. 2) For small clusters, the outer sphere corrections may be needed, which can be important in XANES. 3) The code is not fully relativistic yet. 4) Importance of the quadrupole and the magnetic dipole transitions in XANES should be estimated numerically. 5) Molecular dynamics (MD) has to be included to get the Debye-Waller factors for the paths. This can lead to an improved EXAFS analysis, but all existing *ab initio* MD codes are too slow to be a part of the XAS code. 6) The full multiple scattering is not yet done. It may improve XANES, but contradicts the spirit of EXAFS analysis, based on path expansion.

- Many body theory. 1) Self-energy. All realistic models of self-energy use Hedin-Lundqvist results, obtained within the GW approximation for uniform electron gas using single plasmon pole approximation. A better self-energy could be possibly obtained by applying GW for the real system under consideration. Calculated or experimental inverse dielectric function could be used. 2) Dynamical screening of core-hole is not considered. Interference effects can be responsible for overestimating losses by FEFF and "edge singularities" of Mahan. We use the "fully relaxed" approximation to calculate the potential for photoelectron, however this relaxation (i.e. screening) could be not complete. Obvious examples are semiconductors, isolators and small clusters. 3) Calculation of the realistic excitation spectrum is still difficult, but possible in principle. May improve the XANES and the reliability of coordination number determination. The experimentally observed excitation spectrum in the XPS is a combination of intrinsic (excitation spectrum) and extrinsic (plasmon and electron-hole pair production) losses, which are hard to separate.

- Spin complications. 1) The spin-dependent muffin-tin potential also has to be calculated self-consistently. 2) The spin dependent self-energy models used are *ad hoc*, and all are based on the ground state results of von Barth and Hedin for uniform electron gas. Spin dependent self-energy should be calculated in the single plasmon pole approximation from Eq. 4.33 or using the GW for self-consistent potential.

Thus, as one can see there are many problems to work on by the FEFF group. They differ in their complexity and region of importance (XANES or EXAFS; material type: metal, insulator,small cluster,etc.). Theoretical groups around the world chose different priorities in development of their codes. Other codes for XAS calculations may use the theory, that is not included into FEFF7. Many groups use the full MS, the outer sphere correction and the self-consistent potential are sometimes included.[67] However, none of them use the fast Rehr-Albers algorithm for the MS with curved wave corrections, and the self-energy models are less elaborate. Dipole transitions $\ell \to \ell - 1$ are not always included, and I will show examples, where they were found to be important. The relativistic dipole matrix elements are essential for $\ell = 0$ edges, and are implemented in FEFF7. Our code was aimed primarily for the use

with EXAFS analysis, where FEFF is the recognized leader,[68] but for XANES calculations some codes occasionally can do better job since they included additional important physics, missing in FEFF. Actually, the comparison of different codes and experiment can help to see the important missing details in every code. If we put the same theory into all the codes, we should have the same results. There are always bugs around, and everybody wants to get rid of them.

5.5 Spin-dependent modification FEFF7s.

There is just one card added into feff.inp file: SPIN ispin. The values of 'ispin' correspond to:

- SPIN –2. Calculate the spin-down SPXAS.
- SPIN 2. Calculate the spin-up SPXAS.
- SPIN –1. Make the spin-down portion of XMCD calculations
- SPIN 1. Make the spin-up portion of XMCD calculations. To get XMCD signal you have to combine data from two xmu.dat files. A simple program to do this that can be obtained from me (spin.f), or written by yourself.

Calculations are done, using the formulas from Chapter 3. Just two new subroutines have been added:
VBH - calculates the spin-dependent potentials based on the spin-dependent densities, using von Barth-Hedin results for the uniform electron gas.[25];
BCOEF - tabulates appropriate for XMCD or SPXAS coefficients, which are just some combination of the Wigner 3j-symbols.

Several subroutines were modified :
SCFDAT - now also gives atomic density magnetization (density-up minus density-down), which currently requires some care from the user. It has to be changed for every new element, but usually it is clear from the Hund's rule, how to construct density magnetization, and this process may be automated later.
OVRLP - overlaps atomic densities and construct the total density magnetization, relative to the central atom. Here the SPIN card is used to define the sign of central

atom density magnetization. This subroutine also requires user's attention, since here the procedure is different for ferromagnets and antiferromagnets. Now, there are examples for both, however in the later versions the relative spin orientation should be specified in feff.inp (add 5-th column in ATOMS card). Currently it does not overlap magnetization, thus in interstitial region it is zero. It should be fine for antiferromagnets and f-element ferromagnets, but can lead to important corrections for d-element ferromagnets.

ISTPRM - constructs the ground state potential, using the von Barth-Hedin prescription and the density magnetization from OVRLP. Finds (currently spin-independent) interstitial parameters.

XCPOT - constructs the spin-dependent self-energy, using different prescriptions, described in the text.

XSECT - calculates the embedded atom absorption for the spin-up and -down, according to the sign of 'ispin'.

PHASE - calculates the phase shifts for the constructed (by ISTPRM) potential, using the self-energy from XCPOT.

MMTR - calculates the energy independent part of termination matrix M in Rehr-Albers formalism. Coefficients, appropriate for XMCD of SPXAS, are calculated here.

MMTRXI -calculates the termination matrix M, using the coefficients from MMTR.

Once again, we use the rough prescription to construct the spin-dependent muffin-tin potential. It should be fine for the EXAFS were the small details of potential are irrelevant, but can be not good enough in the XANES region, where the self-consistent spin-dependent muffin-tin potential can lead to better results.

In order to use this spin dependent program you have to: 1) Check the construction of atomic density magnetization in the subroutine SCFDAT (examples for Mn, Fe, Gd are there); 2) Check the construction of spin-dependent potential by OVRLP (examples for ferromagnets and antiferromagnets are there). 3) Be especially careful for the antiferromagnets, since you may want to use the parity of iph to specify the relative directions of spin. 4) Now you can simply use the SPIN card to calculate SPXAS and XMCD. An additional simple program (spin.f) is needed to take care of the different normalizations and give the finite results. If this experimental version will work, then later versions of FEFF will be automated to work with SPIN card

and the 5-th column of ATOMS to specify the relative spin directions on atoms.

Chapter 6

STANDARD TEST ON CU-METAL.

Traditionally we test the XAS code on the Cu-metal. Historically, it was an example, where the single scattering theory failed, but the MS theory worked. Also the curved wave corrections were shown on the Cu example in the Rehr-Albers paper.[21] Since we are interested in the applications of our code to the structural EXAFS analysis, it is important to show that we have a good precision for the well known materials. The Cu-metal structure is well known from the X-ray scattering. Its XAS spectrum is accurately recorded at 10°K. Newville showed, that the Debye-Waller factors for Cu are well described by the correlated Debye model. [69] Therefore, I use our standard test on Cu to compare the self-energy models (XANES calculations and the precision in distance determination), and to analyze the applicability of the *ab initio* atomic model for determination of the coordination numbers.

6.1 Comparison of the self-energy models.

The FEFF7 provides a user with several options for the self-energy calculations. A brief description of the models, based on the theory of previous chapters, is given below.

1) **HL**. This model is based on the Hedin-Lundqvist single plasmon approximation. This is a standard model of the FEFF code.

2) **DH**. The Dirac-Hara self-energy takes into account only the exchange interaction for the uniform electron gas. The imaginary part is taken from the HL model.

3) **NL**. The nonlocal model is based on formula 4.39. This model uses the Dirac-Fock exchange for the core and the HL self-energy for the valence electrons. The 3d and 4s electrons of Cu are treated as valence and the rest as core. The phase shifts calculations with the NL model take almost 5 times longer, since several iterations for the photoelectron wave function should be made.

4) **SD**. Formally the same model as NL, but 3d electrons are included into the core. The desire to treat the d-electrons as localized (core) is determined by the localized

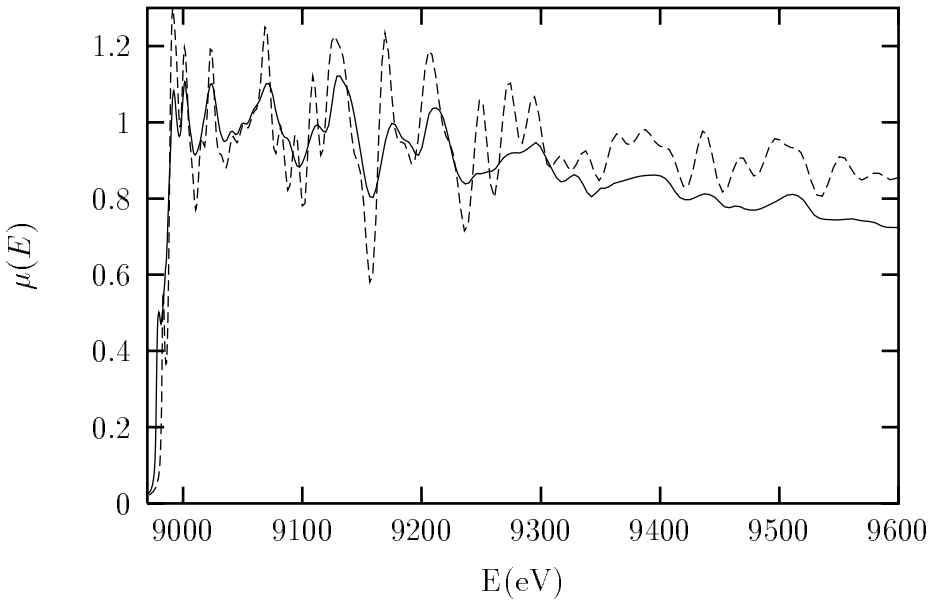

Figure 6.1: The calculated (dashes) XAS for Cu with a ground state potential (EXCHANGE 2 card was used in the feff.inp file) vs. experiment(solid). The calculated amplitude is too big due to the neglect of the self-energy.

picture of magnetism. The average Σ_d, based on WKB expression Eq. 4.45 for the exchange interaction with Cu d-electrons, is added to correct the interstitial level for the exchange with 3d-electrons. Since 3d wave functions stick out of the muffin-tin radius, such correction seems to be needed. For Cu this correction has the order of 1 eV and practically does not affect the results of calculations.

5) **BP**. The broadened plasmon modification of the HL self-energy model. It can be used with all 4 previous models.

To show the significance of the self-energy I made a calculation of the Cu XAS with a ground state potential. I used only the Γ_{ch} contribution to the imaginary part of optical potential. As you can see on Figure 6.1 the amplitude of the EXAFS signal is too big due to neglect of the imaginary part of Σ. The inclusion of the self-energy drastically changes the calculated XAS signal. (see Figure 6.2). The amplitude of the signal in the EXAFS region now has the right amplitude. This shows that the theory for a photoelectron's mean free path, based on the self-energy calculations, works reasonably well at the high energies. The calculations were done with the same number of paths (434) for all self-energy models. The energy shift E_0 was

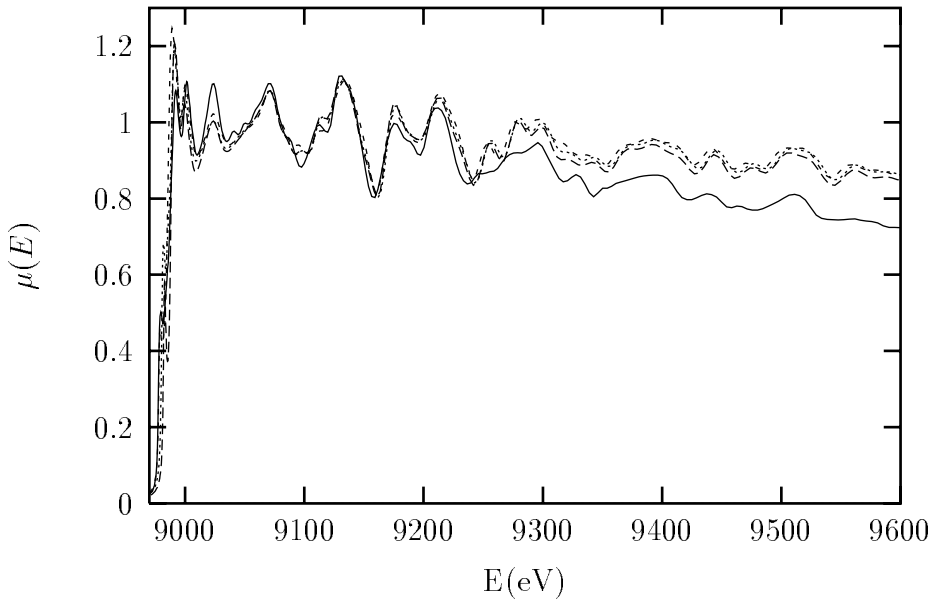

Figure 6.2: The Cu XAS. Experiment (solid) vs. calculations with the self-energy model: HL (long dashes), DH (dashes), NL(dots). The calculated spectra were shifted to match the experimental peak around 9023 eV.

fixed for all self-energy model by the requirement that the calculated first peak was reasonably reproduced: i.e. the peak is approximately in the center of the slope and its amplitude is not too big. All calculated spectra were shifted to match the absolute energy position of the forth peak around 9023 eV in the experimental data. This has been done in order to see, which of the self-energy models describes better the peak positions in the XANES region, which is shown on Figure 6.3. This picture provides a comparison of the real parts of different self-energy models. This picture shows that none of the self-energy model can adequately describe the peak positions in XANES, and therefore yet a better model is needed. Also, the certain aspects of the theory important for the XANES region are not included in the FEFF7 (e.g. self-consistent muffin-tin).

However, in the EXAFS region we still can compare the Σ models, where all important physics is accounted for by the FEFF7. In this region the real part for all self energy models is almost flat. Therefore, it is hard to compare the peak-to-peak distances visually. Since the nearest neighbor distance for the Cu-metal is well known, it is natural to compare the distances extracted from the EXAFS structural

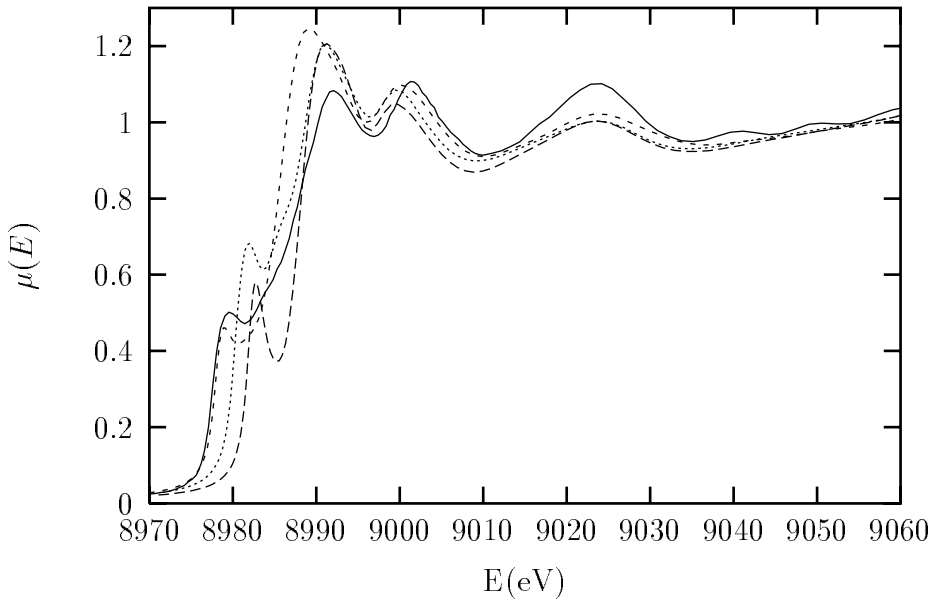

Figure 6.3: The Cu XANES. Experiment (solid) vs. calculations with the self-energy model: HL (long dashes), DH (dashes), NL(dots). The calculated spectra were shifted to match the experimental peak around 9023 eV.

analysis, obtained with the different self-energy models.

I used the FEFFIT program to fit the experimental data with 12 most important paths. The Fourier transforms were done with the $k_{min} = 2$, $k_{max} = 18$ and the k^2 weighting. The Hanning windows of the width $dk = 3$ were used. All fits were done in the R-space between the $r_{min} = 1.75$Åand the $r_{max} = 5.1$Å. (The same as in the Zabinsky thesis [24, p.79]). The Debye-Waller factors were taken from the correlated Debye model. The only fitting parameters were S_0^2, the McMaster correction σ_{mcm}, E_0 and the nearest neighbor distance shift – ϵ_r. A typical output for each fit is shown in the Table 6.1.

For each self-energy model two fits have been done: 1) to the experimental $\chi_{exp}(k)$ obtained by Newville at 10K, and 2) to the calculated $\chi_{thy}(k)$ with 434 paths, which also were used to calculate XAS on Fig. 6.2. Correspondingly, the 2 distance shifts were obtained ϵ_r^{exp} and ϵ_r^{thy}, which are shown in the Table 6.2 for different self-energy models. This table shows, that both HL and NL self-energy models can be used to extract the distances with the precision of the order of 3×10^{-3}Å. The DH model gives a much worse precision. The last column shows, how good is the calculated

Table 6.1: Example of the FEFFIT results. The fit of the experimental data with the HL self-energy.

parameter	best fit value	uncertainty
E_0	-0.8529	0.5451
ϵ	-0.0020	0.0023
s_0^2	1.0285	0.0554
σ_{mcm}	0.0014	0.0003

Table 6.2: Corrections to the nearest neighbor distances from the EXAFS analysis of the experimental and the calculated data.

Σ model	$\epsilon_r^{exp}(10^{-3}\text{Å})$	$\epsilon_r^{thy}(10^{-3}\text{Å})$
HL	-2.1 ± 2.3	0.9 ± 0.6
NL	1.7 ± 2.4	0.8 ± 0.5
DH	15.2 ± 2.7	16.9 ± 2.3

EXAFS signal compared with the experiment (second column). It shows that the NL model is the best. It also shows, that the DH model actually is not that bad, but requires an additional theoretical calculation, which is not convenient in practice, especially for unknown materials.

The Fourier transforms of the experimental and calculated (434 paths) EXAFS signal is shown on Fig. 6.4. The NL and HL models give very similar results, which can be made even closer to the experiment, if one will multiply the Fourier transform by $S_0^2 < 1$. Their Fourier transforms hard to distinguish on the picture, so only one is plotted. This figure also shows that the DH model is the worst, since it is impossible to have reasonable peak intensities, using just S_0^2 as a fitting parameter.

Yet another way to compare the self-energy models has been used by S.Zabinsky. [24] Using the back Fourier transform one can filter out the contribution from the nearest neighbor single scattering (SS) path. This was also done using the FEFFIT code with the back Fourier transform parameters $r_{min} = 1.75$, $r_{max} = 2.85$ and the Hanning windows of the width $dr = 0.5$. The results for the phase of SS path $\chi_{\rm ss}(k) = \text{ImA}_{\rm ss}(k) * \exp(i\phi_{ss}(k))$ are shown on Fig. 6.5 and Fig. 6.6. For the first picture the E_0 shifts (CORRECTIONS card) are made, and on the second all shifts

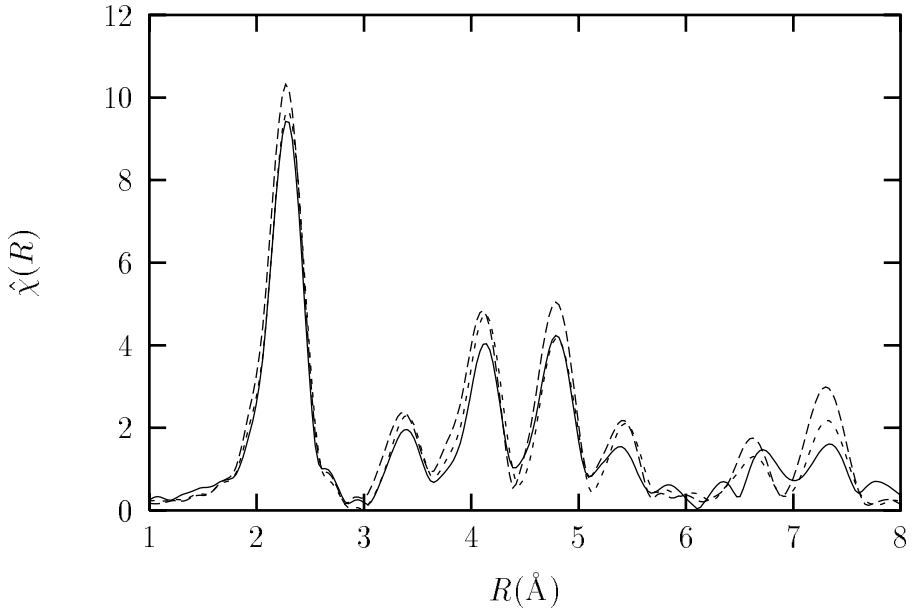

Figure 6.4: The Fourier transforms of the EXAFS signal – $\chi(R)$. The experiment (solid) vs. calculated with the HL (long dashes) and DH (dashes) models, using 434 paths.

are zero. Fig. 6.6 corresponds to Zabinsky Fig.4.8. By the comparison of these two figures, it is clear that in order to use a single scattering phase as a test for the self-energy models, the E_0 shift should be fixed by a more accurate self-consistent calculation of the muffin-tin potential. Actually, if I did not use the E_0 as a fitting parameter in the FEFFIT, then the corrections to the nearest neighbor distances were different: $\epsilon_r^{exp} = 1 \pm 3 \times 10^{-3}$Å for the HL model, and $\epsilon_r^{exp} = 4 \pm 3 \times 10^{-3}$Å for the NL model. Thus once again, the E_0 should be fixed by calculations for a better comparison of the self-energy models.

The distance determination test shows, that the NL model is the best for Cu. The other tests show that the HL model is comparable to the NL model, which works well in the EXAFS analysis for practically all materials. Therefore, a mixed model (HF + LDA) can be used to improve the *ab initio* calculations of the different electronic properties, not only XAS. The advantage lies in the core-valence separation. The Dirac-Fock exchange is enough for the core electrons, their correlations can be neglected. The LDA based HL model accounts for the correlations, which are important for the valence electrons. Actually this model can be put back into the atomic code,

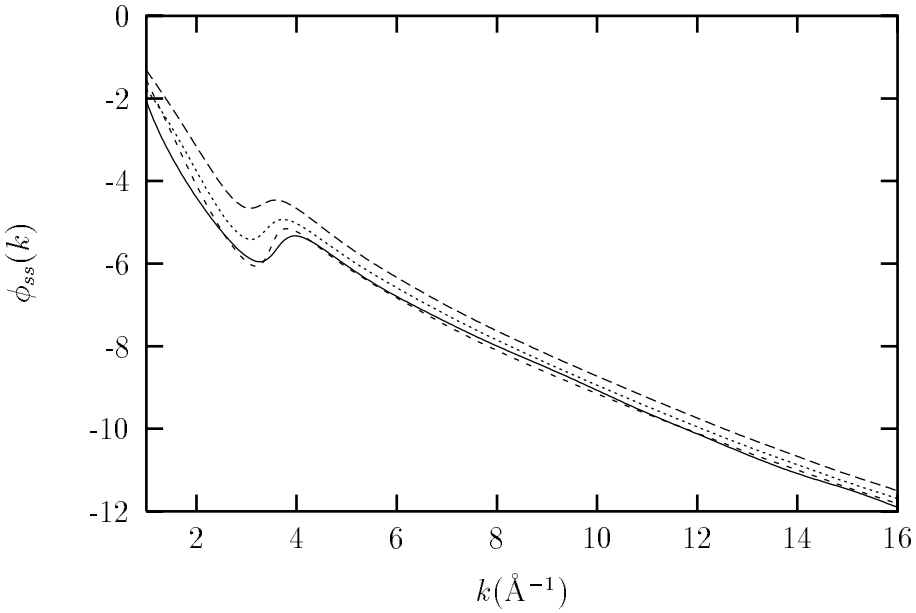

Figure 6.5: Single scattering phase for the experimental data (solid), and for the calculated with the HL (long dashes), DH (dashes) and NL (dots) self-energy models. E_0 shifts in the CORRECTIONS card have been made to set reasonable XANES.

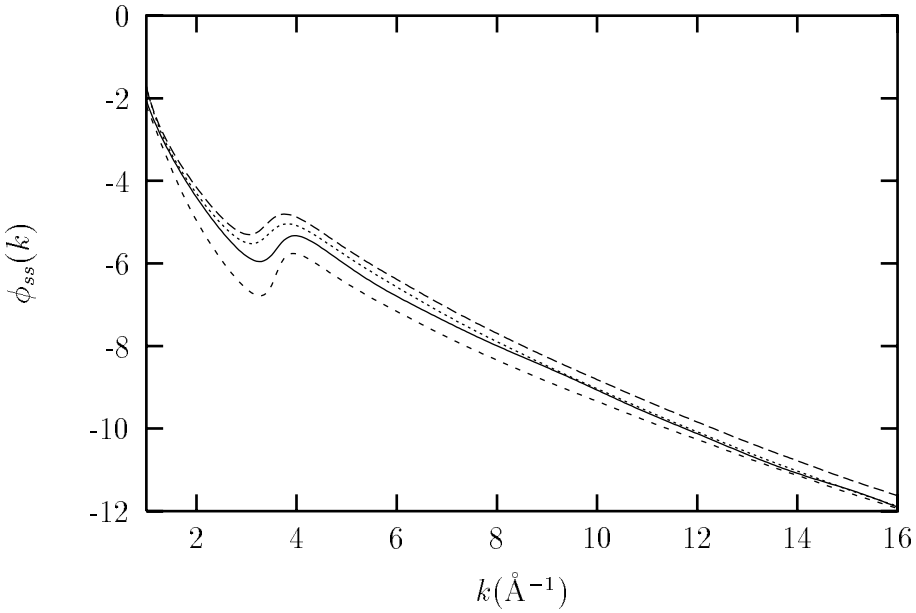

Figure 6.6: Single scattering phase for the experimental data (solid), and for the calculated with the HL(long dashes), DH (dashes) and NL (dots) self-energy models. The E_0 shifts in the CORRECTIONS card are zero.

as an improvement over the DF, since it includes in some way the RPA corrections to the self-energy due to the valence electrons. However, the improvements for the EXAFS analysis are not that impressive and lie within the error of the method (3 $\times 10^{-3}$Å). The HL model takes significantly less amount of time to calculate, and the extracted with a finite number of paths R_{fit} can be even closer to the real distance due to the cancelation of errors. Therefore, the HL model remains the implicit self-energy model in the FEFF7 code, but the experimental NL model should be tested on other materials, especially when the HL results are not satisfactory.

If one includes the d-electrons into a core, then the results for the NL model become worse, than the HL results. This is easily understood, since the correlations for the d-electrons are important (large polarizability, the binding energy is not too low), and the DF exchange completely neglects them. Therefore, the correlations should be somehow included in the SD model. The comparison of the SD and the NL models is presented on Fig. 6.7, and it definitely shows the advantages of the NL self-energy.

This test example also shows why do we still work on the self-energy improvement, if the HL model works pretty well. There is an experimental double peak structure around 9045 eV, which is not reproduced by the calculations with any model. Zabinsky showed, that it is connected with an overestimation of the imaginary part of the self-energy in this region by approximately 2 eV. This is clearly shown on his Fig.4.10, where the mean free path, reported by FEFF, compared with the results of Penn.[27] Since the maximum value of the ImΣ is about 5 eV, this is a very big effect. We have also tried out the broadened plasmon model, where we approximated the experimental inverse dielectric function of Cu by 106 Lorentzian curves . The fit was done for the $r_s = 2$, which is close to the calculated interstitial density of Cu. The peaks intensities in the XANES were improved, but this semi-empirical approach did not work either for the double peak region (see Fig. 6.8). Our procedure corresponds approximately to the same $\epsilon^{-1}(0,\omega)$, as in the Penn's calculations, but has different q-dependence of $\epsilon^{-1}(q,\omega)$

So a better self-energy model is needed, or some important physics is left behind. Both possibilities should be investigated.

1) Since the semi-empirical Penn's calculation gives good results, one can expect, that by doing the full GW procedure a better Σ can be obtained. This goes along

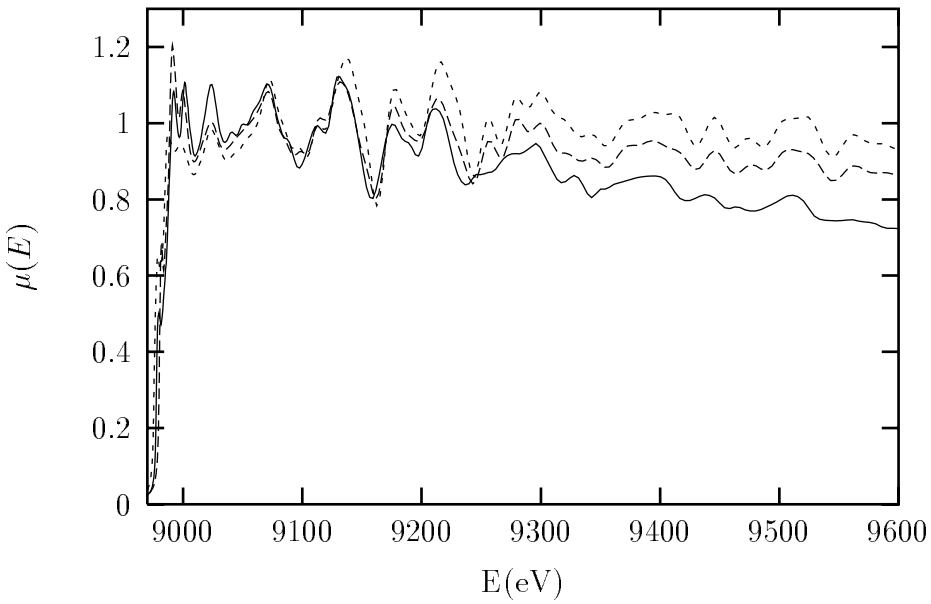

Figure 6.7: Cu XAS. The experiment (solid) vs. the calculations with the HL model. when d-electrons were treated as valence(long dashes) and as core (dashes) electrons. In the last case correction Σ_d was added, since d-electron wave function sticks out of the muffin-tin radius, but this correction practically does not affect the calculated results.

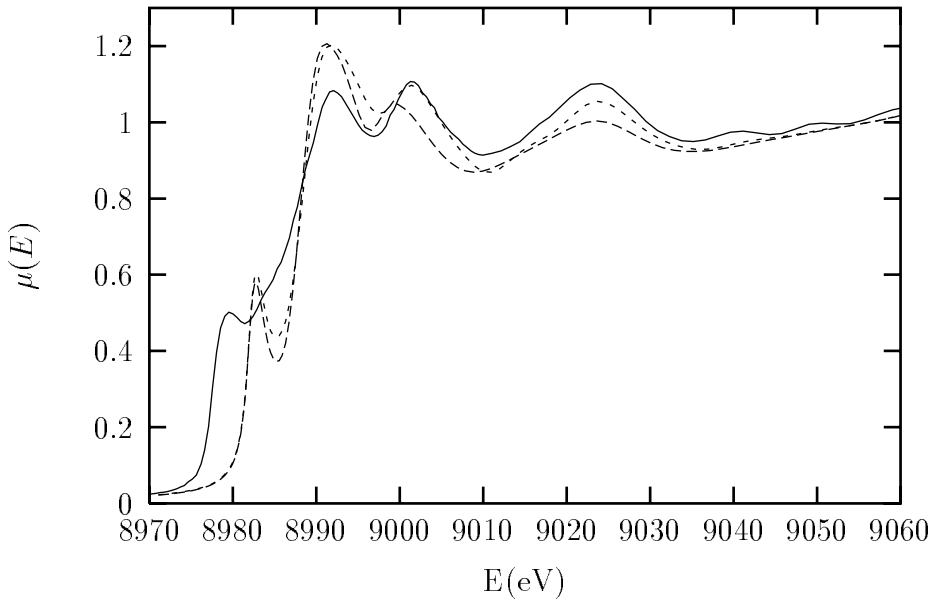

Figure 6.8: Cu XANES. The experiment (solid) vs. the calculations with the self-energy model: HL (long dashes), BP (dots). The calculated spectra are shifted to match the experimental peak around 9023 eV.

with construction of a self-consistent muffin-tin potential and a more accurate ground state calculation.

2) I've already mentioned an interesting cancelation theorem, proved by Hedin for the uniform electron gas. It states that the intrinsic and extrinsic losses cancel each other at the onset of the plasmon frequency. This means that the interference effects could be important around the plasmon frequency for real materials also, and a more accurate consideration of the screening dynamics is needed. Some work has been done along this direction by Rehr et al.

6.2 Determination of the coordination number for Cu.

The coordination number for Cu is 12 for fcc structure. Thus we test a simple atomic model for the excitation spectrum on Cu first, to see whether it works at least roughly. There is no need for a great precision here, since one usually wants to know some integer number.

The convolution with the model excitation spectrum is used in the FEFF7, whenever the MBCONV card is specified in the feff.inp file. The Fourier transform of the

convoluted EXAFS signal is shown on Fig. 6.9. The intensity of the first peak in the Fourier transform should be directly proportional to the coordination number. Since in the theoretical model $N_{nn} = 12$, then from the intensity of experimental nearest neighbor scattering peak we obtain the Cu coordination number:

$$N_{nn} = 12.8 \tag{6.1}$$

The error is still too big to say, that the coordination number determination from EXAFS is reliable. As one can see from Fig 6.9 and Fig 6.10, where the XAS convoluted with the excitation spectrum is shown. Both pictures will be better, if an atomic estimate of S_0^2 was larger. Therefore, atomic orbitals should be calculated with the presence of other atoms. It may reduce the changes in the orbitals and thus increase the calculated S_0^2. A free atom estimate is $S_0^2 = 0.82$. From the various fitting procedures it seems to be around 0.93. Another important point is that I used the DW factors from the correlated Debye model. The better DW factors can be possibly obtained using the molecular dynamics programs, and it will increase the reliability of the extracted N_{nn}.

In order to simulate what is the $S_0^2(E)$ dependence, I convoluted $\exp(i2kR_{nn})$ with the atomic excitation spectrum. The smooth atomic background (θ-function in this case) was also convoluted with the atomic excitation spectrum. The results are shown on Fig. 6.11. The lower curve corresponds to the calculated $S_0^2 = 0.82$ and the relaxation energy $E_R = 5.03$ Ryd. For the upper curve we used a different $S_0^2 = 0.91$, in order to see how the changes in S_0^2 calculations can affect the results. This test shows two points: 1) The EXAFS fitting with a constant multiplication factor is reasonable. 2) The atomic model should be improved to give better coordination numbers.

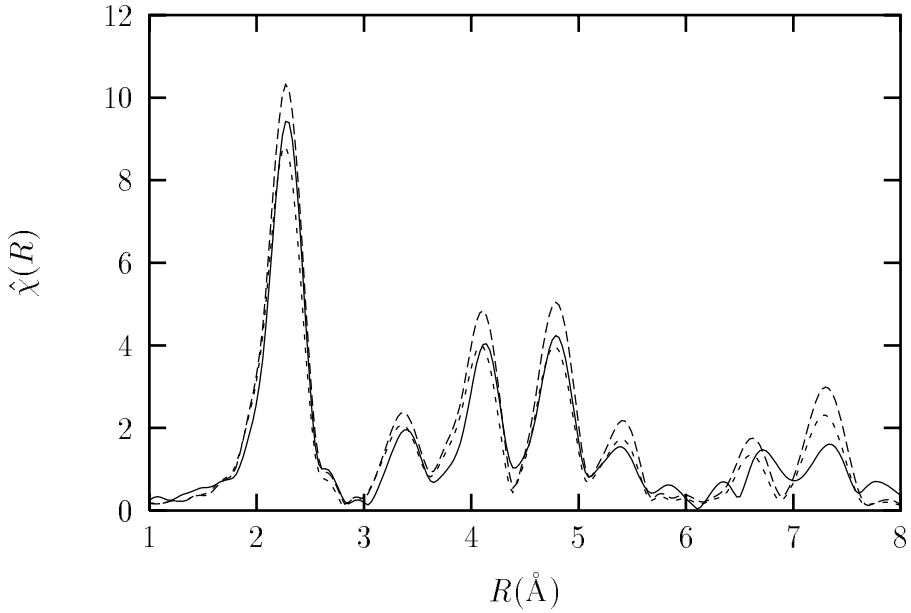

Figure 6.9: The Fourier transforms of experimental EXAFS (solid), and the calculated EXAFS with HL self-energy without (long dashes) and with (dashes) subsequent convolution with the atomic model excitation spectrum. The ratio of amplitudes of the NN peak is used to extract the coordination number.

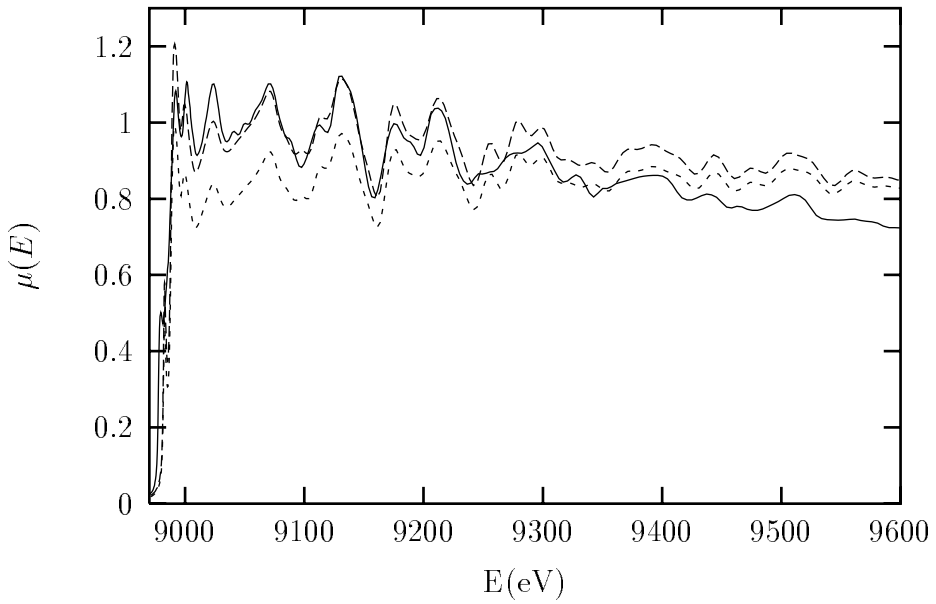

Figure 6.10: Cu XAS. The experiment (solid) vs. the spectra calculated with the HL self-energy without (long dashes) and with (dashes) subsequent convolution with the atomic model excitation spectrum.

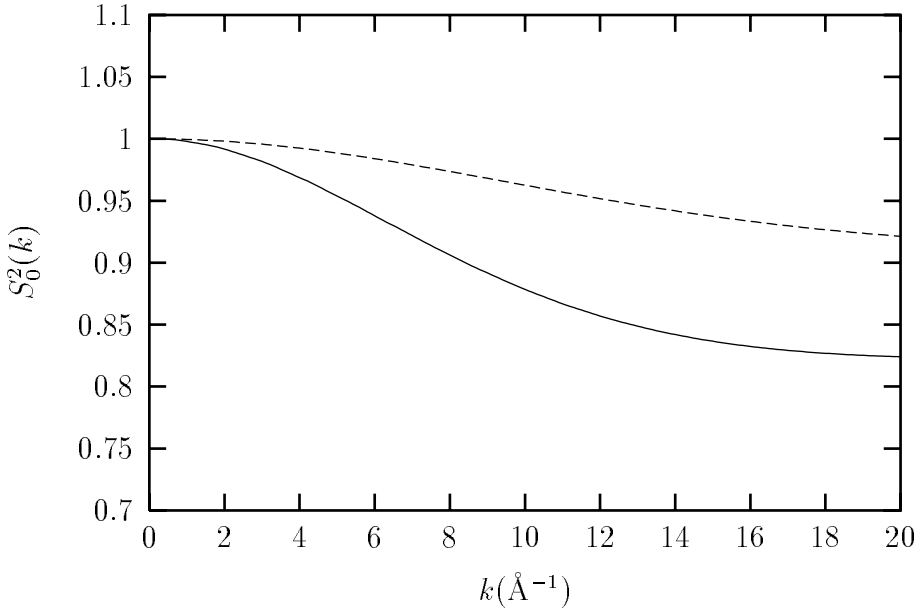

Figure 6.11: Energy dependence of reduction factor $S_0^2(k)$. The calculated relaxation energy $E_R = 5.03$ Ryd is used. Second atomic model parameter $S_0^2 = 0.82$ (solid line) and $S_0^2 = 0.91$ (dashes).

Chapter 7

DIPOLE MATRIX ELEMENTS.

The MS XAS calculation by formula 2.18 is naturally divided into calculation of the scattering Green's function and the dipole matrix elements. The Cu K-edge calculations (XANES calculations) do not provide a complete test on dipole matrix element calculation. They are not sensitive to the polarization dependence and the $\ell \rightarrow \ell - 1$ transitions. Relativistic effects on a photoelectron wave function are also small for Cu.

7.1 Polarization dependence in Cd monocrystal

It is impossible to investigate the polarization dependence of XAS on Cu, since it has cubic structure, and therefore, there is no polarization dependence of the signal in the dipole approximation. Polarization dependence is also impossible to observe for the polycrystalline materials. Thus polarization dependence is important for the monocrystals with symmetry lower than cubic, and for the surface studies, when atoms on the surface are different from those in the bulk. Polarization dependence has been already included in the FEFF6 by me, and this code has been used for the surface analysis.[70]

The results of first calculations for Cd have been already published in our review paper[12] to demonstrate that we can properly calculate the polarization dependent signal. However, the FEFF6 used $\ell \rightarrow \ell + 1$ approximation, which is not enough for the purpose of polarized EXAFS analysis. It was shown by Le Fevre et al., that the neglect of $\ell \rightarrow \ell - 1$ transitions can lead to errors in distance determination as much as 0.1 Å. [71] The present FEFF7 code calculates both contributions within the dipole approximation, and therefore is much better suited for analysis of the polarization dependent data.

The experimental results are compared with the FEFF7 simulations on Fig. 7.1 and Fig. 7.2 for two polarization directions. Le Fevre et al. have extracted a cross term contribution to the Cd XAS, which will be zero, if spherically averaged. For calculated

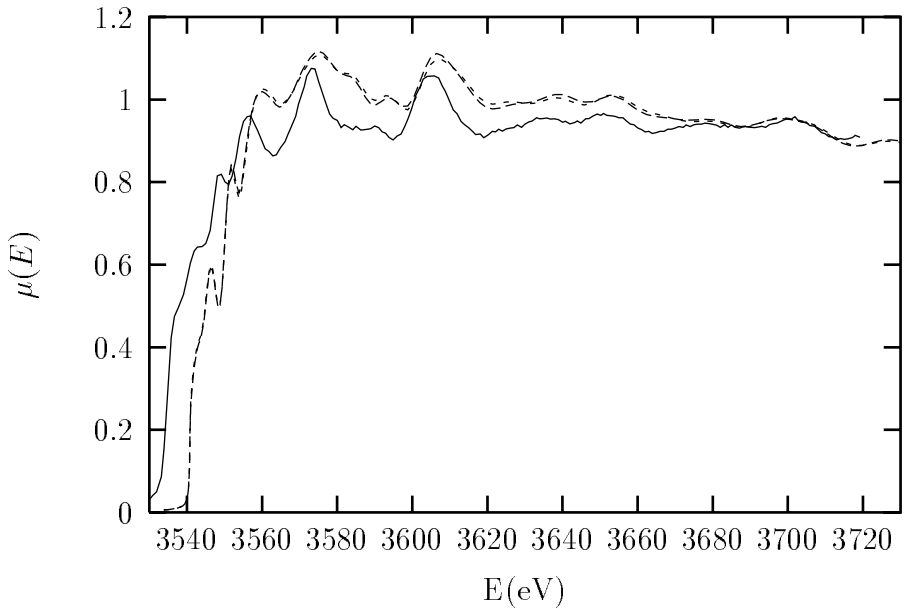

Figure 7.1: Cd L_3 EXAFS. Polarization vector is within the hexagonal plane of Cd hcp structure. The experiment (solid) vs. calculations with the FEFF7(long dashes). Calculation without the $\ell \to \ell - 1$ channel is shown by dashes.

spectra such extraction is straightforward. Theoretical and experimental cross term (χ_2 in [71]) are shown on Fig. 7.3. As you can see the overall sign agrees, and the amplitude agreement is reasonable, considering all complications in the experimental extraction of χ_2.

The more direct test will be to make the EXAFS analysis for two polarizations separately with FEFF7, and to check whether extracted distances are the same.

7.2 Relativistic simulations for Pu.

Before making a fully relativistic code, I wanted to see whether this could be important for any calculations. I chose Pu since it is heavy and relativistic effects are expected to be the largest. FEFF7 calculates the phase shifts (PHASE) by calling DFOVRG, which solves the Dyson equation for $\kappa = -\ell - 1$. To see, how different phase shifts are for $\kappa = \ell$, I simply changed the input quantum number κ for DFOVRG. In the non-relativistic limit this should not make any difference. There is a significant difference in the calculated L3 spectra on Fig. 7.4. This demonstrates, that calculation by the fully relativistic formula would be preferred for the heavy

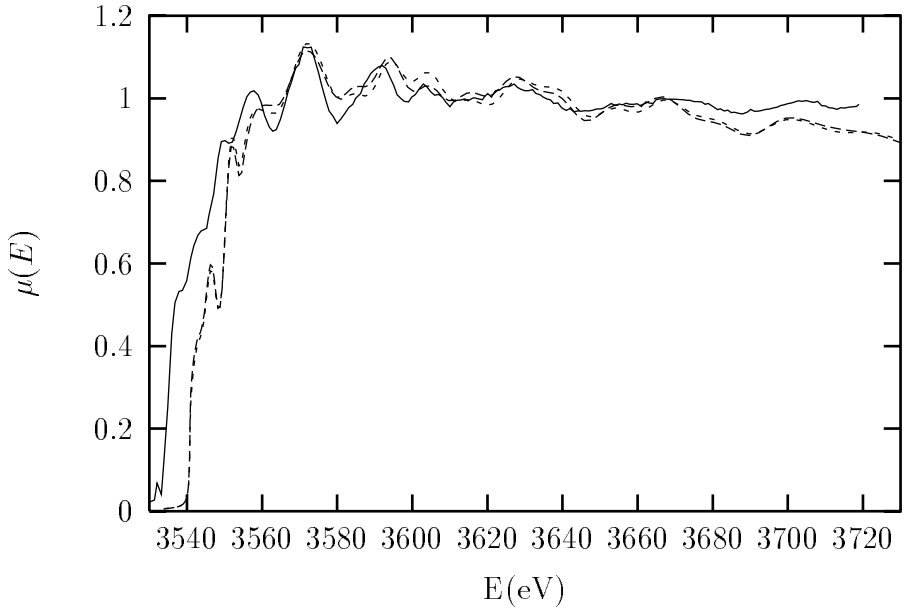

Figure 7.2: Cd L_3 EXAFS. Polarization vector is 80° from hexagonal plane of Cd hcp structure. The experiment (solid) vs. calculations with the FEFF7(long dashes). Calculation without the $\ell \rightarrow \ell - 1$ channel is shown by dashes.

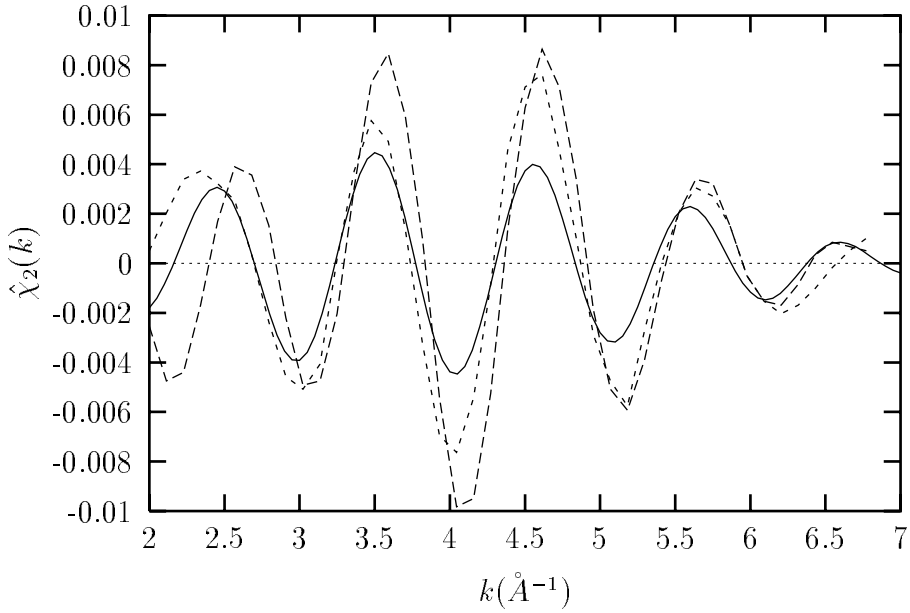

Figure 7.3: Comparison of the calculated (solid) cross term contribution (χ_2) with the experimentally extracted for 0°(dashes) and 80° (long dashes).

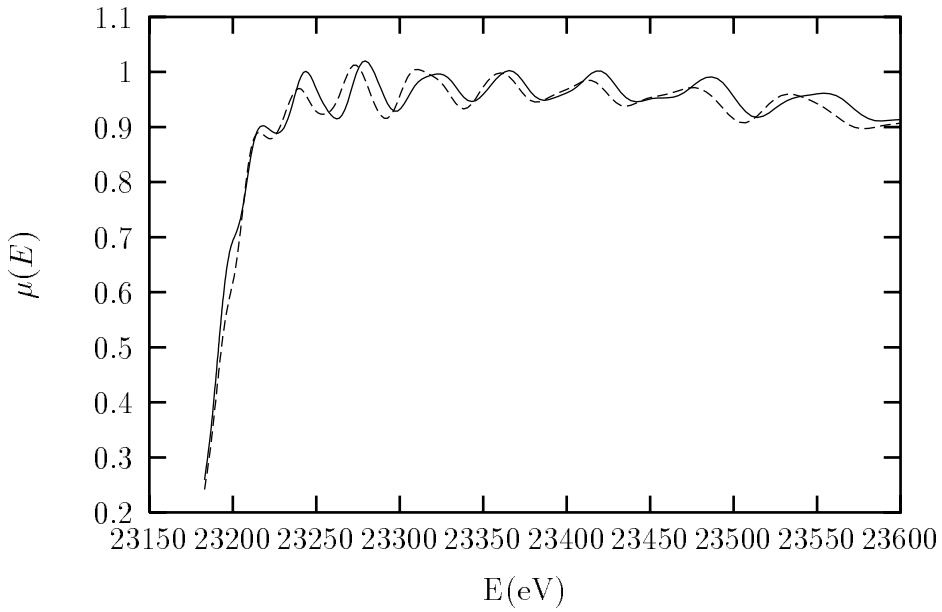

Figure 7.4: Comparison of two calculated Pu L_1 XAS with the phase shifts, taken for $j = l + 1/2$ (solid) and for $j = l - 1/2$(dashes). The fully relativistic calculation will be somewhere in between of those two curves.

elements.

The differences between phase shifts for $\kappa = -\ell - 1$ and $\kappa = \ell$ are shown on Fig. 7.5. As one can see, the largest SO effect is for $\ell = 1$ since the centrifugal potential in this case is the smallest, and photoelectron spends more time in the region with high electric field, responsible for the SO interaction. The largest difference in phase shift is 0.45 radians ($\approx 25°$), and one can expect that the interpolative formula 3.31 to treat simultaneously the SO and the spin-dependent interaction will work for all materials, since at least the SO in the final state can be treated in a perturbative fashion.

Thus simulations for Pu show that the full MS code is desired and formula 3.31 can be applied. This will save a lot of the calculational time, since it does not require to solve the coupled Dirac equation for every m_j, as in other treatment.[31] No big modifications of the FEFF7 are needed. Only the bookkeeping should be changed: four different phase shifts should be calculated instead of one. (Only two, if spin or SO interaction is zero.)

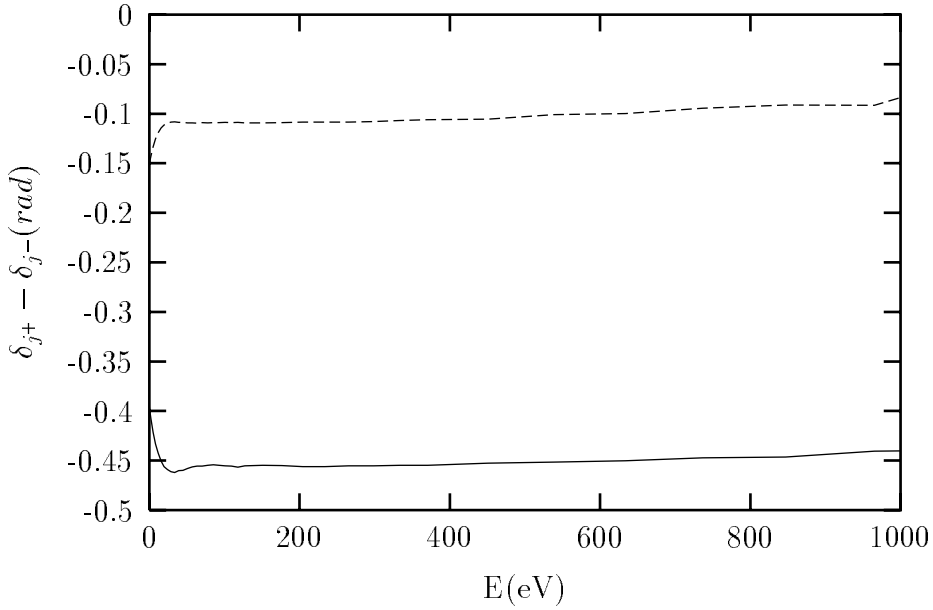

Figure 7.5: Differences in the phase shifts for $j = l + 1/2$ and for $j = l - 1/2$. The difference for $\ell = 1$ (solid) is larger than for $\ell = 2$ (dashes). The difference is decreasing with an increasing ℓ.

Chapter 8

MAGNETIC SYSTEMS.

The Cu test does not provide a test of the spin dependent potential. The construction of the self-consistent muffin tin potential is left for the future. I use the same atomic overlap picture to construct the spin-dependent muffin-tin potentials. It means, that the calculation of XANES signal is not very accurate. However, it should be sufficient for the EXAFS signal. The spin dependent density for each atom is easy to construct from the Hund's rules. If the relative spin alignment is known, then we have enough information to make the XMCD and the SPXAS calculations, using the FEFF7s code.

8.1 Gd L_2 and L_3 edges.

First, the non-relativistic expression (Eq. 3.19) has been used for the Gd L_2, L_3 edges. The calculations of XMCD were carried out for the polycrystalline Gd, using several exchange models, discussed below. The spin polarization of valence s-, p-, and d-electrons was neglected. It was assumed, that all 7 f-electrons have spin up for all Gd atoms. We have verified, that the overlapped atom potential used in FEFF gives to very high accuracy, the same spin-up and -down densities as the self-consistent, full potential band structure calculations of Albers et al.[72] The Debye-Waller factors were calculated, using the correlated Debye model[12] with Debye temperature $\Theta_D = 176$K and experimental temperature $T = 150$K. We ignored the many body amplitude corrections, i.e., we set $S_0^2 = 1.0$, which is usually accurate to about 20%.[73] Atomic absorption coefficients were normalized at $k = 12$ Å^{-1} to circumvent absorption variations close to the edge. The results are compared with the experimental data of Schütz et al.[30], both with and without the magnetic background subtracted. The overall normalization of experimental XMCD signal depends on many additional experimental factors: the degree of polarization of the x-ray beam, the amplitude reduction due to monochromators, the angle between the photon beam and the magnetization axis, and the degree of sample magnetization at

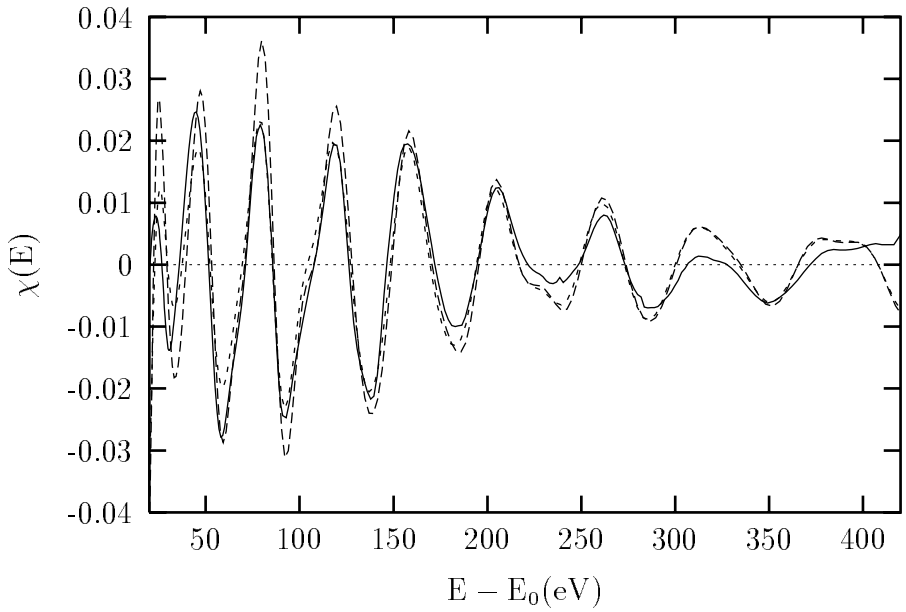

Figure 8.1: Gd L_2 EXAFS. Experiment (solid) vs. calculations with FEFF6 (long dashes) and FEFF7(dashes). Calculated spectra are shifted to match experimental peak around 78 eV.

a given temperature. The energy shift E_0 for all calculated exchange models was fixed by matching the calculated and the measured peak at 78 eV above threshold in the XAFS signal (Fig. 8.1). The shifts needed were 12 eV for the Hedin-Lundquist and 5 eV for the Dirac-Hara self-energy models used in FEFF.[73] We used the same energy shift for the corresponding XMCD calculations. Thus no additional free parameters were needed or used in the XMCD calculations by Eq. 3.5. For simplicity we only used paths with a half-total path length less than $R_{\rm max} = R_{\rm tot}/2 = 7.29$ Å; the number of significant inequivalent paths up to this distance is 65. This number is sufficient to illustrate the magnitude of the XMCD effect and much of the fine structure. The sign of the XMCD signal depends on convention; our choice is consistent with that of Schütz et al.[30]

As discussed above, a quantitative treatment of XMCD depends on the choice of exchange model, several of which were considered in our calculations:

1) Modified Von Barth-Hedin Exchange – The ground state spin-dependent local density approximation (LDA) exchange-correlation potential of Von Barth and Hedin (BH) $V_{gs}^{BH}(\rho, x)$,[25] where $x = \rho_\uparrow/\rho$. This model is frequently used in band-structure

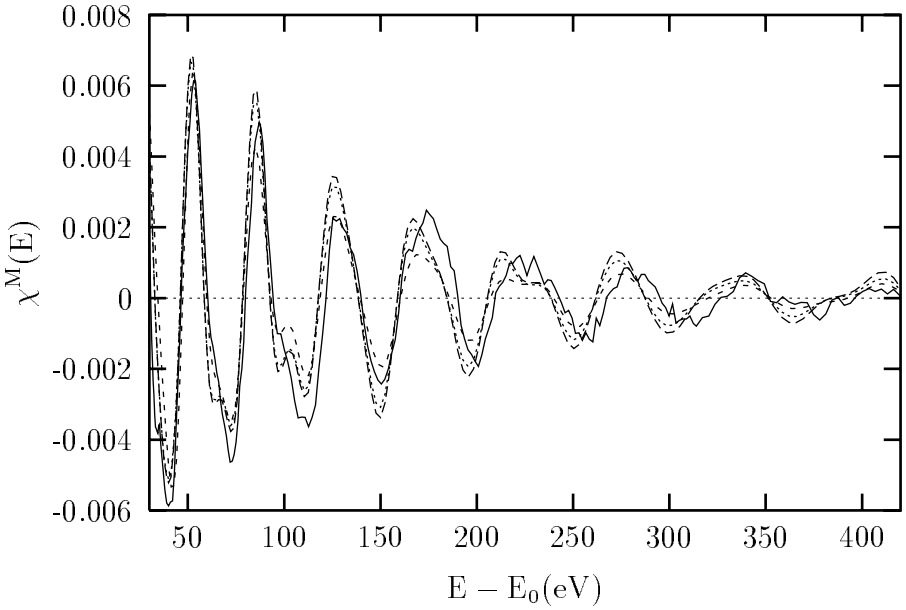

Figure 8.2: Gd L_2 XMCD with background subtraction: comparison of experimental (solid) and calculated spectra for the three models discussed in the text with the same energy shifts were made as for the XAFS spectra of Fig. ref gd.xafs. Dashes, short dashes and dots denote the modified Von Barth-Hedin, -Dirac-Hara; and -Hedin-Lundquist exchange-correlation models respectively.

studies of near-edge XMCD. However, the model has several drawbacks. For example, the difference in exchange potentials between spin-up and -down states is independent of energy, while the effect of the exchange interaction should generally decrease with increasing energy. Moreover, the model does not account for inelastic losses (or mean-free-path damping). Thus we also added a contribution from the spin-independent Hedin-Lundqvist self-energy[19] $\Sigma^{HL}(E,\rho)$, which gives a good approximation to inelastic losses in XAFS,[73]

$$V_{xc}(E,\rho,x) = V_{gs}^{BH}(\rho,x) + \Delta\Sigma^{HL}(E,\rho), \tag{8.1}$$

where $\Delta\Sigma^{HL}(E,\rho) = \left[\Sigma^{HL}(E,\rho) - \Sigma^{HL}(E_F,\rho)\right]$. The difference in $\Delta\Sigma$ ensures that V_{xc} reduces to the ground state exchange at the Fermi energy E_F.[73] Note (Fig. 8.2) that the calculated amplitude of the XMCD signal is in reasonable agreement with experiment in this case, but somewhat high at large energies.

Few corrections have been made to improve the FEFF6 later. The new results do not change the qualitative conclusion of previous calculations, but the amplitude of

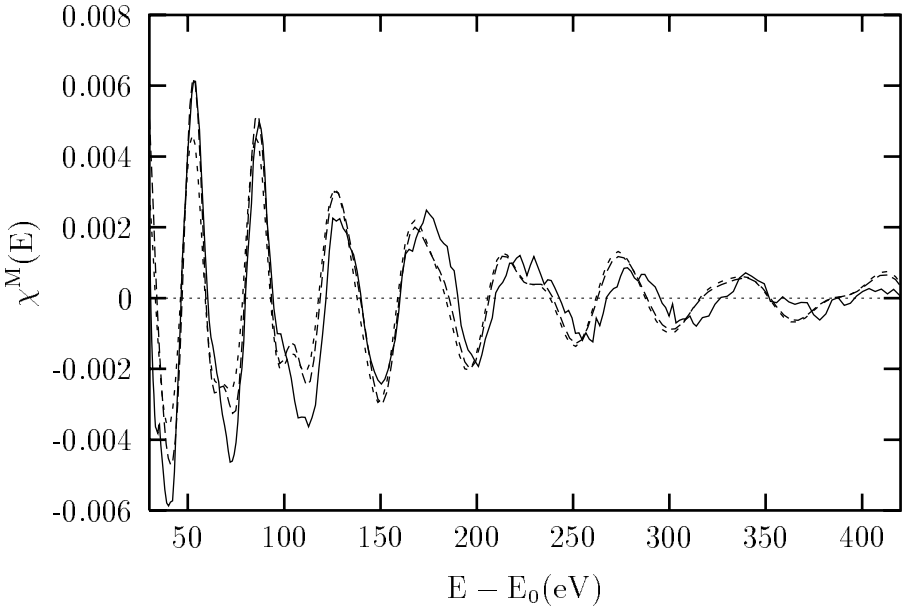

Figure 8.3: Gd L_2 XMCD with background subtraction: comparison of experimental (solid) and calculated spectra for the Von Barth-Hedin model, discussed in the text. The same energy shifts are made as for the XAFS spectra. The FEFF6 (long dashes) and the FEFF7 (dashes) results differ due to the different atomic codes.

the XMCD signal was slightly reduced (see Fig. 8.3, von Barth Hedin model is used for both FEFF6 and FEFF7).

2) Modified Dirac-Hara Exchange – An exchange model which possesses both energy and spin dependence is the local Dirac-Hara (DH) self energy.[73] Thus we tried DH exchange together with the imaginary part of the HL self-energy to account for losses,

$$V_{xc}(E,\rho,x) = V_{gs}^{BH}(\rho,x) + \left[\Sigma^{DH}(E,\rho,x) - \Sigma^{DH}(E_F,\rho,x)\right] + \mathrm{Im}\,\Delta\Sigma^{HL}(E,\rho). \quad (8.2)$$

With this model, the amplitude of the signal in 100-350 eV region is too small (Fig. 8.2), i.e., the DH exchange decays too rapidly with energy, owing to the neglect of dielectric screening. Also the DH self-energy often gives poor description of the XANES region.[73]

3) Modified Hedin-Lundqvist Exchange – We also attempted to simulate both the energy and spin dependence with an *ad hoc* model, constructed to have the same energy dependence for the difference in potentials between spin-up and -down as the Hedin-Lundqvist self-energy and the same spin-dependence as the potential of Von

Barth and Hedin,

$$V_{xc}(E,\rho,x) = V_{gs}^{BH}(\rho,x) + \frac{V_{gs}^{BH}(\rho,x)}{V_{gs}^{BH}(\rho,0.5)}\left[\Sigma^{HL}(E,\rho) - \Sigma^{HL}(E_F,\rho)\right]. \qquad (8.3)$$

This model gives the best amplitude vs energy dependence (Fig. 8.2). But clearly a less *ad hoc* treatment of spin- and energy-dependent exchange is desirable. However, for all three tested exchange models the sign, amplitude and general form of the XMCD signal agree reasonably well with experiment (Fig. 8.2). As noted by Von Barth and Hedin,[25] the spin-dependence of the correlation energy is important and can reduce the exchange interaction by a factor of about two. In Fig. 8.4 we show the calculated signal, including the smooth XMCD background, which we find to be essential to account for the observed XMCD behavior. Comparison with experimental data of Schütz et al.[30] shows good agreement with the calculated sign and amplitude of this background signal. Actually our calculations are doing well even in the XANES region (see Fig. 8.5), for which the calculations with background shown vs. experiment without background. However, still the amplitude of oscillations is in good agreement with experiment.

The magnetic scattering amplitude is the difference between two terms for spin-up and -down.

$$f_{mag} = f_\uparrow - f_\downarrow \qquad (8.4)$$

For the spin independent potential two terms are equal, and magnetic scattering amplitude is zero. Each term is a product of the backscattering amplitude (from the nearest neighbor) and the exponent of central atom phase shift:

$$f_s = f_s(\pi)\, e^{2\mathrm{i}\delta_s} = |f_s(\pi)| e^{\mathrm{i}\phi_s} \quad . \qquad (8.5)$$

If we assume, that the amplitude of backscattering signal is the same, then both terms will differ just by a phase. On Fig. 8.6 the total phase difference $(\phi_\uparrow - \phi_\downarrow)$ and contribution from the central atom $(2(\delta_\uparrow^c - \delta_\downarrow^c))$ are shown. As one can see, more than a half of the phase difference comes from the central atom in the EXAFS region. Central atom contribution is less in the XANES region. The phase difference between the average backscattering amplitude $\bar{f} = 1/2(f_\uparrow + f_\downarrow)$ and the magnetic f_{mag} is shown on Fig. 8.7. The fact, that this phase is close to $\pi/2$, confirms our assumptions, that the amplitudes of f_s are almost the same. Thus the total phase difference of two

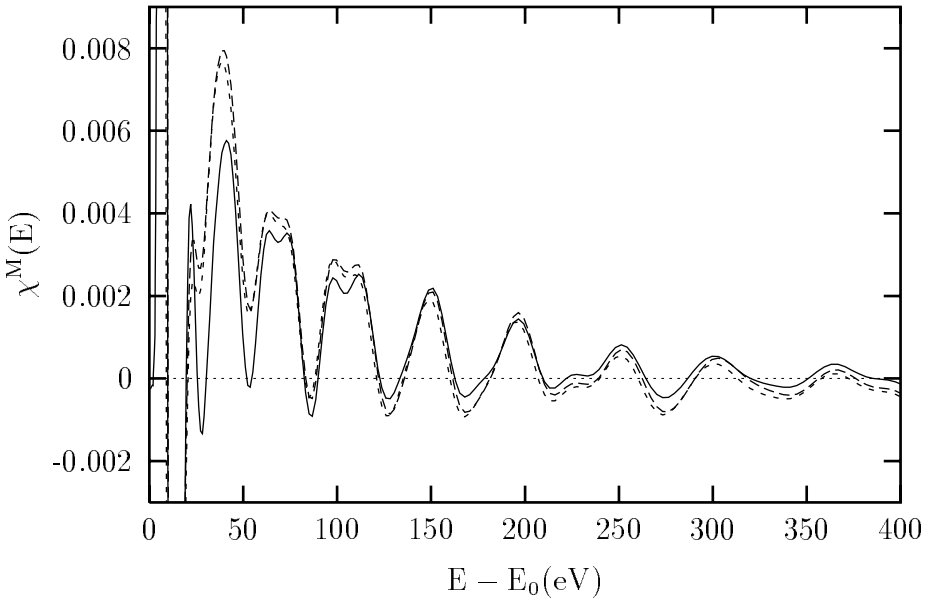

Figure 8.4: Calculated Gd L_2(dashes) and L_3 (long dashes) XMCD without background subtraction. The difference coincides with experimental data of Schütz et al., presented also in our paper. Solid line is the result of FEFF6 calculations, which were practically the same for both edges.

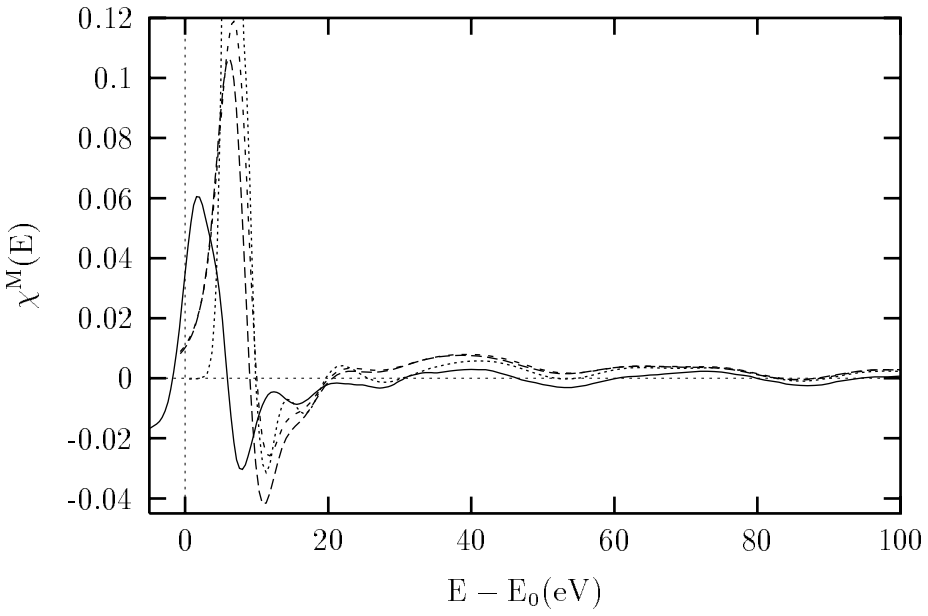

Figure 8.5: Calculated Gd L_2(dashes) and L_3 (long dashes) XMCD without background subtraction. Solid line is the experimental data with subtracted background. This is not a perfect comparison, but it still shows that even important features in XANES are reproduced.

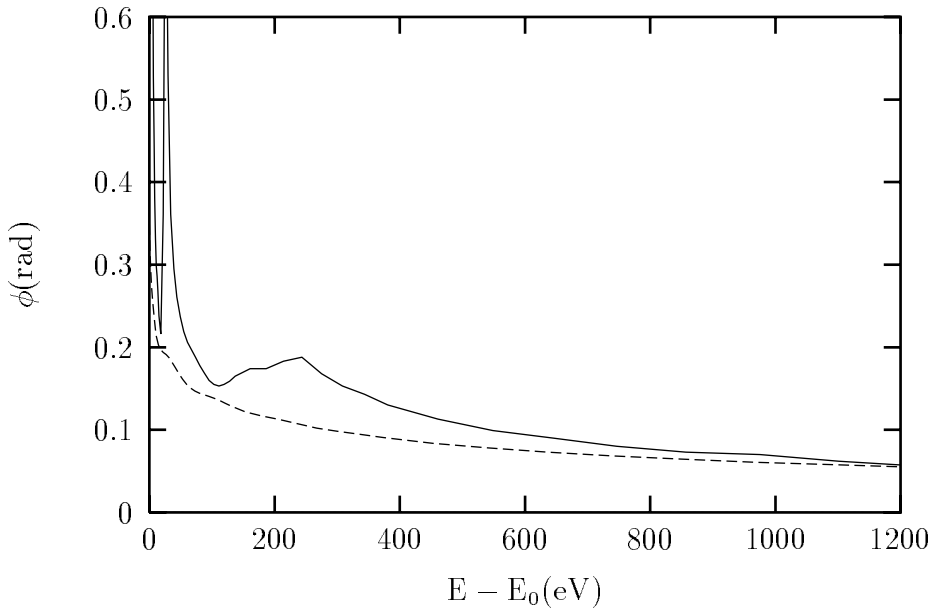

Figure 8.6: Contribution of the central atom phase shift (dashes) into the total phase difference between two effective backscattering amplitudes (solid). Central atom is essential for EXAFS region.

complex numbers is proportional to $|f_{mag}|$. The backscattering amplitude and the magnetic backscattering amplitude are shown on Fig. 8.8. Both amplitudes have a smooth energy dependence. Therefore both XAFS and XMCD oscillations carry *the same* information about the nearest neighbors, and can be used for the structural analysis. However, the EXAFS has a much larger amplitude and less noise. XMCD is zero for the non-magnetic materials and can be regarded as an important test for the spin alignment on different sites.

A formal expression for the XMCD signal for half-filled shells has been developed into a form suitable for calculations based on a generalization of the MS XAFS and XANES code FEFF (version 6).[12] The dominant mechanism responsible for XMCD at the L_2 and L_3 edges is the spin and energy dependent exchange interaction of the photoelectron with the Fermi sea. The amplitude of the XMCD is roughly proportional to an effective magnetic scattering amplitude $f_{\rm eff}^M$, which depends on the magnetization both of the scattering atom and the central atom. The last contribution is larger in the EXAFS region.

Matrix element effects are also important and give the XMCD a non-zero mean.

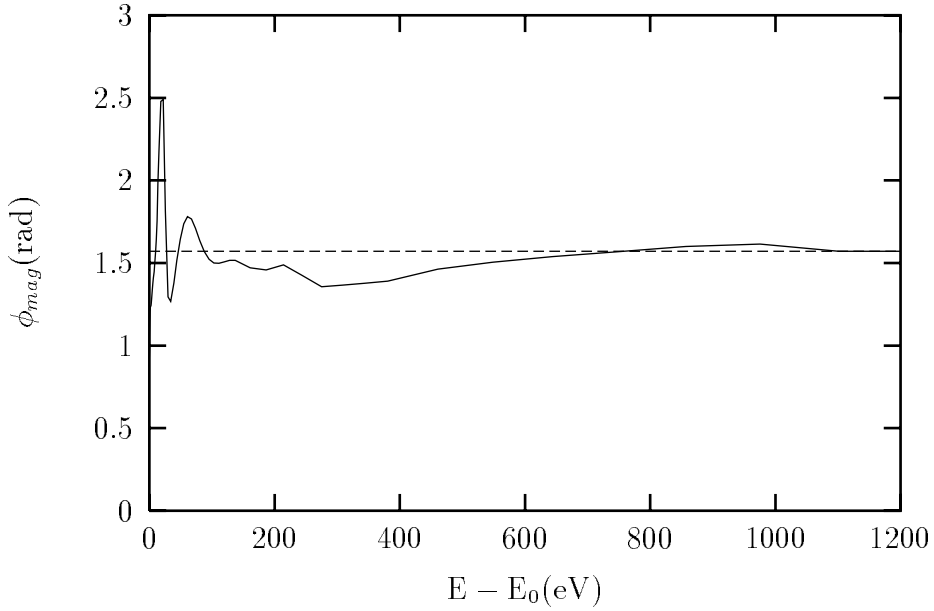

Figure 8.7: Phase difference between the magnetic f_{mag} and average backscattering amplitudes (solid). The $\pi/2$ value is shown by dashes.

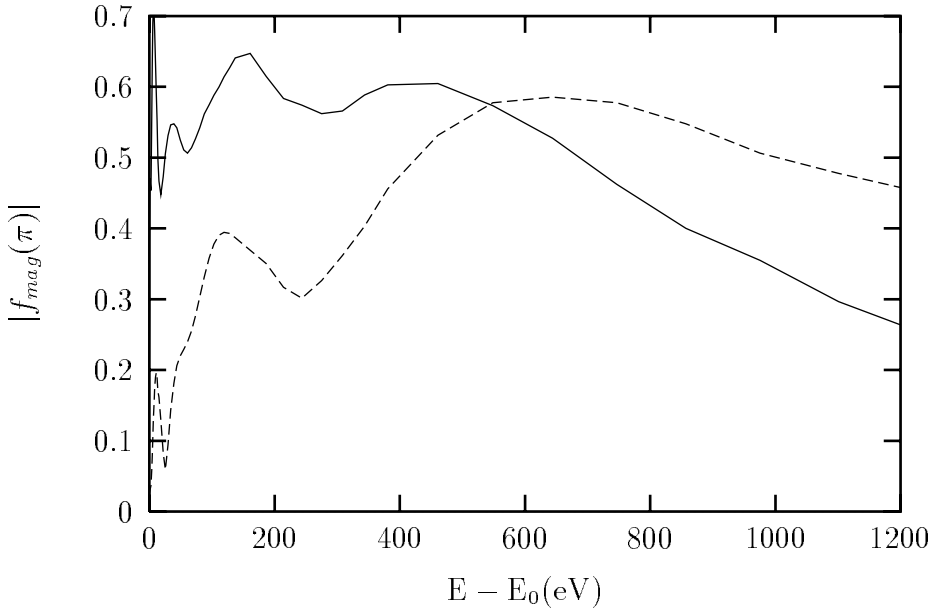

Figure 8.8: The amplitudes of magnetic $|f_{mag}|$(dashes) and average backscattering amplitudes $|\bar{f}|$ (solid).

Since the theory for other than half-filled shells can be more involved, the half-filled cases can provide a good test of various exchange potentials. All free parameters in the XMCD theory can be fixed by fitting the EXAFS signal. Our XMCD calculations above the L_2 and L_3 edges of Gd are in satisfactory agreement with the experiment, but differ somewhat between the various exchange models. This indicates that the main approximations made in derivation, namely the neglect of exchange splitting for core electrons and SO interaction for photoelectron are reasonable. However, *none* of the tested hybrid exchange models naturally accounts for the spin and energy-dependence of the exchange interaction, including inelastic losses. The smooth atomic background XMCD signal predicted by our theory agrees wells with that found in the experiment, illustrating the necessity of taking into account matrix element factors in the theory.

8.2 Gd L_1 edge and Fe K edge.

Since the non-relativistic formula for $\ell = 0$ edges gives a zero signal, these calculation provide an important test of the relativistic dipole matrix elements and of the interpolative approach to include relativistic effects for spin-dependent potentials. The calculated L_1 edge XMCD is compared to the experimental data of Schütz on Fig. 8.9. The calculated spectrum shows a good agreement even in the XANES region, which justifies *a posteriori* our recipe to construct the spin-dependent potential, and shows that the relativistic calculation of XAS works well.

The calculations for the Fe K-edge is compared to the experiment of Dartyge et al.[74] on Fig. 8.10. Actually, analogous calculations were carried out by the LMTO method [75]. Our calculations agree better with the experiment not only in the EXAFS, but in the XANES also.

8.3 K edge SPXAS for antiferromagnetic MnF_2.

The XMCD signal for the antiferromagnetic material is zero. However, the SPXAS signal won't be zero, since here the magnetic order relative to the central atom spin is important. Even if only the central atom in the cluster has a nonzero total spin and the rest of the atoms are nonmagnetic, the SPXAS signal will be nonzero due to the difference in central atom phase shifts. To demonstrate the amplitude of effect I

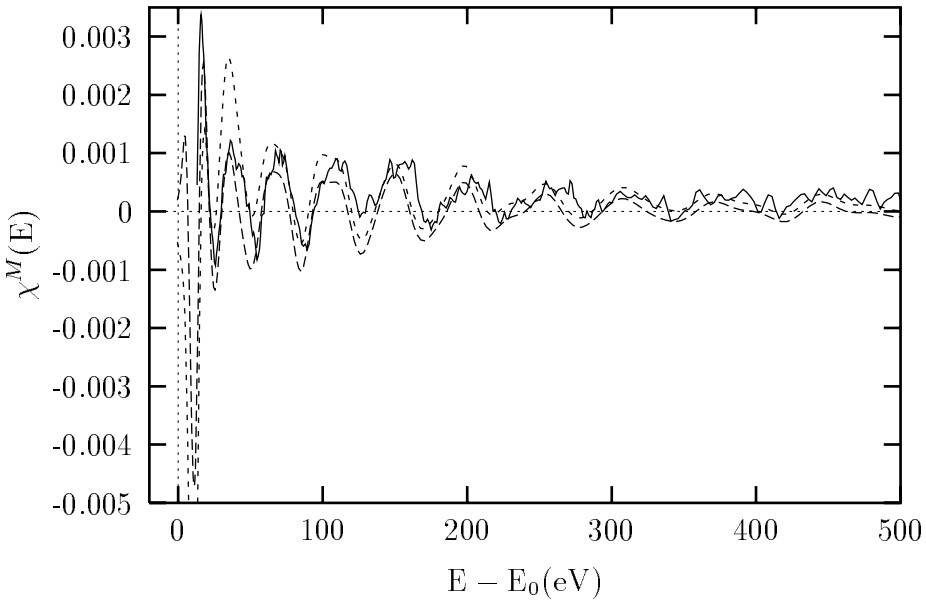

Figure 8.9: Calculated Gd L_1 XMCD with (dashes) and without (long dashes) background subtraction vs. experiment (solid).

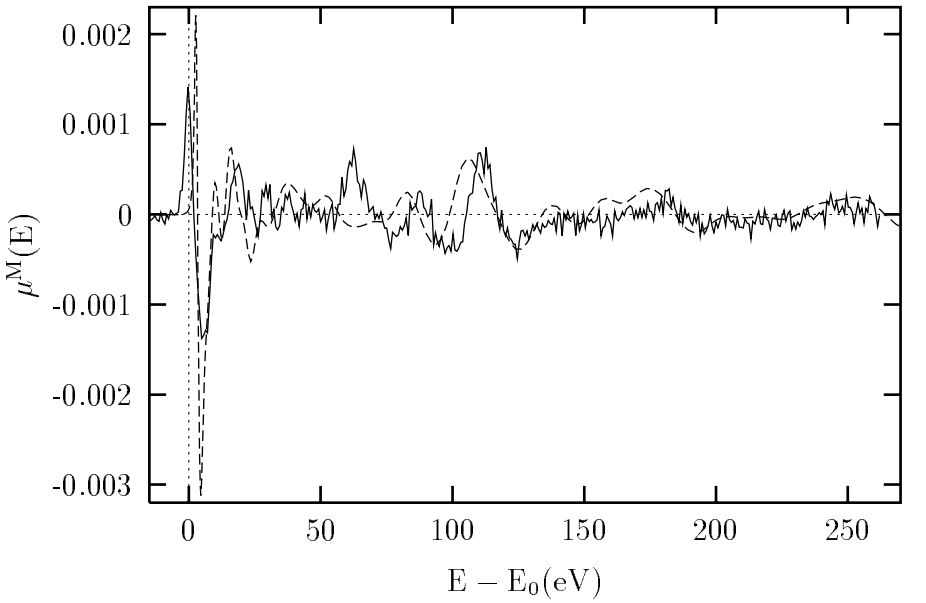

Figure 8.10: Calculated Fe K edge XMCD vs experimental data of Dartyge et al..

made calculations for two materials.

MnF_2 is antiferromagnetic and it's SPXAS has been first measured by Hamalainen et al.[76]. The calculations have been done previously by Soldatov et al.[67] for the XANES region, using full MS and self-consistent potential. However, they used the Dirac-Hara self-energy in their calculations, which explains that the calculated difference between spin-up and -down signals is too big, compared to the experiment around 6565 eV photon energy. The use of the von Barth-Hedin prescription for spin- dependent potential will reduce the calculated difference by approximately a factor of 2. The results of my calculations are shown on Fig. 8.11. Calculated with the FEFF7s signal agrees well with the experiment at the energies above 7 eV from the threshold. As one can see the amplitude of SPXAS signal around 6565 eV is improved, but the double peak structure at the edge is not as well resolved in my calculations. I tried to include more paths to achieve the full MS, but it did not help. Actually, the double peak structure appeared only, when I included the calculation of Debye-Waller factors for Debye temperature 350°K and experimental temperature 300°K. It may be, that Soldatov et al. were able to get a better double peak structure, since they used self-consistent potential. This agrees with our expectations that SCF could be important in the XANES, and not very important for the EXAFS. However, I found that even XANES calculations for MnF_2 are sensitive to the Debye-Waller factors, and they are not that easy to incorporate into the full MS approach used by Soldatov et al..

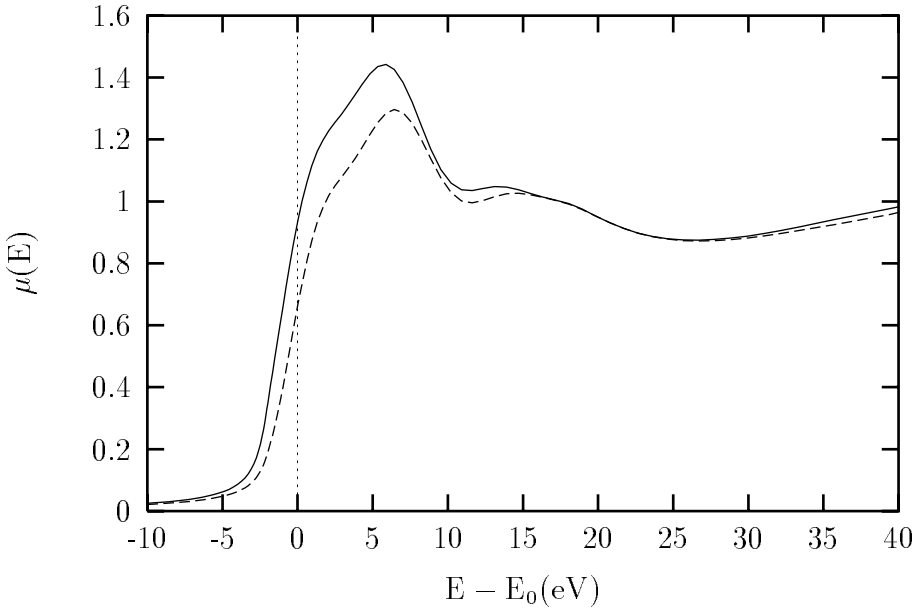

Figure 8.11: Calculated K-edge SPXAS for MnF_2.

Chapter 9

CONCLUSIONS

By the 70's all the mechanisms responsible for XAFS were already understood.[5] However, reliable *ab initio* calculations were not available at that time. The important step was the inclusion into FEFF3 code[73] of HL self-energy model, which reasonably well accounts for mean free path of photoelectron and the peak shifts in XANES. Curved wave corrections were correctly accounted for MS terms in FEFF5, using separable Rehr-Albers representation on free Green's function. This representation is necessary for a fast MS code. The proper consideration of Debye-Waller factors is needed for the agreement between calculations and experiment. Some codes use Debye-Waller factors as fitting parameters, but the correlated Debye model, introduced in FEFF6 [12], gives reasonable estimates of these factors[69]. Path filters were developed by Zabinsky for FEFF5 and FEFF6 and also made MS calculations faster. Despite the success of FEFF6 for EXAFS analysis, it still has several shortcomings. It is an LDA based code, but non-local DF exchange is better for description of core orbitals. Also FEFF6 neglects $\ell \rightarrow \ell - 1$ dipole transitions. The muffin tin potential is not self-consistent. Non-relativistic approximation is used to calculate cross-section and partial wave phase shifts. The corrections due to the ban on transitions below the chemical potential were not properly accounted for. The many body excitation spectrum is accounted for only by single factor S_0^2.

The principal mechanisms for XMCD were described by Erskine and Stern in 1975. [16] The first measurements were done in 1987 by Schütz et al.[15] The calculations in XANES region were done by Ebert et al. [31] No XMCD calculations for EXAFS region were available. The importance of spin-orbit interaction in the final state for K,L_1 XMCD was shown by Brouder and Hikam.[77] However, they used a non-relativistic expansion to include this interaction. Another approximate approach was suggested by Ebert and Guo. The coupled Dirac equation should be solved. This approach increases EXAFS calculations by a factor 50, which is a very large price for small corrections. In 1992 Thole et al. discovered new sum rules to separate

the orbital and spin contribution to the net magnetization. The error for the known materials is of order 10% . There may be two origins of this error: 1) normalization factor and 2) excited state expectation values differ from ground state values by approximately 10% .

In the present dissertation I attempted to overcome the above mentioned shortcomings and problems of X-ray absorption theory and FEFF code through a series of developments:

1) Theory. Several new theoretical results have been obtained:

- Interpolative approach to treat simultaneously SO interaction and spin-dependent potentials has been developed, and it's applicability has been tested by the phase shift calculations for Pu and Gd.

- New nonlocal self-energy models have been introduced, using core-valence separation. They can be used to improve atomic orbitals, using embedded atom calculation.

- Algorithms to calculate SPXAS and XMCD have been developed.

- A new way to derive the sum rules for XAS has been used. A many-body analysis, based on the sudden approximation, has been made. It showed, that the quantities, obtained from the sum rules, are the GROUND state expectation values, and not the excited state values.

2) New code. A version of XAS code (FEFF7) has been developed from the FEFF6. The following serious steps toward a fully relativistic code have been made:

- A new Dirac-Fock atomic code (SCFDAT) has been made from the Desclaux code to replace FEFF6's LDA based Dirac-Fock-Slater atomic code.

- A subroutine (DFOVRG) has been developed to calculate phase shifts for both values of j ($\ell \pm 1/2$) and for the complex potential.

- Relativistic calculation of the dipole matrix elements has been introduced (α-form). The cross section in the file xsect.bin is written in $\mathring{A}^2$ in order to make a connection with possible absolute XAS measurements. Now the contributions from both $\ell \rightarrow \ell \pm 1$ are included in calculations.

- Convolution with the Lorentzian due to the core-hole lifetime is made, in order to remove contribution to XAS from the poles of scattering Green's function below the chemical potential.

- Subroutines to calculate XMCD and SPXAS have been added.

3) Tests comparing theory and experiment. The code has been tested on a number of materials. These tests showed that:

- Cu: Non-local self-energy model worked best, but improvements over HL model for distance determination were within the limits of EXAFS method precision, shown to be 3×10^{-3}Å. Therefore HL self-energy remains standard for EXAFS analysis. The coordination number can be obtained, using *ab initio* atomic model for intrinsic excitations, but the embedded atom calculations needs to be done for better precision.

- Cd: The inclusion of $\ell \rightarrow \ell - 1$ transitions is very important to improve the polarized EXAFS analysis.

- Gd XMCD, Mn SPXAS: Agreement with the experiment shows, that approximations to construct the spin-dependent potentials are reasonable. They provide an important test for the theory, and a way for better understanding of magnetism.

- Comparison with other calculations shows, that the important (for XANES) ingredient, missing in FEFF codes, is the self-consistent muffin tin potential. However, it is not required for the EXAFS analysis.

However several problems are not yet resolved and number of improvements of the present code can be made. With relativistic spin-dependent theory, developed in present thesis, it is straightforward to make the code fully relativistic. This may be especially important for the heavy elements. Self-consistent calculations of muffin-tin potential should be added for better XANES calculations. Self-consistent spin-dependent potentials require some theoretical work. Better Σ model can be build from the self-consistent density, using the consistent GW approach, not it's LDA version. *Ab initio* molecular dynamics could be added to calculate the Debye-Waller

factors and better EXAFS, but the present Car-Parrinello codes are not fast enough. Outer sphere corrections may be added to achieve better results for small complexes.

FEFF codes can be modified for the other spectroscopies, involving propagation of electron in solid, since all main ingredients of the theory will remain the same. For XPS calculations just the boundary conditions need be modified. The dipole matrix elements should be replaced by the matrix elements of Coulomb interactions for EELS. Both real and imaginary parts of the scattering Green's functions are needed for the DAFS along with two different polarization vector in two dipole matrix elements. The LEED calculation will require to add the scattering from all atoms, and subroutines can be borrowed from the LEED calculation programs.

All aspects of *ab initio* x-ray absorption calculations were addressed in this dissertation. Several major problems have been resolved, especially the spin and relativistic aspects of the theory. However many exciting developments are yet to be done in the field of *ab initio* calculations.

BIBLIOGRAPHY

[1] H. Fricke. *Phys. Rev.*, **16**:202, 1920.

[2] G. Hertz. *Z. Phys.*, **3**:19, 1920.

[3] R. de L. Kronig. *Z. Phys.*, **70**:317, 1931.

[4] R. de L. Kronig. *Z. Phys.*, **75**:468, 1932.

[5] D. E. Sayers, E. A. Stern, and F. W. Lyttle. *Phys. Rev. Lett.*, **27**:1204, 1971.

[6] D. E. Sayers, F. W. Lyttle, and E. A. Stern. *Adv. X-Ray Anal.*, **13**:248, 1970.

[7] Edward A. Stern and Steve M. Heald. *Handbook on Synchrotron Radiation*, volume 1, chapter 10, Basic Principles and Applications of EXAFS. North-Holland Publishing Company, 1983.

[8] B. K. Teo and P. A. Lee. *J. Am. Chem. Soc.*, **101**:2815, 1979.

[9] A. G. McKale, G. S. Knapp, and S. K. Chan. *Phys. Rev. B*, **33**:841, 1986.

[10] N. Binsted, S. L. Cook, J. Evans, G. N. Greaves, and R. J. Price. *J. Am. Chem. Soc.*, **109**:3669, 1987.

[11] J. B. Pendry. Low energy electron diffraction, 1974. SERC Daresbury Laboratory MUFPOT program based on the work described in.

[12] S. I. Zabinsky, J. J. Rehr, A. Ankudinov, R. C. Albers, and M. J. Eller. Ms calculations of x-ray-absorption spectra. *Phys. Rev. B*, **52**:2995, 1995.

[13] M. Benfatto, C. R. Natoli, C. Brouder, R. F. Pettifer, and M-F. Ruiz-Lopez. Polarized curved-wave extended x-ray absorption fine structure: theory and application. *Phys. Rev. B*, **39**:1936, 1989.

[14] J. J. Rehr, J. Mustre de Leon, S. I. Zabinsky, and R. C. Albers. *J. Am. Chem. Soc.*, **113**:5135, 1991.

[15] G. Schütz, W. Wagner, W. Wilhelm, P. Kienle, R. Zeller, R. Frahm, and G. Materlik. *Phys. Rev. Lett.*, **58**:737, 1987.

[16] J. L. Erskine and E. A. Stern. *Phys. Rev. B*, **12**:5016, 1975.

[17] A. Messiah. *Quantum Mechanics*. Interscience, New York, 1961.

[18] G. D. Mahan. *Many-particle physics*. Plenum Press, New York, 1981.

[19] L. Hedin and S. Lundqvist. *Solid State Physics: Advances in Research and Applications*, volume **23**, pages 1– 181. Academic Press, Inc., 1969.

[20] J. J. Sakurai. *Advanced Quantum Mechanics*. Addison-Wesley Publishing Company, 1967.

[21] J. J. Rehr and R. C. Albers. Scattering-matrix formulation of curved-wave multiple-scattering theory: Application to x-ray-absorption fine structure. *Phys. Rev. B*, **41**:8139, 1990.

[22] I. P. Grant. *Advan. Phys.*, **19**:747, 1970.

[23] B. R. Judd. *Operator techniques in Atomic Spectroscopy*. McGraw-Hill, New York, 1963.

[24] S. I. Zabinsky. *Multiple Scattering Theory of XAFS*. PhD thesis, University of Washington, 1993.

[25] U. von Barth and L. Hedin. A local exchange-correlation potential for the spin polarized case:i. *J. Phys. C*, **5**:1629, 1972.

[26] H. Stragier, J. O. Cross, J. J. Rehr, L. B. Sorensen, C. E. Bouldin, and J. C. Woicik. Diffraction anomalous fine structure: a new x-ray structural technique. *Phys. Rev. Lett.*, **69**:3064, 1992.

[27] D. R. Penn. Electron mean-free-path calculations using a model dielectric function. *Phys. Rev. B*, **35**:482, 1987.

[28] E. D. Crozier, J. J. Rehr, and R. Ingalls. Amorphous and liquid systems. In D. C. Koningsberger and R. Prins, editors, *X-Ray Absorption: Principles, Applications, Techniques of EXAFS, SEXAFS, and XANES*, pages 375–384. John Wiley & Sons, 1988.

[29] A. Ankudinov and J. J. Rehr. *Phys. Rev. B*, **52**:10 214, 1995.

[30] G. Schütz, R. Frahm, P. Mautner, W. Wagner R. Wienke, W. Wilhelm, and P. Kienle. *Phys. Rev. Lett.*, **62**:2620, 1989.

[31] H. Ebert, P. Strange, and B. L. Gyoffy. *J. Appl. Phys.*, **63**:3055, 1988.

[32] B. T. Thole, P. Carra, and G. van der Laan. *Phys. Rev. Lett.*, **68**:1943, 1992.

[33] P. Carra, B. T. Thole, M. Altarelli, and X. Wang. *Phys. Rev. Lett.*, **70**:694, 1993.

[34] R. Wu, D. Wang, and A. J. Freeman. *Phys. Rev. Lett.*, **71**:3581, 1993.

[35] A. Ankudinov and J. J. Rehr. *Phys. Rev. B*, **51**:1282, 1995.

[36] M. Altarelli. *Phys. Rev. B*, **47**:597, 1993.

[37] B. T. Thole and G. van der Laan. *Phys. Rev. Lett.*, **67**:3306, 1991.

[38] P. Carra, H. König, B. T. Thole, and M. Altarelli. *Physica B*, **192**:182, 1993.

[39] G. D. Mahan and K. R. Subbaswamy. *Local Density Theory of Polarizability*. Plenum Press, New York, 1990.

[40] L. J. Sham and W. Kohn. One-particle properties of an inhomogeneous interacting electron gas. *Phys. Rev.*, **145**:561, 1966.

[41] D. J. Thouless. *The Quantum Mechanics of Many-Body System.* Academic Press, 1961.

[42] E. L. Shirley, 1996. report at the APS Meeting.

[43] F. Aryasetiawan and O. Gunnarsson. Electronic structure of nio in the gw approximation. *Phys. Rev. Lett.*, **74**:3221, 1995.

[44] F. Aryasetiawan. Self-energy of ferromagnetic nickel in the gw approximation. *Phys. Rev. B*, **46**:13 051, 1992.

[45] P. A. Dirac. *Proc. Camb. Phil. Soc.*, **26**:376, 1930.

[46] J. Lindhard. *Dan. Math. Phys. Medd.*, **28**(8), 1954.

[47] L. Hedin. *Phys. Rev.*, **139**:A796, 1965.

[48] M. Newville, P. Livins, Y. Yacoby, J. J. Rehr, and E. A. Stern. Near-edge x-ray-absorption fine structure of pb: a comparison of theory and experiment. *Phys. Rev. B*, **47**:14126, 1993.

[49] J. J. Quinn. *Phys, Rev.*, **126**:1453, 1962.

[50] K. S. Singwi, M. P. Tosi, R. H. Land, and A. Sjölander. *Phys. Rev.*, **176**:589, 1968.

[51] J. Hubbard. *Proc. Roy. Soc.*, **A243**:336, 1957.

[52] D. M. Ceperley and B. J. Alder. *Phys. Rev. Lett.*, **45**:566, 1980.

[53] H. J. Flad and A. Savin. A new jastrow factor for atoms and molecules, using two- electron systems as a guiding principle. *J. Chem. Phys.*, **103**:691, 1995.

[54] J. P. Perdew. Generalized gradient approximations for exchange and correlation: a look backward and forward. *Physica B.*, **172**:1, 1991.

[55] O. Gunnarsson, O. K. Andersen, O. Jepsen, and J. Zaanen. Density-functional calculation of the parameters in the anderson model: application to mn in cdte. *Phys. Rev. B*, **39**:1708, 1989.

[56] P. M. Marcus and V. L. Moruzzi. Stoner model of ferromagnetism and total-energy band theory. *Phys. Rev. B*, **38**:6949, 1988.

[57] P. Horsch, W. von der Linden, and W.-D. Lukas. On the self-energy of electron gas in metals. *Sol. St. Comm.*, **62**:359, 1987.

[58] M. Alouani. Final-state rule and the absorption spectra for 3d ferromagnets. *Phys. Rev. B*, **49**:16 038, 1994.

[59] M. Ia. Amusia. *Atomic photoeffect*. Plenum Press, New York, 1990.

[60] L. Hedin. Extrinsic and intrinsic processes in exafs. *Physica B.*, **158**:344, 1989.

[61] J. J. Rehr, L. Hedin, and W. Bardyszewski, 1996. unpubsished.

[62] O. Gunnarsson and F. Aryasetiawan, 1996. report at the APS Meeting.

[63] G. N. George. ESAFSPAK code.

[64] P. J. Ellis and H. C. Freeman. Xfit - an interactive exafs analysis program. *J. Synch. Rad.*, **2**:190, 1995.

[65] A. L. Ankudinov, S. I. Zabinsky, and J. J. Rehr. Single configuration dirac-fock atom code. *Comp. Phys. Comm.*, 1996. in press.

[66] J. P. Desclaux. A multiconfiguration dirac-fock program. *Comp. Phys. Comm.*, **9**:31, 1975.

[67] A. V. Soldatov, T. S. Ivanchenko, A. P. Kovtun, S. D. Longa, and A. Bianconi. Spin-dependent mn k-edge xanes of mno and mnf2: full multiple scattering analysis. *Phys. Rev. B*, **52**:11757, 1995.

[68] M. Vaarkamp, I. Dring, R. J. Oldman, E. A. Stern, and D. C. Koningsberger. Comparison of theoretical methods for the calculation of extended x-ray-absorption fine structure. *Phys. Rev. B*, **50**:7872, 1994.

[69] M. Newville. *Local Thermodynamic Measurements of Dilute Binary Alloys Using XAFS*. PhD thesis, University of Washington, 1995.

[70] D. Arvanitis and K. Baberschke. Adsorbate-substrate bonding and dynamics as determined by sexafs. *J. Elec. Spect.*, **75**:149, 1995.

[71] P. Le Fevre, H. Magnan, and D. Chandesris. X-ray absorption at the $l_{2,3}$ edge of an anisotropic single crystal: cadmium (0001), 1996. to be published.

[72] R. C. Albers and A. Ormeci. private communication.

[73] J. Mustre de Leon, J. J. Rehr, S. I. Zabinsky, and R. C. Albers. *Phys. Rev. B*, **44**:4146, 1991.

[74] E. Dartyge. personal communication.

[75] C. Brouder, M. Alouani, and K. H. Bennemann. unpublished.

[76] K. Hamalainen. C. C. Kao, J. B. Hastings, D. P. Siddons, L. E. Berman, V. Stojanoff, and S. P. Cramer. Spin-dependent x-ray absorption of mno and mnf/sub 2/. *Phys. Rev. B*, **46**:14274, 1992.

[77] C. Brouder and M. Hikam. *Phys. Rev. B*, **43**:3809, 1991.

VITA

Alexei Ankoudinov graduated from St.Petersburg State University in 1987 with a B.A. in Physics, specializing in infrared absorption and Raman spectra. He then worked as a research assistant in the Gas-dynamics Laboratory of the Ioffe Physical-Technical Institute. Later, as a graduate student at the Radium Institute, St.Petersburg, Russia he developed a code to calculate crystal field parameters from experimental optical data.

Moving through the electro-magnetic spectrum from infra-red through optical wavelengths naturally lead him to the study of X-ray absorption spectra at the University of Washington in 1992. He received his Master of Science in Physics in 1993. This dissertation completes the requirements for his Ph.D. in Physics.